

**NASA  
Technical  
Paper  
2954**

January 1990

Surface Flow and Heating  
Distributions on a Cylinder  
in Near Wake of Aeroassist  
Flight Experiment (AFE)  
Configuration at Incidence  
in Mach 10 Air

William L. Wells

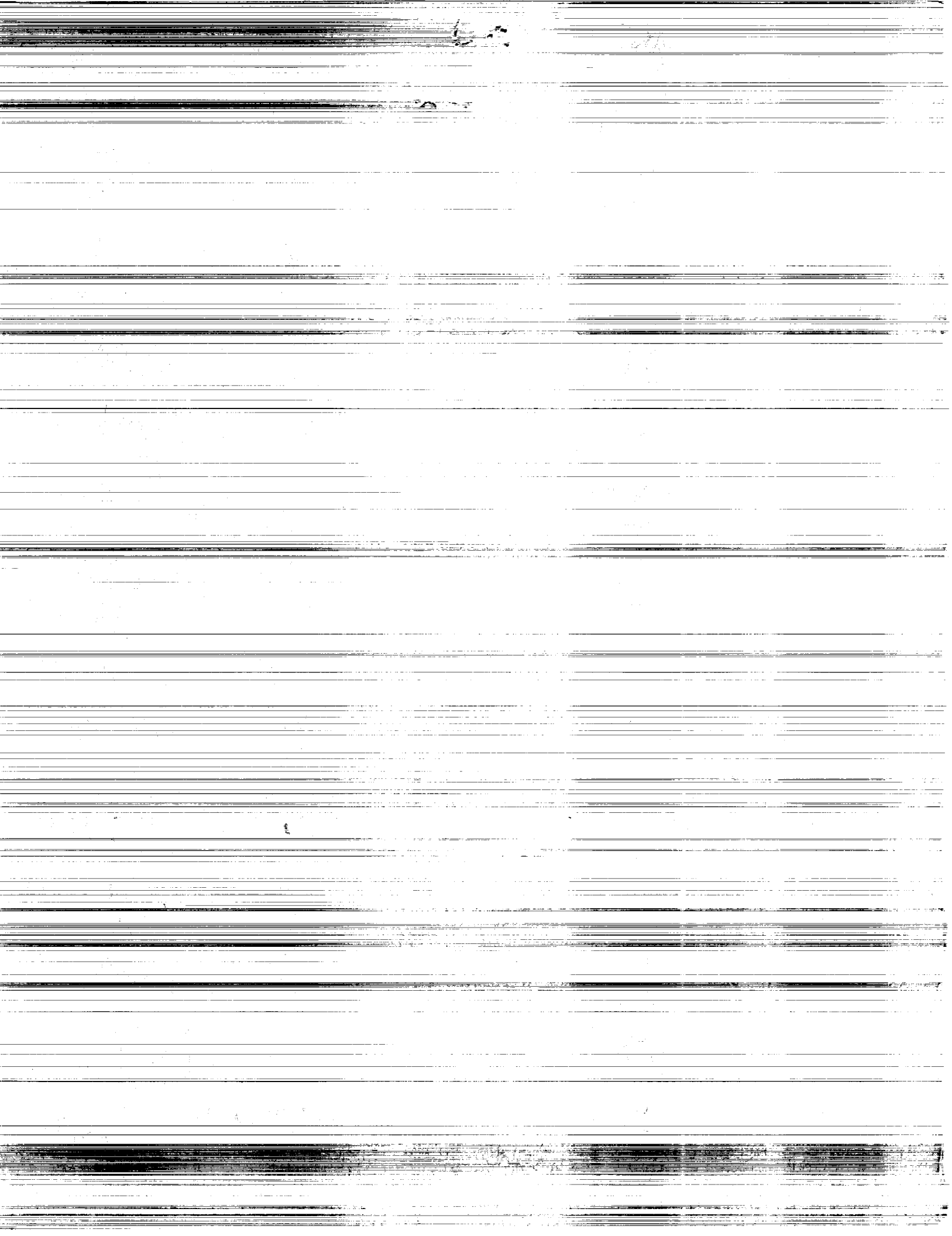
(NASA-TP-2954) SURFACE FLOW AND HEATING  
DISTRIBUTIONS ON A CYLINDER IN NEAR WAKE OF  
AEROASSIST FLIGHT EXPERIMENT (AFE)  
CONFIGURATION AT INCIDENCE IN MACH 10 AIR  
(NASA) 58 p

N90-14493

CSCL 200 H1/34

Unclass  
0232297

**NASA**



**NASA  
Technical  
Paper  
2954**

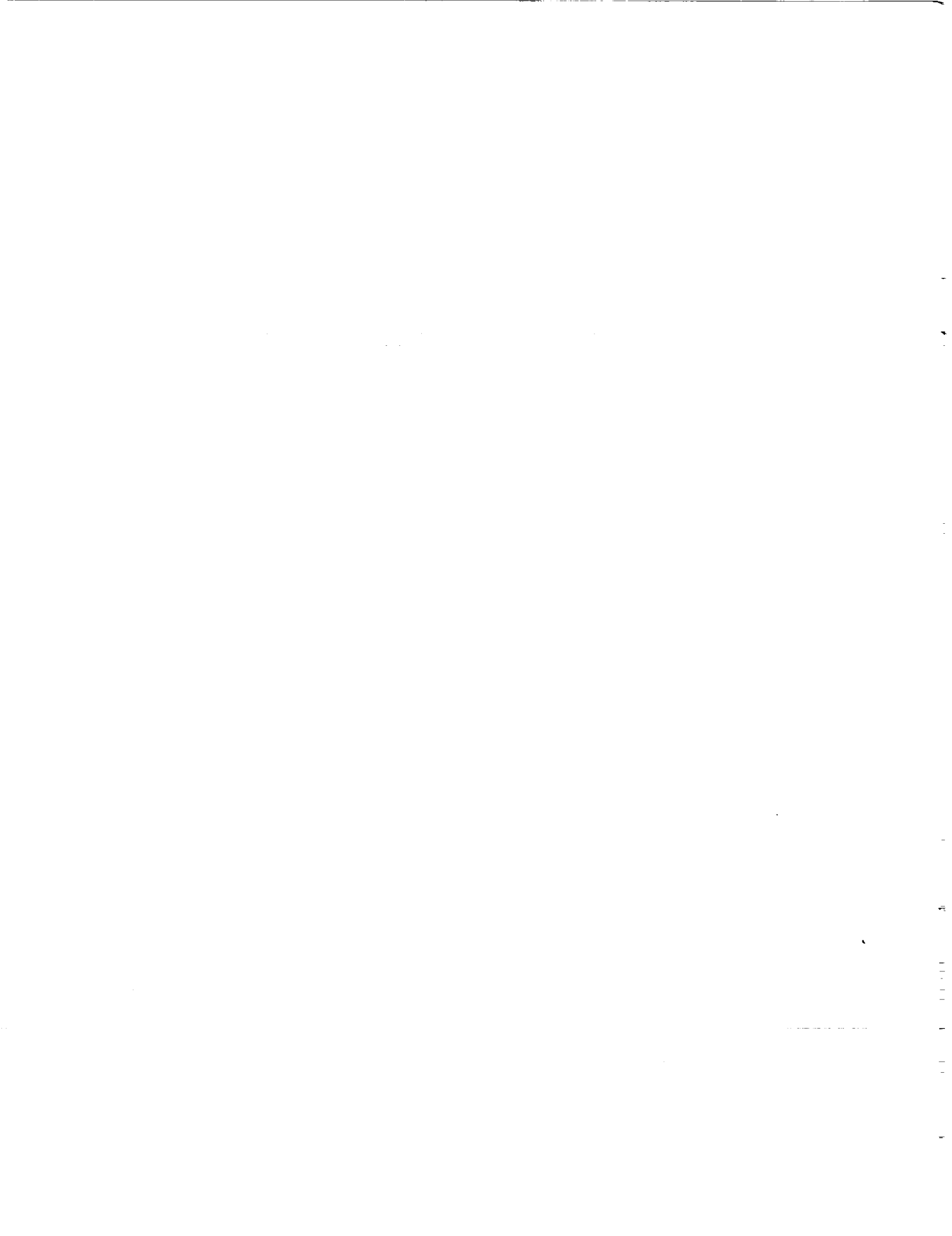
1990

Surface Flow and Heating  
Distributions on a Cylinder  
in Near Wake of Aeroassist  
Flight Experiment (AFE)  
Configuration at Incidence  
in Mach 10 Air

William L. Wells  
*Langley Research Center  
Hampton, Virginia*



National Aeronautics and  
Space Administration  
Office of Management  
Scientific and Technical  
Information Division



## Summary

Measurements of heating rate and surface streamline directions were made along a cylinder in the near wake of the Aeroassist Flight Experiment (AFE) configuration. The AFE aerobrake is a raked  $60^\circ$  half-angle elliptic cone with an ellipsoid-blunted nose and a rounded shoulder at the base plane. Heating rates were measured with thin-film resistance gages and surface streamlines determined by the oil-flow technique in the Langley 31-Inch Mach 10 Tunnel. The tests were conducted for a range of angle of attack from  $-10^\circ$  to  $5^\circ$ , a sideslip angle of  $0^\circ$ , and a range of postshock Reynolds number based on model diameter from 6300 to 50000 in air. Heating rates predicted with a Navier-Stokes computer code were compared with measurements.

Flow over the cylinder is dominated by impingement of that portion of the free shear layer that originates from the corner of the forebody upper surface (ellipsoid section). The location of impingement was deduced from surface streamline directions as indicated by oil flow and from heating-rate distributions. Downstream of the impingement region, the oil flow appears similar to that of a swept cylinder in a supersonic stream, with cross-flow separation resulting in the formation of twin longitudinal counter-rotating vortices with reattachment along the "lee-side" centerline. The rear stagnation point (point of upstream- and downstream-directed oil flow) moves upstream with decreasing angle of attack but is not a significant function of Reynolds number. Maximum heating occurs near, but downstream of, the rear stagnation point inferred from oil-flow patterns. The distance between the rear stagnation point and the maximum heating region decreases with decreasing angle of attack and/or increasing Reynolds number. The heating magnitude is greatest along the upper surface, where direct impingement occurs, decreases along the sides, and is least along the lower surface. The magnitude of heating on the cylinder, particularly in the maximum heating region, is significant relative to the computed forebody stagnation point heating. For example, for angles of attack from  $-5^\circ$  to  $5^\circ$ , the corresponding range of maximum heating is from 45 percent to 28 percent of the computed forebody stagnation point value. Heating-rate distributions predicted with the Navier-Stokes computer code are generally in good agreement with the measurements.

## Introduction

Future space transportation systems include space transfer vehicles (STV's, formerly referred to as orbital transfer vehicles, or OTV's) that will be

used to ferry cargo to and from a high-Earth orbit (for example, geosynchronous orbit) to low-Earth orbit where the Space Shuttle and a space station will operate. Studies have shown that upon return to low-Earth orbit the STV can carry a significantly greater payload when decelerated by drag during a pass through the outer portion of the Earth's atmosphere than when decelerated by retro-rockets (ref. 1). Space transfer vehicles designed to use the Earth's atmosphere for deceleration are generally referred to as aeroassisted space transfer vehicles, or ASTV's. The aerobrake version of an ASTV is envisioned to be an umbrella-shaped forebody of perhaps 60-ft diameter with a payload mounted in the immediate near wake. Much more information about very high-altitude, high-velocity flight is needed, however, before an actual ASTV can be optimally designed. Preparations are underway to conduct a flight experiment in which a 14-ft-diameter, instrument-laden simulated ASTV configuration (fig. 1) will be launched from the Space Shuttle, make a sweep through the upper atmosphere to gain aerodynamic and aerothermal information, and then return to low-Earth orbit where it will be retrieved by the Space Shuttle. The rationale for this experiment, called the Aeroassist Flight Experiment (AFE), is outlined in reference 2, and the set of experiments to be performed is described in reference 3.

The flight experiment has been proposed because of the scarcity of flight data in a high-velocity, low-density environment. Furthermore, this environment cannot be fully duplicated or simulated in present test facilities nor adequately modeled by existing computational techniques. The AFE will provide an experimental data base for validation and refinement of current computational fluid dynamics (CFD) codes to be used in future ASTV designs. However, the AFE itself requires a data base for prediction of its flight characteristics; and present test facilities, in conjunction with the best available CFD codes, must provide this information. A preflight test program in ground-based hypersonic facilities (ref. 4) was initiated to develop an aerodynamic and aerothermodynamic data base to aid in project planning and to provide calibration data for the most recent CFD computer codes. This test program has already provided a comprehensive data base of aerodynamic characteristics, distributions of pressure and aerodynamic heating on the forebody, surface streamlines, and shock shapes. Some of these data have been reported in references 5, 6, and 7. Attention is now being focused on heating in the near-wake region. Aerodynamic heating in the near wake of the AFE is of interest because the instrumentation

carrier for the experiments is located in the base region, and it is here that cargo will be carried by ASTV's.

The wake of blunt bodies in hypersonic flow is quite complicated, and although the literature (for example, ref. 8) reveals some controversy as to the exact nature of the flow under various conditions, a generally accepted concept of the flow is shown by the sketch in figure 2. The salient features are an inner flow that recirculates in the base region and an outer flow that continues downstream. The dividing streamline, a concept first introduced by Chapman (ref. 9), separates the inner and outer flow and ends at a rear stagnation point. The dividing streamline is embedded in a viscous shear layer which originates with the boundary layer that separates off the aft edge of the forebody surface. Near the rear stagnation point (in the absence of a solid surface), the flow from one side of the body meets the flow from the opposite side. Recompression waves coalesce into a recompression shock, and shear-layer flow outside the dividing streamline continues downstream through a "neck" while flow inside the dividing streamline turns upstream into the base region. The addition of a solid surface (for example, a sting) must obviously alter the flow, but studies with backward-facing steps (ref. 10) reveal the same primary features of an inner recirculating flow, free shear layer, outer flow, and a recompression/reattachment shock.

During the 1960's, investigations of wake flow characteristics at supersonic and hypersonic speeds flourished both analytically and experimentally. Experimental efforts for the most part focused on pressure measurements, but the literature for that era reflects particularly diverse analytical activities, most of which are summarized in a book by Berger (ref. 8). A 1969 survey of hypersonic near-wake studies is presented in reference 11. A recent survey of the literature reveals less activity in the intervening years. The forecast for use of ASTV's has renewed an interest in the near wake of blunt bodies in hypersonic flow because payloads are expected to be carried in the base region of those vehicles. Measurements of heat transfer on a cylinder in the wake of generic ASTV's (AFE not included) by the phase-change paint technique are reported in reference 12. Afterbody heat-transfer measurements with thermocouples are reported for a two-dimensional blunt body in reference 13. The advent of high-speed super computers has made it feasible to address the problem in more detail by using advanced numerical techniques as reported in references 14 through 18.

The primary purpose of the present study was to illustrate the effects of angle of attack and Reynolds number on aerodynamic heating and surface stream-

line directions on a generic afterbody shape in the near wake of the AFE forebody configuration. Although the aft portion of the experimental test model is different from the actual flight vehicle, it provides a way to include the model support sting in the numerical computer code models and allows measurements at a sufficient distance to allow measurement of base flow closure effects. The experimental results provide calibration data for Navier-Stokes codes in the AFE near-wake region. The tests were conducted in air through a range of angle of attack in the Langley 31-Inch Mach 10 Tunnel. Reynolds number immediately behind the normal shock, based on forebody diameter, ranged from approximately 6300 to 50 000.

## Symbols

$c$	model material heat capacity, Btu/lb·°R
$D$	diameter of model forebody, 3.67 in.
$d$	shear-layer thickness (fig. 2), in.
$h$	test gas enthalpy, Btu/lb
$k$	model material thermal conductivity, Btu/ft·sec·°R
$\ell$	distance from forebody base to measurement location, in.
$M$	Mach number
$Pr$	test gas Prandtl number
$Re$	unit Reynolds number, ft <sup>-1</sup>
$p$	pressure, psia
$\dot{q}$	heating rate, Btu/ft <sup>2</sup> ·sec
$r_{ref}$	nose radius of reference sphere, in.
$s$	distance between shear-layer impingement locations as indicated by oil flow and peak heating, in.
$T$	temperature, °R
$t$	time, sec
$U$	velocity, ft/sec
$\alpha$	angle of attack, deg
$\beta$	thermal product, $\sqrt{\rho ck}$ , Btu/ft <sup>2</sup> ·°R·sec <sup>1/2</sup>
$\Gamma$	velocity gradient (eq. (3))

$\theta$	gage-array location angle (fig. 5), deg
$\mu$	test gas viscosity, slug/ft-sec
$\rho$	density, slug/ft <sup>3</sup>
$\psi$	angle between free shear layer and cylinder surface (fig. 2), deg

Subscripts:

$D$	diameter
$o$	initial time
ref	reference
surf	surface of cylinder
$t$	stagnation conditions
$w$	wall conditions
$\infty$	free-stream conditions
2	flow conditions immediately behind normal shock

### AFE Configuration

The basic AFE flight vehicle will be composed of a 14-ft-diameter drag brake, an instrument carrier at the base, a solid rocket propulsion motor, and small control motors. A sketch of the vehicle is shown in figure 1. The drag brake (fig. 3), or forebody configuration, is derived from a blunted elliptic cone that is raked off at 73° to the centerline to produce a circular raked plane. A skirt having an arc radius equal to one-tenth of the rake-plane diameter and an arc length corresponding to 60° has been attached to the rake plane to reduce aerodynamic heating around the base periphery. The blunt nose is an ellipsoid with an ellipticity of 2.0 in the symmetry plane. The ellipsoid nose and the skirt are tangent to the elliptic cone surface at their respective intersections. The half angle of the original elliptic cone is 60° in the vehicle symmetry plane. A detailed description of the analytical shape is presented in reference 19.

### Apparatus and Tests

#### Facility

The Langley 31-Inch Mach 10 Tunnel expands dry air through a three-dimensional contoured nozzle to a 31- by 31-in. square test section to achieve a nominal Mach number of 10. The air is heated to approximately 1850°R by an electrical resistance heater, and the maximum reservoir pressure is approximately 1500 psia. The tunnel, formerly referred

to as the Langley Continuous-Flow Hypersonic Tunnel, is presently operated in the blowdown mode with nominal run times of up to 60 sec. Prior to injection into the test stream, the model is stored in an enclosure that is isolated from the test stream by a sliding door. Injection time is approximately 0.5 sec. This tunnel is described in reference 20.

#### Test Conditions and Test Matrix

The present tests were conducted in a wind tunnel with a nominal free-stream Mach number of 10 in air. Nominal free-stream unit Reynolds numbers were 0.25, 0.54, 1.09, and 2.17 million per foot. Angle of attack was varied from 5° to -10° in 5° increments with a sideslip angle of 0°. Nominal flow conditions for the tunnel are presented in table I.

### Models and Instrumentation

#### Models

Two models were used in the present study, one for convective heat-transfer measurements and another for oil-flow tests. Both models are the same size and shape. The forebody shape is described in the "AFE Configuration" section and illustrated in figure 3. For each model, the forebody symmetry-plane base height ("D" in fig. 4) is 3.67 in. (0.022 scale), and the material is Stycast.<sup>1</sup> Although the model cross section in the rake plane is circular, the addition of the torus-section skirt results in a base that is slightly elliptical.

**Heat-transfer model.** Photographs of the heat-transfer model are shown in figures 5(a) and (b). An aluminum cylinder/cone-frustum section extends from the forebody base to slightly overlap the forward end of the instrumented cylinder. A rubber seal is provided at the forebody base to prevent flow circulation underneath the aluminum section.

The forebody has a threaded hole at the base center to accept the threaded end of the sting so that the sting and instrumented cylinder are perpendicular to the forebody base plane. The sting and cylinder can be rotated relative to the forebody. Consequently, the cylinder may be positioned and pinned in place with the gage array facing upward or downward in the forebody symmetry plane or at 45° increments between these two locations. (The lead of the screw thread causes a slight displacement of the gage locations relative to the forebody base when the cylinder is rotated, but this is accounted for when the data are tabulated or plotted.) In figure 5(a), the angle  $\theta$  is defined to locate the gage

<sup>1</sup> Stycast, a highly filled epoxy compound, is a registered trademark of Emerson and Cuming Co., Inc.

array, where  $\theta = 0^\circ$  and  $\theta = 180^\circ$  represent upward- and downward-facing gages, respectively. The 1.01-in.-diameter instrumented Macor<sup>2</sup> cylinder is hollow with a 0.25-in. wall thickness and is coaxial with the sting. A linear array of 21 thin-film heat-transfer gages is mounted on three highly polished Macor inserts that are fitted and contoured to the cylinder (fig. 4). A slot in the hollow sting allows passage of a lead-wire pair from each gage to the data acquisition system. The nominal axial distance between gages is 0.15 in. except for two at adjoining inserts where the nominal distance is 0.25 in. (fig. 6). The gages were applied by a sputtering process that is described in reference 21.

**Surface streamline (oil-flow) model.** As mentioned previously, the shape and size of the model used to record surface streamlines are the same as for the heat-transfer model. The forebody for this model and the forebody for heat-transfer model were cast in the same mold, and an accurately machined force model was used as a pattern for the mold. However, the oil-flow-model cylinder material is Stycast instead of Macor and is not instrumented with thin-film gages.

## Instrumentation

**Heat transfer.** Thin-film resistance gages were used to measure heat transfer. The palladium sensing element of each gage is in a serpentine pattern and is approximately 0.040 in. by 0.050 in. by approximately 1000 Å thick. To provide some protection for the delicate gages, they were covered with Al<sub>2</sub>O<sub>3</sub> approximately 5000 Å thick. The Macor inserts on which the gages are deposited are 0.20-in. thick and 0.25-in. wide. For continuity in thermal properties, the cylinder in which the inserts are placed is also made of Macor. Each gage resistance is nominally 100 ohms at room temperature, but varies with temperature in a known way from a calibration in a well-stirred oil bath for temperatures from 535°R to 685°R.

During a test, provision is made to monitor and record the voltage change across each gage while supplying a constant current through it. Hence, each gage resistance can be determined at any time. Two constant-current diodes are available for each gage to provide a selection of either 1 mA or 4 mA. The higher current results in larger signals and is used for gages in lower heating areas. (Current values higher than these are not used because of possible ohmic

heating of a gage.) Gage signals can be increased by use of built-in amplifiers with amplification factors of 2, 5, 10, 20, 50, and 100. The data system can accept signals up to 1000 mV; hence in the present study, constant-current/amplifier combinations were selected in an attempt to provide signals nominally mid-range. A 38-Hz filter is included in the circuit to avoid higher frequency-induced oscillations. The heating rate is computed from the surface temperature change with time (as determined by the change in gage resistance) and the Macor thermal properties.

**Surface streamlines.** Streamlines on surfaces in the wake region were detected by movement of oil drops that were deposited on the surfaces prior to a test. Surface flow directions were obtained from post-run photographs of the oil streaks. A video camera was used to record oil movement during a test. Good contrast was provided between the oil and the model surfaces by mixing artist's white oil paint with a clear silicone fluid to serve as the carrier and painting the surfaces black. The silicone fluid was available for a range of viscosity values.

## Data Reduction and Uncertainty

### Heat Transfer

The numerical method used to compute heat-transfer rates from the output of the thin-film resistance gages assumes a thick wall with one-dimensional heat transfer and is discussed in detail in reference 21. The equations used are

$$\dot{q}(t) = \frac{\sqrt{\pi\beta}}{2} \left( \frac{\Delta T(t)}{\sqrt{t}} + \frac{1}{\pi\sqrt{t}} \int_0^t \frac{\sqrt{\lambda}\Delta T(t) - \sqrt{t}\Delta T(\lambda)}{(t-\lambda)^{3/2}} d\lambda \right) \quad (1)$$

where the substrate thermal properties ( $\beta = \sqrt{\rho ck}$ ) are assumed to be constant during the run,  $\Delta T(t)$  is an arbitrary surface-temperature time history ( $\Delta T(0) = 0$ ),  $\lambda$  is a dummy variable, and the presence of the thin-film sensor is neglected. Equation (1) is integrated numerically to obtain the heating rate. A difficulty arises in the numerical integration because of the singularity in the integrand evaluated at the upper limit  $t = \lambda$ . To avoid this singularity, which will give rise to errors in the deduced value of heating rate, the following equation is used:

$$\dot{q}(t) = \frac{2\beta}{\sqrt{\pi}} \sum_{i=1}^n \frac{\phi(t_i) - \phi(t_{i-1})}{\sqrt{t_n - t_i} + \sqrt{t_n - t_{i-1}}} \quad (2)$$

where  $\phi = \int_0^T (k/k_o) dt$  and  $n$  is the number of steps (time intervals).

<sup>2</sup> Macor, a glass-ceramic, is a registered trademark of Corning Glass Works.

Also in reference 21 is a discussion of the calibration procedure used to determine the temperature coefficient of resistance of each gage and the contributors to the uncertainty in the heat-transfer rate inferred from the gages. The effect on inferred heating rate resulting from temperature-induced variations in Macor thermal properties is discussed in reference 22.

In the present tests, a number of precautions were taken to reduce uncertainties in the measurements. Corrections of less than 2 percent were made to account for variations with temperature of the Macor thermal product  $\beta = \sqrt{\rho ck}$  as suggested in appendix B of reference 22. (The value of  $\beta$  used was  $0.097 \text{ Btu/ft}^2 \cdot \text{sec}^{1/2} \cdot \text{R}$  at  $536^\circ \text{R}$ .) As further precautions, the analog-to-digital converter was calibrated daily, the circuit current was verified by measuring the voltage across a precision resistor temporarily substituted for each gage, and each gage resistance was measured and compared with the calibration resistance at ambient conditions just prior to each run. The signal-to-noise ratio during a run depended on the signal strength, which varied with the gage-array location and the particular gage location within the array. In general, the signal strength decreased as the gage locator angle  $\theta$  increased from  $0^\circ$  to  $180^\circ$ . For each run, "time zero" was selected to be 0.06 sec prior to a detectable signal increase resulting from model injection into the test stream. The baseline signal was taken to be the average signal over a 0.5-sec period preceding time zero. (Data were taken at a rate of 50 samples/sec per gage.) Heating rate was determined over the 3-sec run duration beginning at time zero, and a least-squares curve was fit to the heating-rate time history for 1.3 sec beginning at 0.5 sec after time zero, that is, immediately after the model became stationary at the test stream centerline. The data presented herein were taken at approximately the midpoint of this curve. Examples of heating-rate time histories with curve fits are presented in figure 7, where 7(a) shows a result of one of the high-heating signals and 7(b) a result of one of the very low-heating signals. In figure 7(a), notice that the rise in surface temperature ( $\Delta T_{\text{surf}}$ ) at the beginning and end of the curve fit is  $17.3^\circ \text{R}$  and  $43.8^\circ \text{R}$ , respectively, whereas the corresponding values in 7(b) are only  $0.83^\circ \text{R}$  and  $1.91^\circ \text{R}$ . The fast response, surface-mounted thin-film gages make it possible to deduce heat-transfer rates even with  $\Delta T_{\text{surf}}$  as small as that indicated in figure 7(b). Run-to-run repeatability of measured heat-transfer rates is illustrated in figure 8. For  $\theta = 0^\circ$ , repeatability is within  $\pm 1.4$  percent of the average value for each gage. In figure 8(b), where the values of heating correspond to  $\theta = 180^\circ$  and are quite small, the deviation from the average can be as much as  $\pm 9$  percent, but is within

about 3 percent for most gages. Deviation for each gage location is tabulated in figure 8. (Heating distribution profiles are discussed in the "Results and Discussion" section.)

From the discussions of probable error sources in reference 22 and consideration of precautions taken during the present test program, the uncertainty in measured heat-transfer rate is estimated to be within 8 percent for all gage locations except for  $\theta = 180^\circ$ . Based only on data reduction procedures and repeatability, the uncertainty in measured heat-transfer rate along most of the  $\theta = 180^\circ$  line (where low heating occurs) is estimated to be about 12 percent.

### Surface Streamlines

The oil-flow technique provided a visual record of surface flow directions but not quantitative data. The flow directions were not obtained on some areas, however, because the shear at the surface was too low to move the oil droplets. The oil viscosity required to allow movement on particular surface areas was determined primarily by experience.

### Flow Conditions

Free-stream and post-normal-shock flow conditions were determined by using the measured reservoir pressure, reservoir temperature, and pitot pressure ( $p_{t,2}$ ) and assumption of an isentropic expansion in the nozzle. The pitot pressure was obtained from unpublished pressure-calibration tests conducted just prior to the present test series. The tunnel provides excellent flow uniformity, as illustrated in reference 23. Calorically imperfect air effects (ref. 24) were accounted for in the flow quantities calculations.

### Reference Heating Rate

The plotted heat-transfer data herein are non-dimensionalized by reference heating rates. These reference values are computed heating rates to the stagnation point of a sphere using the method of Fay and Riddell (ref. 25). The reference sphere radius is 2.25 in., which approximates the AFE model forebody ellipsoidal nose radius in the symmetry plane. The equation is

$$\dot{q}_{\text{ref}} = \frac{0.76}{\text{Pr}_w^{0.6}} (\rho_{t,2} \mu_{t,2})^{0.4} (\rho_w \mu_w)^{0.1} (h_{t,2} - h_w) \Gamma^{0.5} \quad (3)$$

where for air  $\text{Pr}_w = 0.71$ , and  $\Gamma$  is the velocity gradient approximated by the Newtonian expression

$$\Gamma = \frac{1}{r_{\text{ref}}} \sqrt{\frac{2(p_{t,2} - p_\infty)}{\rho_{t,2}}}$$

and the subscript  $w$  denotes quantities at the wall where the temperature was always set equal to  $540^\circ\text{R}$ . Reference 21 further outlines the derivation of individual quantities within equation (3) including corrections for imperfect gas effects in the flow.

In heat-transfer tests on the forebody at  $\alpha = 0^\circ$ , measured heat-transfer rates (ref. 6) in the nose region were about 20 percent greater than values obtained by equation (3) for the same nose radius as assumed in the tests reported herein. The ellipsoidal nose is three-dimensional (as opposed to axisymmetric) and possibly could be better represented by a radius other than the symmetry plane value. Such an "effective" nose radius may in fact vary with angle of attack. However, the  $\dot{q}_{\text{ref}}$  computed by equation (3) allows data obtained from different test conditions to be compared on plots with a common scale, and the ratio  $\dot{q}/\dot{q}_{\text{ref}}$  provides some indication of the severity of the local heating compared with the forebody stagnation region heating at the same test conditions.

## Prediction

The predictions presented in this paper were obtained by use of the LAURA (Langley Aerothermodynamic Upwind Relaxation Algorithm) code. This code has been continually improved over the past few years, and the latest version is described in reference 14. The code uses an upwind-biased, point-implicit relaxation algorithm for obtaining the numerical solution to the governing equations (Navier-Stokes) for three-dimensional, viscous hypersonic flows, including chemical and thermal nonequilibrium when appropriate. A multidomain grid (fig. 9) allows for better resolution of the free shear layer coming off the forebody shoulder as compared with the resolution achievable using a single domain, structured grid. The flow is assumed to be steady and laminar.

## Results and Discussion

The test results are presented in three groups: oil-flow photographs, tabulated heat-transfer data, and graphical comparisons. The oil-flow photographs present views of the model top, side, and bottom and provide surface streamline directions in all the areas where heat-transfer measurements were made. The oil-flow and heat-transfer tests were conducted at the same test conditions. Run schedules for these heat-transfer and oil-flow tests are presented in tables II(a) and II(b). No schlieren equipment was available to visualize the flow away from the surface in the present study, but standard schlieren photography for some additional tests (unreported) at a higher Reynolds number in a Mach 6 tunnel faintly revealed

the free shear layer in the upper symmetry plane (as discussed in the Introduction) and clearly revealed the bow shock and reattachment shock as shown in figure 10. (Computer image enhancement was selectively used to strengthen the image of the shear layer in this figure.)

### Surface Streamlines (Oil Flow)

The oil-flow results are shown for the cylinder top in figures 11, 12, and 13 for postshock Reynolds numbers of approximately 6000, 14 000, and 50 000, respectively. The effect of  $\alpha$  at a given Reynolds number is illustrated in each of these figures. The effect of Reynolds number at a given  $\alpha$  can be seen by comparing corresponding parts of the three figures. For example, compare figures 11(a), 12(a), and 13(a) to see the effect of Reynolds number for  $\alpha = 5^\circ$ .

The most prominent feature in the streamline patterns of the top views is the apparent origin of streamlines where flow has been directed radially outward from the apparent "source." This "source" location, on top of and within approximately the upstream third of the cylinder, is assumed to be the impingement point of the dividing streamline (fig. 2), since flow has been directed upstream forward of this point and downstream behind this point. In the literature, this point is often referred to as the "rear stagnation point." It is apparent that this rear stagnation point moves upstream as the model is pitched down. Notice, however, that for a particular angle of attack there is little variation in impingement location with Reynolds number. A "v" symbol has been attached to each of the photographs in figures 11, 12, and 13 to indicate the location of the maximum measured heating rate along the top of the cylinder that is evident in figure 8(a). This location relative to the rear stagnation point will be discussed after discussion of the heat-transfer data.

Oil-flow patterns from the side view and bottom view are shown in figures 14 through 16 and 17 through 19, respectively. These views can be matched with the top views and tabulated heat-transfer data by facility run numbers. Downstream of the impingement point, the surface streamline directions resemble those on a cylinder at incidence in a supersonic free stream where the top ( $\theta = 0^\circ$ ) appears as the windward side and the bottom ( $\theta = 180^\circ$ ) the leeward side. In general, the photographs show cross flow with separation lines along the sides near the "leeward" side of the cylinder, a "feather" pattern that indicates the development of twin counterrotating vortices (ref. 26), and reattachment along the  $\theta = 180^\circ$  line. Patterns along the bottom side of the cylinder were often obscured because of oil accumulation along the flow separation line that was

swept across the bottom as the model was retracted from the test stream, and this accumulated oil tended to further run because of gravity. At a given angle of attack, Reynolds number did not strongly affect the overall flow patterns. Forward of the impingement location, the flow was directed forward and around the cylinder. Near the bottom, the flow separation line extended from the aft end nearly to the upstream end of the cylinder at  $\alpha = -5^\circ$  and  $-10^\circ$ , but not at  $\alpha = 0^\circ$  and  $5^\circ$ .

### Heat Transfer

Heating of the cylinder in the wake of the forebody is primarily due to impingement of the free shear layer, which originates around the entire periphery of the forebody base. Because of the forebody shape and relative orientation of the cylinder, however, the cylinder top ( $\theta = 0^\circ$ ) is more vulnerable to impingement, as previously illustrated in the schlieren photograph of figure 10. Because of the forebody rake angle (fig. 3), the cylinder, which is mounted perpendicular to the forebody base, is pivoted upward  $17^\circ$  to the free stream even when  $\alpha = 0^\circ$ . Decreasing the angle of attack further pivots the cylinder upward and orients it more nearly perpendicular to the upper shear-layer flow in the forebody symmetry plane.

The measured heat-transfer rate at each gage location for each of the four angles of attack is given in table III for nominal  $Re_{2,D} = 6500$ . Parts (a), (b), and (c) of table III correspond to locations of the gage array:  $\theta = 0^\circ$ ,  $45^\circ$ , and  $90^\circ$ , respectively. (See fig. 5(a).) Tables IV, V, and VI present the remainder of the data at other Reynolds numbers. Only one run was made at  $Re_{2,D} = 26\,500$ . Data for  $\theta = 180^\circ$  are limited to  $\alpha = 0^\circ$  and  $5^\circ$  at  $Re_{2,D} = 13\,700$  and  $50\,800$ . In each table, the measured wall temperature is also given for the time at which the heat-transfer measurement was made with each gage.

Heating-rate distributions on the cylinder are presented in figure 20 at four angles of attack at nominal  $Re_{2,D} = 13\,700$ . Parts (a), (b), (c), and (d) of the figure are for  $\theta = 0^\circ$ ,  $45^\circ$ ,  $90^\circ$ , and  $180^\circ$ , respectively. The maximum values of heating occur on top of the cylinder ( $\theta = 0^\circ$ ). In figure 20(a), a heating peak associated with the free-shear-layer impingement is evident. The axial location of the rear stagnation point as indicated by oil flow is also shown. Relative to the computed forebody nose heating, the value of heating on top of the cylinder is significant and increases with decreasing angle of attack. For example, peak heating is about 28 percent of forebody stagnation point heating at  $\alpha = 5^\circ$ , about 33 percent at  $\alpha = 0^\circ$ , and about 45 percent at  $\alpha = -5^\circ$ . At  $\alpha = -10^\circ$ , maximum heating is nearly 58 percent of the com-

puted forebody stagnation point value. Upstream of the impingement location, in the recirculation region, heating decreases rapidly toward the base to only a small fraction of the peak value. Downstream of impingement, the heating decreases somewhat but still remains at a relatively high value along the remainder of the cylinder. For example, at  $\alpha = 0^\circ$ , the peak heating ratio is approximately 0.33, the value at the upstream end is smaller by nearly a factor of 10, and the value near the downstream end is about 0.24. It is also evident from figure 20(a) that as the angle of attack is increased, the peak heating becomes less localized. The peak heating profile is expected to broaden with increasing angle of attack, since the angle between the shear layer and the cylinder surface becomes smaller. That is, if the shear layer is visualized as a slab of thickness  $d$  inclined at an angle  $\psi$  to the cylinder surface (in a plane, fig. 2), then the shear layer "foot print," or length in contact with the surface, is  $d/\sin\psi$  where  $\sin\psi$  decreases with increasing  $\alpha$ .

As the gage location angle increases from  $\theta = 0^\circ$ , the heating distributions undergo a change. At  $\theta = 45^\circ$  (fig. 20(b)), the distributions are very similar to those at  $\theta = 0^\circ$ , although the peak heating values are lower. At  $\theta = 90^\circ$ , heating peaks occur farther downstream, are less localized, and values are smaller than at  $\theta = 0^\circ$  or  $45^\circ$ . The peaks are approximately equal in magnitude for each angle of attack, but are separated longitudinally as a function of  $\alpha$ .

The peaks in heating distributions at  $\theta = 0^\circ$ ,  $45^\circ$ , and  $90^\circ$  indicate an effect of direct impingement of the free shear layer. At  $\theta = 180^\circ$  (fig. 20(d)), there is no evidence of direct impingement, and the heating rate monotonically increases with distance downstream. At the most downstream measurement, the heating is nearly as high as that at  $\theta = 90^\circ$ . (Tests were run with only two values of  $\alpha$  at  $\theta = 180^\circ$ .) The data suggest that the heating is a result of flow impingement on the cylinder upper surface ( $\theta = 0^\circ$ ), since heating rates increase with decreasing  $\alpha$  instead of the reverse order, which would occur if flow impingement from the lower forebody shear layer was the source. Recall that oil-flow results revealed cross flow from the upper surface with separation along the sides and reattachment along the bottom centerline.

The previously discussed data were from tests at a fixed postshock Reynolds number and variable  $\alpha$ . The effect of Reynolds number variation at  $\alpha = 0^\circ$  is illustrated in figure 21 by data obtained with  $\theta = 0^\circ$ . For approximately a factor-of-eight variation in Reynolds number, the distributions and relative levels of heating are not significantly different except near the location of direct shear-layer impingement

where peak heating occurs. The peak heating ratio for  $Re_{2,D} = 50770$  is about 25 percent higher than for  $Re_{2,D} = 6450$ , and the peak heating location moves upstream with increasing Reynolds number. It is obvious from the photographs in figures 11, 12, and 13 and the heating distributions in figures 20 and 21 that peak heating and the rear stagnation region as indicated by oil flow do not occur at the same location. They are closer as  $\alpha$  decreases, however (fig. 20(a)). The effect of Reynolds number on the relative locations at a given angle of attack (for example,  $-5^\circ$ ) can be seen by comparing figures 11(c), 12(c), and 13(c), or for  $\alpha = 0^\circ$  in figure 21. As the postshock Reynolds number varies from approximately 6000 to 50 000, the peak heating point and the rear stagnation point become increasingly closer until they are nearly coincident. The peak heating location is noted to shift whereas the rear stagnation point remains essentially fixed. It is recognized that the oil-flow tests were conducted for a longer run time (8-10 sec) than the heat-transfer tests (3 sec), and consequently, the increase in forebody wall temperature associated with longer test time could influence the forebody boundary-layer characteristics. A review of videotapes of oil-flow tests reveals no change in the rear stagnation point location during a test, however.

The relationship between locations of peak heating and rear stagnation point is summarized in figure 22. The solid symbols indicate peak heating location, whereas the open symbols indicate location of the rear stagnation point (from oil flow) for the same angle of attack. As  $\alpha$  is decreased, the peak heating and rear stagnation point locations become closer for all  $Re_{2,D}$ , and as  $Re_{2,D}$  is decreased, the distance is increased at any value of  $\alpha$ . This scenario is consistent with a fluid layer of thickness  $d$  having a low-energy inner region and a high-energy outer region intersecting a solid surface at an angle  $\psi$  as depicted in the highly simplified sketch of base region flow in figure 2. At the cylinder surface, the distance  $s$  between the rear stagnation point and outer edge of the shear layer would be proportional to  $d/\sin\psi$  where  $d$  increases with decreasing  $Re_{2,D}$  (thicker forebody boundary layer) and  $\psi$  decreases with increasing angle of attack for the model configuration used in the current tests. For example,  $d$  would be expected to be largest and  $\psi$  smallest in the lower right-hand corner of figure 22 so that  $s$  would be greatest as illustrated. The opposite effect would be expected in the upper left-hand corner of the figure which is also indicated by the results. Undoubtedly the interaction of the flow and the surface departs from the simple interaction depicted in figure 2 because the values of  $s$  seem quite large

when the shear-layer thickness shown in the schlieren photograph of figure 10 is considered. (For example, for  $\alpha = 5^\circ$ , the distance between peak heating and rear stagnation point locations is  $\approx 0.23\ell/D$  (0.8 in.) at the lowest  $Re_{2,D}$  and  $0.14\ell/D$  (0.5 in.) at the highest  $Re_{2,D}$ .) The outer edge of the shear-layer flow apparently tends to turn in a direction more nearly parallel to the surface thereby increasing the value of  $s$ . The flow would be expected to turn more parallel to the surface when  $\psi$  is small, that is, when the angle of attack is largest and  $s$  would be greater, as indicated by the data in figure 22.

As previously mentioned, a number of investigators have developed numerical algorithms to compute the flow field about three-dimensional bodies in a hypersonic environment. Peter A. Gnoffo at the Langley Research Center incorporated the configuration (forebody and cylinder) used in the present experimental study in his code LAURA. This computer code is discussed in detail in reference 14 and briefly in the "Prediction" section of this paper. The heat-transfer results computed for  $\alpha = 0^\circ$ ,  $Re_{2,D} = 13700$ , and  $\theta = 0^\circ$  and  $180^\circ$  are compared with measurements in figure 23. The surface temperature was set at  $540^\circ R$  for these computations. The computed results are in very good agreement with the experimental data. At  $\theta = 0^\circ$ , the largest discrepancy is near the shear-layer impingement location where the computed values suggest an impingement that is somewhat closer to the forebody base and less localized than the measurements indicate.

The numerical three-dimensional grid was built up with four domains: one over the forebody face, one in the outer wake, and two in the near-wake region (fig. 9). The streamwise portion of the wake grid near the cylinder surface is aligned with the cylinder, and the other portion is aligned nearly normal to it. To examine grid density effects, the spacing of the normal portion of the grid was reduced to one-half the original spacing for one case. The heating results obtained with this refined grid and the original spacing are compared with the measurements for  $\alpha = -5^\circ$  and  $\theta = 0^\circ$  in figure 24. Results obtained with the refined grid are in better agreement with the measurements except near the shear-layer impingement location. In general, the computed results are within the accuracy of the experimental data.

## Concluding Remarks

Measurements of heating rate and surface streamline directions were made along a cylinder in the near wake of the Aeroassist Flight Experiment (AFE) configuration. Tests were conducted in air at a nominal free-stream Mach number of 10, with postshock Reynolds numbers based on model base height of

6450 to 50 770 and angles of attack of  $5^\circ$ ,  $0^\circ$ ,  $-5^\circ$ , and  $-10^\circ$ . From the results of these tests the following concluding remarks are made. Flow over the cylinder is dominated by impingement of that portion of the free shear layer that originates from the forebody upper (ellipsoid section) surface. The location of impingement is evident by surface streamline directions as indicated by oil flow. Downstream of the impingement region, the oil flow appears similar to that of a swept cylinder in a supersonic stream with cross flow that separates off the cylinder sides to form twin longitudinal counterrotating vortices with reattachment along the "leeside" centerline. The rear stagnation point location (point of upstream- and downstream-directed oil flow in the impingement region) moves upstream with decreasing angle of attack but is not a significant function of Reynolds number. Maximum heating occurs near, but downstream of, the rear stagnation point. The distance between the rear stagnation point and the maximum heating point decreases with decreasing angle of attack and/or increasing Reynolds number. The heating magnitude is greatest along the upper surface, where direct impingement occurs, decreases along the sides, and is least along the lower surface. The magnitude of heating on the top of the cylinder, particularly at the maximum heating point, is significant relative to the computed forebody stagnation point heating. For example, for angles of attack from  $-5^\circ$  to  $5^\circ$ , the corresponding range of heating rate varied from 45 percent to 28 percent of the forebody stagnation point value. Comparisons of heating-rate distributions predicted with a Navier-Stokes computer code are generally in good agreement with the measurements.

NASA Langley Research Center  
Hampton, VA 23665-5225  
September 29, 1989

## References

1. Walberg, Gerald D.: A Review of Aeroassisted Orbit Transfer. AIAA-82-1378, Aug. 1982.
2. Jones, Jim J.: The Rationale for an Aeroassist Flight Experiment. AIAA-87-1508, June 1987.
3. Walberg, G. D.; Siemers, P. M., III; Calloway, R. L.; and Jones, J. J.: The Aeroassist Flight Experiment. IAF Paper 87-197, Oct. 1987.
4. Wells, William L.: Wind-Tunnel Preflight Test Program for Aeroassist Flight Experiment. *Technical Papers—AIAA Atmospheric Flight Mechanics Conference*, 1987, pp. 151-163. (Available as AIAA-87-2367.)
5. Wells, William L.: *Free-Shear-Layer Turning Angle in Wake of Aeroassist Flight Experiment (AFE) Vehicle at Incidence in  $M = 10$  Air and  $M = 6$   $CF_4$* . NASA TM-100479, 1988.
6. Micol, John R.: Experimental and Predicted Pressure and Heating Distributions for an Aeroassist Flight Experiment Vehicle in Air at Mach 10. AIAA-89-1731, June 1989.
7. Micol, John R.: Simulation of Real-Gas Effects on Pressure Distributions for a Proposed Aeroassist Flight Experiment Vehicle and Comparison to Prediction. AIAA-87-2368, Aug. 1987.
8. Berger, Stanley A.: *Laminar Wakes*. American Elsevier Publ. Co., Inc., 1971.
9. Chapman, Dean R.: *Laminar Mixing of a Compressible Fluid*. NACA Rep. 958, 1949. (Supersedes NACA TN 1800.)
10. Hama, Francis R.: *Experimental Investigations of Wedge Base Pressure and Lip Shock*. Tech. Rep. No. 32-1033 (Contract No. NAS7-100), Jet Propulsion Lab., California Inst. of Technology, Dec. 1, 1966. (Available as NASA CR-81031.)
11. Crane, R. I.: A Survey of Hypersonic Near Wake Studies. *Aeronaut. J. Royal Aeronaut. Soc.*, vol. 73, no. 707, Nov. 1969, pp. 998-1006.
12. Shih, Peter Kwang-Tien; and Gay, Archie: Low L/D Aerobrake Heat Transfer Test at Mach 10. AIAA-84-0309, Jan. 1984.
13. Bushnell, Dennis M.: *Local Afterbody Heat Transfer to a Blunt Two-Dimensional Configuration at Mach 8*. NASA TN D-4443, 1968.
14. Gnoffo, Peter A.: A Code Calibration Program in Support of the Aeroassist Flight Experiment. AIAA-89-1673, June 1989.
15. Palmer, Grant: An Efficient, Explicit-Finite Rate Algorithm To Compute Flows in Chemical Nonequilibrium. AIAA-89-0522, June 1989.
16. Tassa, Yehuda; and Conti, Raul J.: Numerical Navier-Stokes Modeling of Hypersonic Laminar Wakes Behind Blunt Cones With Real-Gas Effects. AIAA-87-0374, Jan. 1987.
17. Caruso, S. C.; and Childs, R. E.: Aspects of Grid Topology for Reynolds-Averaged Navier-Stokes Base Flow Computations. AIAA-88-0523, Jan. 1988.
18. Li, Chien-Peng: *Numerical Procedure for Three-Dimensional Hypersonic Viscous Flow Over Aerobrake Configuration*. NASA TM-58269, 1985.
19. Cheatwood, F. McNeil; DeJarnette, Fred R.; and Hamilton, H. Harris, II: *Geometrical Description for a Proposed Aeroassist Flight Experiment Vehicle*. NASA TM-87714, 1986.
20. Miller, C. G.; and Smith, F. M.: Langley Hypersonic Facilities Complex—Description and Application. AIAA-86-0741, Mar. 1986.
21. Miller, Charles G., III: *Comparison of Thin-Film Resistance Heat-Transfer Gages With Thin-Skin Transient Calorimeter Gages in Conventional Hypersonic Wind Tunnels*. NASA TM-83197, 1981.
22. Miller, Charles G., III; Micol, John R.; and Gnoffo, Peter A.: *Laminar Heat-Transfer Distributions on Biconics at Incidence in Hypersonic-Hypervelocity Flows*. NASA TP-2213, 1985.

23. Miller, Charles G., III: *Measured Pressure Distributions, Aerodynamic Coefficients, and Shock Shapes on Blunt Bodies at Incidence in Hypersonic Air and CF<sub>4</sub>*. NASA TM-84489, 1982.
24. Brahinsky, Herbert S.; and Neel, Charles A.: *Tables of Equilibrium Thermodynamic Properties of Air. Volume III. Constant Entropy*. AEDC-TR-69-89, Vol. III, U.S. Air Force, Apr. 1969. (Available from DTIC as AD 687 092.)
25. Fay, J. A.; and Riddell, F. R.: Theory of Stagnation Point Heat Transfer in Dissociated Air. *J. Aeronaut. Sci.*, vol. 25, no. 2, Feb. 1958, pp. 73-85, 121.
26. Peake, David J.; and Tobak, Murray: *Three-Dimensional Interactions and Vortical Flows With Emphasis on High Speeds*. NASA TM-81169, 1980.

Table I. Nominal Test Conditions in the Langley 31-Inch Mach 10 Tunnel

$p_t$ , psi	$T_t$ , °R	$M_\infty$	$p_\infty$ , psia	$T_\infty$ , °R	$Re_\infty$ , ft <sup>-1</sup>	* $Re_{2,D}$	$p_{t,2}$ , psia
150	1800	9.55	0.005	97	$0.25 \times 10^6$	6450	0.54
350	1835	9.74	0.01	96	0.54	13 670	1.17
720	1810	9.90	0.02	92	1.09	26 490	2.23
1450	1800	10.05	0.03	89	2.17	50 770	4.25

\* $D = 3.67$  in.

Table II. AFE Wake-Heating Configuration Run Schedule in Langley 31-Inch Mach 10 Tunnel

(a) Heat transfer, test 212

Run no.	$\theta$ , deg	$\alpha$ , deg	$Re_{2,D}$	$M_\infty$	$U_\infty$ , ft/sec	$p_\infty$ , psi	$T_\infty$ , °R	$T_t$ , °R	$p_t$ , psia
121	0	0	6330	9.55	4613	$4.446 \times 10^{-3}$	96.9	1792	147
123	0	0	23 010	9.88	4747	$1.589 \times 10^{-2}$	95.9	1880	654
125	0	5	6240	9.55	4623	$4.400 \times 10^{-3}$	97.3	1800	146
126	0	5	13 960	9.74	4635	$9.490 \times 10^{-3}$	94.1	1803	350
127	0	5	49 090	10.05	4728	$3.244 \times 10^{-2}$	92.0	1858	1458
128	0	0	49 700	10.05	4695	$3.241 \times 10^{-2}$	90.7	1835	145
129	0	0	13 980	9.74	4633	$9.494 \times 10^{-2}$	93.4	1802	350
130	0	-5	13 500	9.74	4664	$9.287 \times 10^{-3}$	95.2	1824	343
131	0	-5	6280	9.55	4634	$4.446 \times 10^{-3}$	97.8	1807	148
132	0	-10	6330	9.55	4658	$4.532 \times 10^{-3}$	98.8	1824	151
133	0	-10	13 580	9.74	4711	$9.525 \times 10^{-3}$	97.2	1858	354
134	0	-5	49 390	10.05	4704	$3.232 \times 10^{-2}$	91.0	1841	1449
135	0	-10	48 870	10.05	4718	$3.217 \times 10^{-2}$	91.6	1851	1445
136	45	0	14 070	9.74	4622	$9.512 \times 10^{-3}$	93.5	1794	351
138	45	-5	6350	9.55	4643	$4.514 \times 10^{-3}$	98.2	1814	150
139	45	-5	49 820	10.05	4696	$3.250 \times 10^{-2}$	90.7	1835	1456
140	45	0	6610	9.55	4629	$4.672 \times 10^{-3}$	97.6	1803	155
141	45	-10	6100	9.55	4644	$4.344 \times 10^{-3}$	98.2	1814	144
142	45	-10	13 790	9.74	4709	$9.666 \times 10^{-3}$	97.1	1856	359
143	45	5	13 550	9.74	4680	$9.387 \times 10^{-3}$	95.9	1836	348
144	45	5	6220	9.55	4643	$4.423 \times 10^{-3}$	98.2	1813	147
145	45	-5	13 260	9.74	4712	$9.307 \times 10^{-3}$	97.2	1858	346
146	45	0	46 670	10.05	4802	$3.196 \times 10^{-2}$	94.9	1912	145
147	45	5	49 510	10.05	4706	$3.243 \times 10^{-2}$	91.1	1842	1454
148	45	-10	50 160	10.05	4680	$3.249 \times 10^{-2}$	90.1	1824	1454
149	90	-5	6340	9.55	4624	$4.473 \times 10^{-3}$	97.4	1800	148
150	90	0	13 730	9.74	4680	$9.512 \times 10^{-3}$	95.9	1836	352
152	90	-10	13 750	9.74	4671	$9.490 \times 10^{-2}$	95.6	1829	351
153	90	-10	6340	9.55	4620	$4.466 \times 10^{-3}$	97.2	1797	148
154	90	0	6170	9.55	4655	$4.408 \times 10^{-3}$	98.7	1822	147
155	90	5	6360	9.55	4659	$4.554 \times 10^{-3}$	98.9	1825	152
156	90	5	13 200	9.74	4752	$9.415 \times 10^{-3}$	98.9	1887	351
157	90	-5	13 350	9.74	4697	$9.310 \times 10^{-3}$	96.6	1848	345
158	90	0	48 780	10.05	4721	$3.215 \times 10^{-2}$	91.7	1853	1444
159	90	-5	49 210	10.05	4707	$3.225 \times 10^{-2}$	91.2	1843	1447
160	90	-10	50 100	10.05	4672	$3.235 \times 10^{-2}$	89.8	1818	1446
161	90	5	49 850	10.05	4693	$3.248 \times 10^{-2}$	90.6	1833	1455
162	180	0	13 810	9.74	4636	$9.391 \times 10^{-3}$	94.1	1804	346
163	180	5	13 980	9.74	4624	$9.460 \times 10^{-3}$	93.6	1796	349
164	180	0	50 250	10.05	4651	$3.215 \times 10^{-2}$	88.9	1804	1440
165	180	5	50 490	10.05	4645	$3.223 \times 10^{-2}$	88.7	1799	1442

Table II. Concluded

(b) Oil flow, test 212

Run no.	$\alpha$ , deg	$Re_{2,D}$	$M_\infty$	$U_\infty$ , ft/sec	$p_\infty$ , psi	$T_\infty$ , °R	$T_t$ , °R	$p_t$ , psia
187	0	6184	9.55	4623	$4.343 \times 10^{-2}$	97.3	1799	144
189	-5	6034	9.55	4667	$4.324 \times 10^{-3}$	99.2	1831	144
190	0	13 674	9.74	4679	$9.466 \times 10^{-3}$	95.9	1835	351
191	-10	6446	9.55	4624	$4.530 \times 10^{-3}$	97.4	1800	150
192	-10	14 288	9.74	4619	$9.620 \times 10^{-3}$	93.4	1792	355
193	0	50 744	10.05	4646	$3.238 \times 10^{-2}$	88.7	1800	1448
194	-5	14 059	9.74	4645	$9.579 \times 10^{-3}$	94.5	1811	354
195	-5	49 728	10.05	4689	$3.239 \times 10^{-2}$	90.5	1830	1451
196	-10	50 400	10.05	4664	$3.239 \times 10^{-2}$	89.5	1813	1448
197	5	6550	9.55	4644	$4.293 \times 10^{-3}$	98.2	1814	143
201	5	13 683	9.74	4669	$9.421 \times 10^{-3}$	95.5	1828	349
203	5	51 196	10.05	4632	$3.252 \times 10^{-2}$	88.3	1790	1450

Table III. Measured Heat-Transfer Rate at Mach 10 and  $Re_{2,D} = 6500$

(a)  $\theta = 0^\circ$

Gage	$l/D$	Run no. 125 $\alpha = 5^\circ$		Run no. 121 $\alpha = 0^\circ$		Run no. 131 $\alpha = -5^\circ$		Run no. 132 $\alpha = -10^\circ$	
		$T_w$ , °R	$\dot{q}$ , Btu/ft <sup>2</sup> ·sec	$T_w$ , °R	$\dot{q}$ , Btu/ft <sup>2</sup> ·sec	$T_w$ , °R	$\dot{q}$ , Btu/ft <sup>2</sup> ·sec	$T_w$ , °R	$\dot{q}$ , Btu/ft <sup>2</sup> ·sec
1	0.357	535	0.197	538	0.373	540	0.689	545	1.233
2	.399	536	.257	540	.591	544	1.144	553	2.102
3	.439	536	.343	542	.848	549	1.723	560	2.826
4	.480	538	.460	545	1.193	554	2.165	562	3.039
5	.522	540	.613	549	1.503	556	2.368	560	2.939
6	.562	542	.790	551	1.699	556	2.340	558	2.702
7	.603	542	.964	551	1.773	554	2.174	556	2.439
8	.671	545	1.236	553	1.790	553	2.008	556	2.363
9	.710	545	1.312	549	1.694	551	1.923	554	2.324
10	.749	545	1.347	551	1.607	551	1.879	554	2.295
11	.792	547	1.384	551	1.567	551	1.857	554	2.295
12	.831	547	1.379	549	1.509	551	1.839	554	2.280
13	.873	547	1.379	549	1.504	551	1.837	554	2.293
14	.914	547	1.354	549	1.490	551	1.835	554	2.292
15	.979	545	1.294	549	1.462	551	1.807	554	2.285
16	1.023	545	1.274	549	1.459	551	1.808	554	2.300
17	1.065	545	1.245	549	1.445	551	1.798	556	2.301
18	1.104	545	1.224	549	1.443	551	1.798	556	2.326
19	1.144	545	1.194	549	1.434	551	1.784	556	2.332
20	1.184	545	1.168	549	1.432	551	1.783	556	2.351
21	1.226	545	1.168	549	1.432	551	1.783	556	2.360

(b)  $\theta = 45^\circ$

Gage	$l/D$	Run no. 144 $\alpha = 5^\circ$		Run no. 140 $\alpha = 0^\circ$		Run no. 138 $\alpha = -5^\circ$		Run no. 141 $\alpha = -10^\circ$	
		$T_w$ , °R	$\dot{q}$ , Btu/ft <sup>2</sup> ·sec	$T_w$ , °R	$\dot{q}$ , Btu/ft <sup>2</sup> ·sec	$T_w$ , °R	$\dot{q}$ , Btu/ft <sup>2</sup> ·sec	$T_w$ , °R	$\dot{q}$ , Btu/ft <sup>2</sup> ·sec
1	0.358	538	0.163	538	0.263	542	0.504	544	0.795
2	.401	538	.202	540	.386	545	.800	549	1.313
3	.439	540	.261	542	.576	549	1.207	553	1.839
4	.481	540	.331	544	.794	553	1.554	556	2.121
5	.523	542	.434	547	1.041	554	1.781	556	2.169
6	.563	542	.546	549	1.249	554	1.824	556	2.046
7	.605	544	.670	551	1.400	554	1.775	554	1.888
8	.673	545	.888	551	1.474	553	1.598	553	1.683
9	.711	547	.977	551	1.408	551	1.478	551	1.590
10	.751	547	1.061	551	1.371	551	1.417	551	1.573
11	.793	547	1.147	551	1.343	551	1.391	551	1.583
12	.833	549	1.168	549	1.278	551	1.360	551	1.559
13	.874	549	1.176	549	1.249	551	1.360	551	1.570
14	.915	547	1.159	549	1.196	551	1.344	551	1.546
15	.981	547	1.101	547	1.136	551	1.317	551	1.518
16	1.024	547	1.076	547	1.135	551	1.318	551	1.541
17	1.066	547	1.041	547	1.095	551	1.307	551	1.522
18	1.105	547	1.014	547	1.089	551	1.299	551	1.540
19	1.145	547	.975	547	1.066	549	1.274	551	1.519
20	1.186	545	.949	547	1.046	549	1.279	551	1.537
21	1.227	545	.931	547	1.047	549	1.267	551	1.537

Table III. Concluded

(c)  $\theta = 90^\circ$ 

Gage	$l/D$	Run no. 155 $\alpha = 5^\circ$		Run no. 154 $\alpha = 0^\circ$		Run no. 149 $\alpha = -5^\circ$		Run no. 153 $\alpha = -10^\circ$	
		$T_w$ , $^\circ\text{R}$	$\dot{q}$ , $\text{Btu}/\text{ft}^2\cdot\text{sec}$	$T_w$ , $^\circ\text{R}$	$\dot{q}$ , $\text{Btu}/\text{ft}^2\cdot\text{sec}$	$T_w$ , $^\circ\text{R}$	$\dot{q}$ , $\text{Btu}/\text{ft}^2\cdot\text{sec}$	$T_w$ , $^\circ\text{R}$	$\dot{q}$ , $\text{Btu}/\text{ft}^2\cdot\text{sec}$
1	0.360	536	0.120	536	0.164	536	0.213	538	0.295
2	.402	536	.136	538	.201	538	.298	540	.424
3	.441	538	.156	538	.258	540	.433	542	.584
4	.483	538	.179	538	.328	540	.563	542	.698
5	.524	538	.218	540	.424	542	.693	544	.776
6	.565	538	.259	542	.526	544	.780	544	.793
7	.606	538	.297	542	.646	544	.833	544	.790
8	.674	540	.384	544	.776	544	.793	542	.695
9	.713	540	.432	544	.801	542	.722	542	.616
10	.752	542	.501	544	.828	542	.687	542	.595
11	.795	542	.609	544	.856	542	.666	542	.606
12	.834	542	.676	544	.828	542	.631	542	.589
13	.876	544	.735	544	.806	542	.617	542	.598
14	.917	544	.773	544	.770	542	.591	542	.577
15	.982	544	.796	542	.709	540	.564	540	.553
16	1.026	544	.806	542	.686	540	.562	540	.555
17	1.067	544	.798	542	.652	540	.533	540	.526
18	1.107	544	.784	542	.635	540	.528	540	.524
19	1.146	544	.754	542	.606	540	.515	540	.511
20	1.187	544	.740	542	.589	540	.509	540	.508
21	1.229	544	.714	542	.581	540	.502	540	.512

Table IV. Measured Heat-Transfer Rate at Mach 10 and  $Re_{2,D} = 13700$

(a)  $\theta = 0^\circ$

Gage	$l/D$	Run no. 126 $\alpha = 5^\circ$		Run no. 129 $\alpha = 0^\circ$		Run no. 130 $\alpha = -5^\circ$		Run no. 133 $\alpha = -10^\circ$	
		$T_w$ , °R	$\dot{q}$ , Btu/ft <sup>2</sup> ·sec	$T_w$ , °R	$\dot{q}$ , Btu/ft <sup>2</sup> ·sec	$T_w$ , °R	$\dot{q}$ , Btu/ft <sup>2</sup> ·sec	$T_w$ , °R	$\dot{q}$ , Btu/ft <sup>2</sup> ·sec
1	0.357	535	0.209	536	0.391	542	1.090	560	2.439
2	.399	536	.262	538	.611	551	2.084	576	4.217
3	.439	536	.362	542	1.005	562	3.099	581	4.717
4	.480	538	.519	547	1.567	567	3.599	578	4.344
5	.522	540	.764	553	2.164	565	3.560	574	3.899
6	.562	544	1.090	556	2.578	563	3.266	569	3.386
7	.603	547	1.449	558	2.721	560	2.917	567	3.145
8	.671	553	1.998	558	2.709	558	2.648	567	3.216
9	.710	554	2.151	556	2.553	556	2.532	567	3.188
10	.749	554	2.211	556	2.427	556	2.504	567	3.177
11	.792	554	2.211	554	2.335	556	2.511	567	3.204
12	.831	554	2.152	554	2.239	556	2.501	567	3.201
13	.873	554	2.109	553	2.191	556	2.524	567	3.222
14	.914	553	2.042	553	2.135	556	2.524	567	3.228
15	.979	553	1.924	553	2.050	556	2.497	567	3.213
16	1.023	551	1.885	553	2.036	556	2.515	569	3.243
17	1.065	551	1.843	553	1.994	556	2.504	569	3.257
18	1.104	551	1.815	553	1.998	556	2.512	569	3.291
19	1.144	551	1.781	551	1.976	556	2.479	569	3.300
20	1.184	551	1.752	551	1.961	556	2.444	569	3.333
21	1.226	551	1.727	551	1.942	556	2.483	569	3.345

(b)  $\theta = 45^\circ$

Gage	$l/D$	Run no. 143 $\alpha = 5^\circ$		Run no. 136 $\alpha = 0^\circ$		Run no. 145 $\alpha = -5^\circ$		Run no. 142 $\alpha = -10^\circ$	
		$T_w$ , °R	$\dot{q}$ , Btu/ft <sup>2</sup> ·sec	$T_w$ , °R	$\dot{q}$ , Btu/ft <sup>2</sup> ·sec	$T_w$ , °R	$\dot{q}$ , Btu/ft <sup>2</sup> ·sec	$T_w$ , °R	$\dot{q}$ , Btu/ft <sup>2</sup> ·sec
1	0.358	535	0.183	538	0.316	545	0.758	551	1.561
2	.401	536	.217	540	.443	551	1.358	563	2.792
3	.439	536	.281	542	.697	558	2.157	569	3.537
4	.481	538	.380	545	1.052	563	2.720	569	3.514
5	.523	540	.545	549	1.530	565	2.929	567	3.170
6	.563	542	.770	554	1.953	563	2.802	563	2.755
7	.605	545	1.076	556	2.225	562	2.591	560	2.451
8	.673	549	1.559	556	2.295	560	2.229	558	2.291
9	.711	551	1.782	554	2.161	556	2.046	558	2.228
10	.751	553	1.961	554	2.026	556	1.956	558	2.223
11	.793	554	2.050	553	1.922	556	1.941	558	2.257
12	.833	553	2.022	553	1.827	556	1.907	558	2.250
13	.874	553	1.961	551	1.758	556	1.919	558	2.260
14	.915	553	1.863	551	1.687	556	1.902	558	2.233
15	.981	551	1.675	551	1.589	556	1.872	558	2.211
16	1.024	549	1.599	551	1.567	556	1.885	558	2.235
17	1.066	549	1.530	549	1.530	556	1.856	558	2.217
18	1.105	549	1.472	549	1.507	556	1.845	558	2.228
19	1.145	547	1.409	549	1.479	554	1.819	558	2.207
20	1.186	547	1.378	549	1.478	556	1.824	558	2.237
21	1.227	547	1.346	549	1.451	554	1.809	558	2.228

Table IV. Concluded

(c)  $\theta = 90^\circ$ 

Gage	$\ell/D$	Run no. 156 $\alpha = 5^\circ$		Run no. 150 $\alpha = 0^\circ$		Run no. 157 $\alpha = -5^\circ$		Run no. 152 $\alpha = -10^\circ$	
		$T_w$ , °R	$\dot{q}$ , Btu/ft <sup>2</sup> ·sec	$T_w$ , °R	$\dot{q}$ , Btu/ft <sup>2</sup> ·sec	$T_w$ , °R	$\dot{q}$ , Btu/ft <sup>2</sup> ·sec	$T_w$ , °R	$\dot{q}$ , Btu/ft <sup>2</sup> ·sec
1	0.360	538	0.149	540	0.215	540	0.314	542	0.447
2	.402	538	.169	540	.239	540	.445	545	.729
3	.441	538	.197	540	.291	544	.678	549	1.077
4	.483	538	.228	542	.389	545	.945	551	1.271
5	.524	538	.277	544	.545	549	1.217	551	1.327
6	.565	540	.333	545	.741	549	1.327	549	1.227
7	.606	540	.400	547	.984	549	1.329	549	1.136
8	.674	542	.562	551	1.219	547	1.192	547	.920
9	.713	544	.681	551	1.275	547	1.083	545	.818
10	.752	545	.830	551	1.319	545	.995	545	.801
11	.795	547	1.038	551	1.316	545	.950	545	.822
12	.834	549	1.173	549	1.237	545	.886	545	.806
13	.876	549	1.277	549	1.175	545	.861	545	.811
14	.917	549	1.370	549	1.099	545	.833	545	.791
15	.982	549	1.379	547	.992	544	.792	545	.760
16	1.026	549	1.345	547	.965	544	.784	545	.756
17	1.067	549	1.274	547	.906	544	.764	545	.723
18	1.107	549	1.247	547	.884	544	.750	545	.723
19	1.146	547	1.148	545	.846	544	.720	544	.709
20	1.187	547	1.097	545	.816	544	.718	544	.710
21	1.229	547	1.038	545	.812	544	.698	544	.710

(d)  $\theta = 180^\circ$ 

Gage	$\ell/D$	Run no. 163 $\alpha = 5^\circ$		Run no. 162 $\alpha = 0^\circ$	
		$T_w$ , °R	$\dot{q}$ , Btu/ft <sup>2</sup> ·sec	$T_w$ , °R	$\dot{q}$ , Btu/ft <sup>2</sup> ·sec
1	0.362	545	0.078	540	0.086
2	.405	545	.082	540	.094
3	.444	545	.081	540	.094
4	.486	545	.095	540	.115
5	.527	545	.119	540	.120
6	.568	545	.140	540	.143
7	.609	545	.136	540	.150
8	.677	545	.181	540	.193
9	.716	545	.198	540	.189
10	.755	547	.216	540	.230
11	.798	547	.249	542	.285
12	.837	547	.279	542	.328
13	.879	547	.310	542	.394
14	.920	547	.353	544	.455
15	.985	549	.417	544	.562
16	1.029	549	.466	545	.638
17	1.070	549	.530	545	.711
18	1.110	551	.589	545	.794
19	1.149	551	.653	547	.875
20	1.190	551	.728	547	.935
21	1.232	553	.820	549	1.026

Table V. Measured Heat-Transfer Rate at Mach 10 and  $Re_{2,D} = 26\,500$

$$\theta = 0^\circ$$

Gage	$l/D$	Run no. 123 $\alpha = 0^\circ$	
		$T_w,$ $^\circ R$	$\dot{q},$ Btu/ft <sup>2</sup> ·sec
1	0.357	538	.531
2	.399	542	.953
3	.439	549	1.693
4	.480	560	2.799
5	.522	569	3.847
6	.562		
7	.603	574	4.258
8	.671	571	3.941
9	.710	569	3.653
10	.749	567	3.473
11	.792	565	3.348
12	.831	565	3.228
13	.873	565	3.188
14	.914	563	3.134
15	.979	563	3.014
16	1.023	563	2.992
17	1.065	562	2.963
18	1.104	562	2.954
19	1.144	562	2.905
20	1.184	562	2.857
21	1.226		

Table VI. Measured Heat-Transfer Rate at Mach 10 and  $Re_{2,D} = 50800$ (a)  $\theta = 0^\circ$ 

Gage	$\ell/D$	Run no. 127 $\alpha = 5^\circ$		Run no. 128 $\alpha = 0^\circ$		Run no. 134 $\alpha = -5^\circ$		Run no. 135 $\alpha = -10^\circ$	
		$T_w$ , °R	$\dot{q}$ , Btu/ft <sup>2</sup> ·sec	$T_w$ , °R	$\dot{q}$ , Btu/ft <sup>2</sup> ·sec	$T_w$ , °R	$\dot{q}$ , Btu/ft <sup>2</sup> ·sec	$T_w$ , °R	$\dot{q}$ , Btu/ft <sup>2</sup> ·sec
1	0.357	538	0.379	542	0.648	563	2.758	616	8.527
2	.399	538	.474	547	1.078	594	6.053	630	10.045
3	.439	542	.659	558	2.139	610	7.695	616	8.334
4	.480	545	1.001	578	4.051	607	7.211	605	7.017
5	.522	553	1.691	596	6.063	599	6.424	596	6.149
6	.562	563	2.844	601	6.639	592	5.734	592	5.736
7	.603	578	4.332	598	6.258	589	5.304	590	5.576
8	.671	592	5.916	590	5.630	587	5.193	592	5.845
9	.710	592	5.970	587	5.206	585	5.022	592	5.831
10	.749	590	5.714	585	4.913	585	4.960	592	5.857
11	.792	589	5.366	581	4.728	585	4.948	592	5.860
12	.831	585	5.000	581	4.548	585	4.926	592	5.880
13	.873	581	4.726	580	4.484	585	4.973	594	5.944
14	.914	580	4.478	580	4.397	585	4.971	594	5.963
15	.979	576	4.104	578	4.232	583	4.911	594	5.927
16	1.023	574	3.992	578	4.195	583	4.932	594	5.996
17	1.065	574	3.883	578	4.153	583	4.920	594	6.013
18	1.104	572	3.791	576	4.129	583	4.910	594	6.064
19	1.144	572	3.682	576	4.082	583	4.864	594	6.088
20	1.184	571	3.595	576	4.054	583	4.862	596	6.183
21	1.226	571	3.502	576	3.990	583	4.808	594	6.101

(b)  $\theta = 45^\circ$ 

Gage	$\ell/D$	Run no. 147 $\alpha = 5^\circ$		Run no. 146 $\alpha = 0^\circ$		Run no. 139 $\alpha = -5^\circ$		Run no. 148 $\alpha = -10^\circ$	
		$T_w$ , °R	$\dot{q}$ , Btu/ft <sup>2</sup> ·sec	$T_w$ , °R	$\dot{q}$ , Btu/ft <sup>2</sup> ·sec	$T_w$ , °R	$\dot{q}$ , Btu/ft <sup>2</sup> ·sec	$T_w$ , °R	$\dot{q}$ , Btu/ft <sup>2</sup> ·sec
1	0.358	540	0.348	544	0.544	556	1.618	589	5.142
2	.401	542	.414	547	.790	568	3.930	614	7.787
3	.439	544	.534	554	1.450	599	5.949	607	6.941
4	.481	545	.712	569	2.844	601	6.360	592	5.553
5	.523	549	1.059	589	4.827	596	5.589	585	4.801
6	.563	556	1.687	598	5.805	589	4.836	581	4.375
7	.605	567	2.668	596	5.583	583	4.315	580	4.182
8	.673	581	4.207	587	4.741	578	3.932	578	4.062
9	.711	585	4.615	583	4.306	576	3.739	578	3.980
10	.751	587	4.704	580	4.058	576	3.656	576	3.969
11	.793	585	4.637	578	3.865	576	3.624	578	4.037
12	.833	583	4.439	576	3.663	574	3.586	578	4.029
13	.874	580	4.258	576	3.561	576	3.601	578	4.085
14	.915	578	4.013	574	3.448	574	3.557	578	4.052
15	.981	574	3.685	572	3.312	574	3.522	578	4.045
16	1.024	572	3.528	572	3.279	574	3.526	578	4.041
17	1.066	571	3.343	571	3.179	574	3.450	576	3.992
18	1.105	569	3.205	571	3.149	572	3.433	576	3.999
19	1.145	567	3.069	571	3.081	572	3.369	576	3.981
20	1.186	567	2.991	571	3.086	572	3.395	578	4.034
21	1.227	565	2.885	569	3.042	572	3.307	576	3.964

Table VI. Concluded

(c)  $\theta = 90^\circ$ 

Gage	$\ell/D$	Run no. 161 $\alpha = 5^\circ$		Run no. 158 $\alpha = 0^\circ$		Run no. 159 $\alpha = -5^\circ$		Run no. 160 $\alpha = -10^\circ$	
		$T_w$ , °R	$\dot{q}$ , Btu/ft <sup>2</sup> ·sec	$T_w$ , °R	$\dot{q}$ , Btu/ft <sup>2</sup> ·sec	$T_w$ , °R	$\dot{q}$ , Btu/ft <sup>2</sup> ·sec	$T_w$ , °R	$\dot{q}$ , Btu/ft <sup>2</sup> ·sec
1	0.360	538	0.287	540	0.314	544	0.567	547	1.212
2	.402	538	.322	540	.365	547	.913	558	2.226
3	.441	540	.369	542	.437	556	1.842	565	3.018
4	.483	540	.429	544	.567	567	2.863	562	2.662
5	.524	542	.525	547	.918	571	3.316	558	2.217
6	.565	544	.652	554	1.614	565	2.790	554	1.908
7	.606	545	.886	563	2.604	562	2.348	554	1.782
8	.674	553	1.584	569	3.175	558	2.000	551	1.585
9	.713	558	2.187	565	2.809	556	1.840	551	1.492
10	.752	563	2.743	560	2.338	554	1.758	551	1.483
11	.795	569	3.065	558	2.052	554	1.706	551	1.478
12	.834	569	3.073	556	1.894	554	1.635	551	1.442
13	.876	567	2.969	556	1.842	553	1.595	551	1.414
14	.917	565	2.757	554	1.775	553	1.540	549	1.383
15	.982	562	2.421	554	1.675	553	1.473	549	1.334
16	1.026	560	2.278	553	1.623	551	1.449	549	1.317
17	1.067	558	2.141	553	1.553	551	1.394	549	1.264
18	1.107	558	2.058	553	1.520	551	1.372	549	1.261
19	1.146	556	1.971	551	1.467	551	1.326	547	1.227
20	1.187	556	1.922	551	1.443	551	1.321	549	1.232
21	1.229	554	1.826	551	1.397	549	1.286	547	1.225

(d)  $\theta = 180^\circ$ 

Gage	$\ell/D$	Run no. 165 $\alpha = 5^\circ$		Run no. 164 $\alpha = 0^\circ$	
		$T_w$ , °R	$\dot{q}$ , Btu/ft <sup>2</sup> ·sec	$T_w$ , °R	$\dot{q}$ , Btu/ft <sup>2</sup> ·sec
1	0.362	540	0.067	542	0.218
2	.405	540	.099	542	.289
3	.444	540	.147	544	.358
4	.486	542	.193	544	.400
5	.527	542	.252	544	.428
6	.568	542	.308	544	.433
7	.609	542	.332	544	.426
8	.677	544	.377	544	.457
9	.716	544	.371	544	.467
10	.755	544	.385	544	.499
11	.798	544	.427	545	.586
12	.837	544	.493	547	.718
13	.879	545	.577	547	.890
14	.920	547	.689	551	1.093
15	.985	549	.920	553	1.427
16	1.029	551	1.116	554	1.619
17	1.070	553	1.346	558	1.813
18	1.110	554	1.610	560	1.986
19	1.149	558	1.890	560	2.145
20	1.190	560	2.176	562	2.265
21	1.232	563	2.495	563	2.419

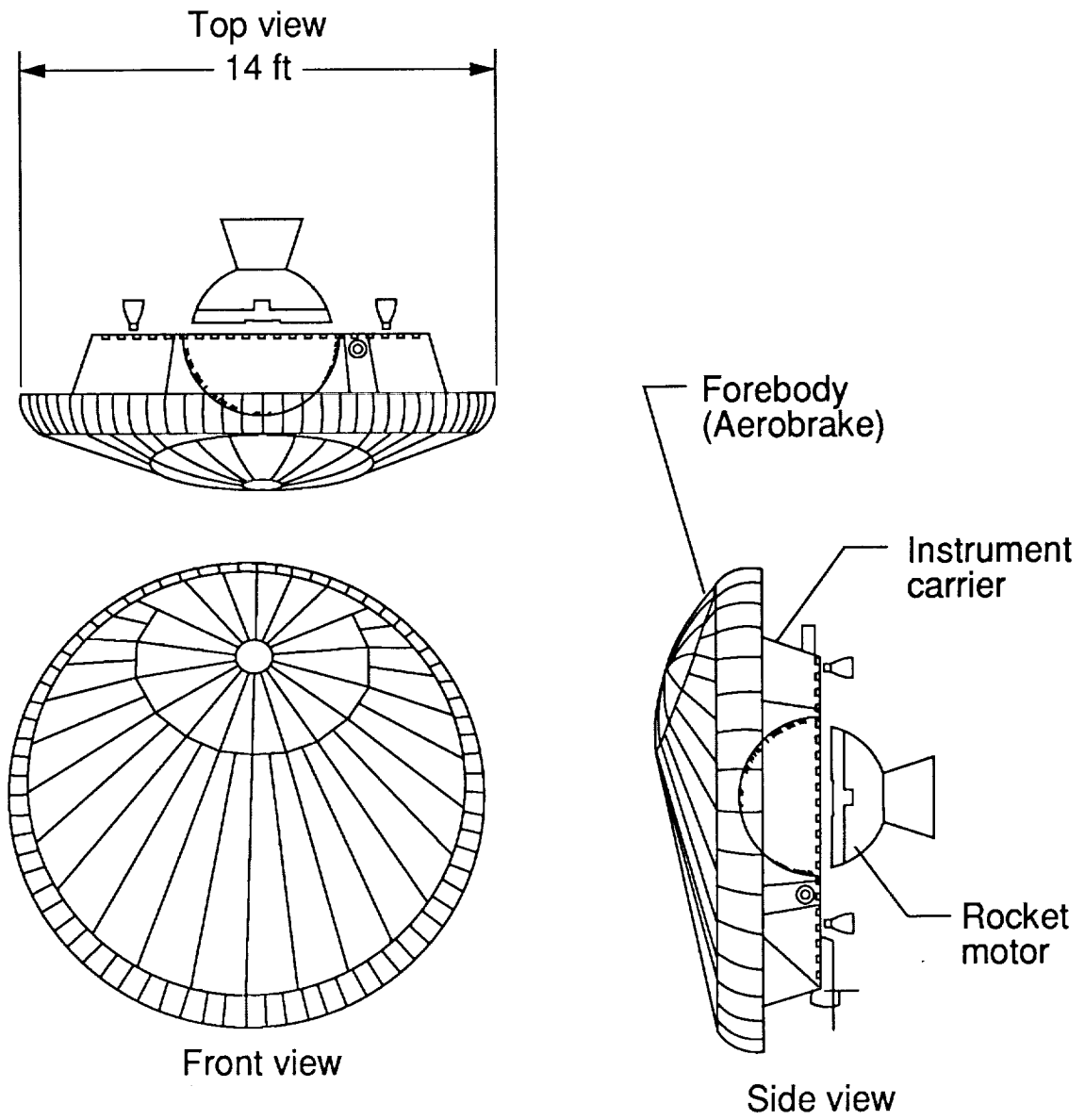


Figure 1. AFE vehicle configuration.

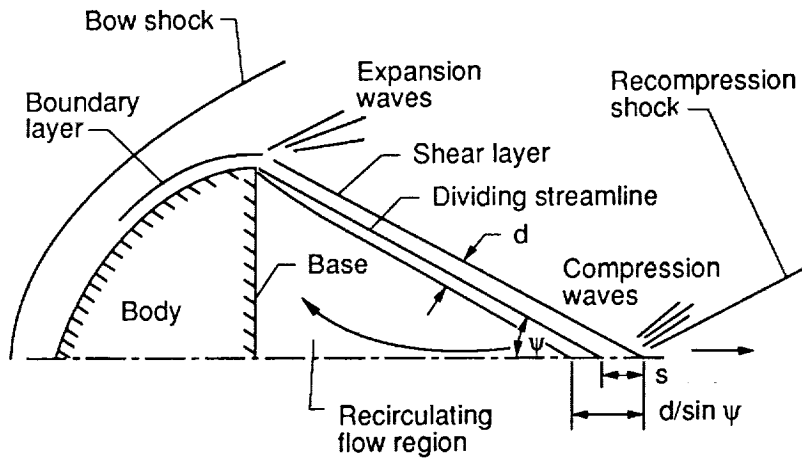


Figure 2. Simplified model of near-wake flow for blunt body in hypersonic free stream.

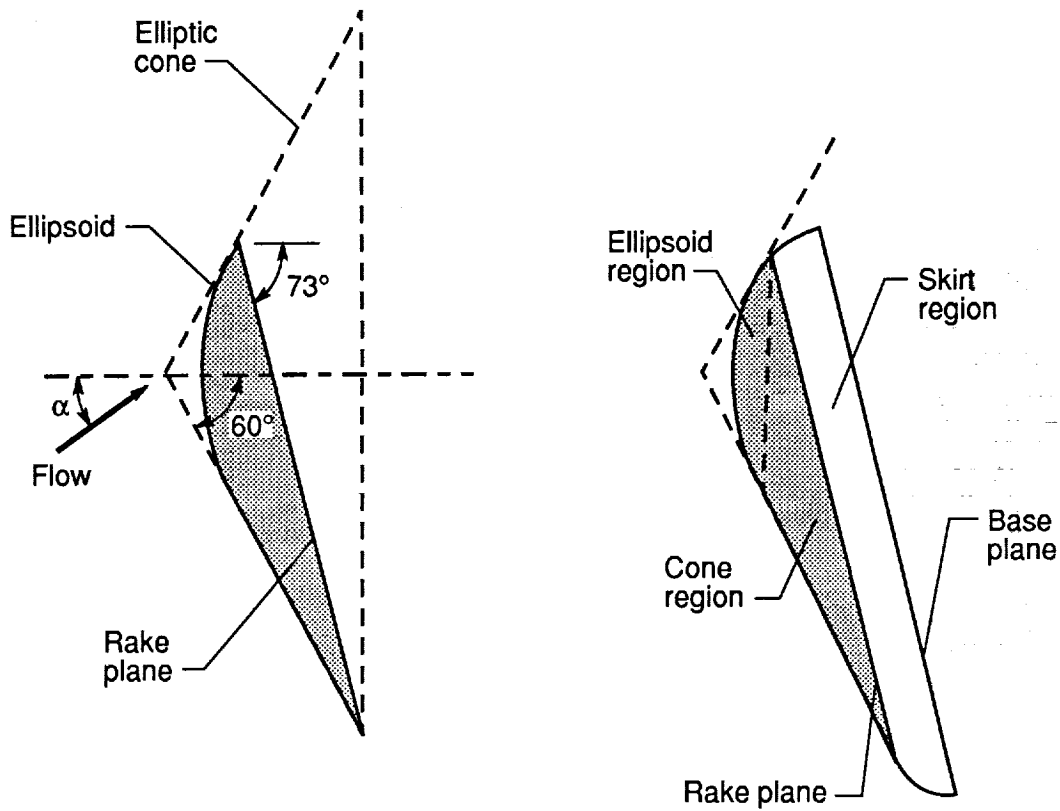


Figure 3. Development of AFE vehicle forebody from elliptic cone.

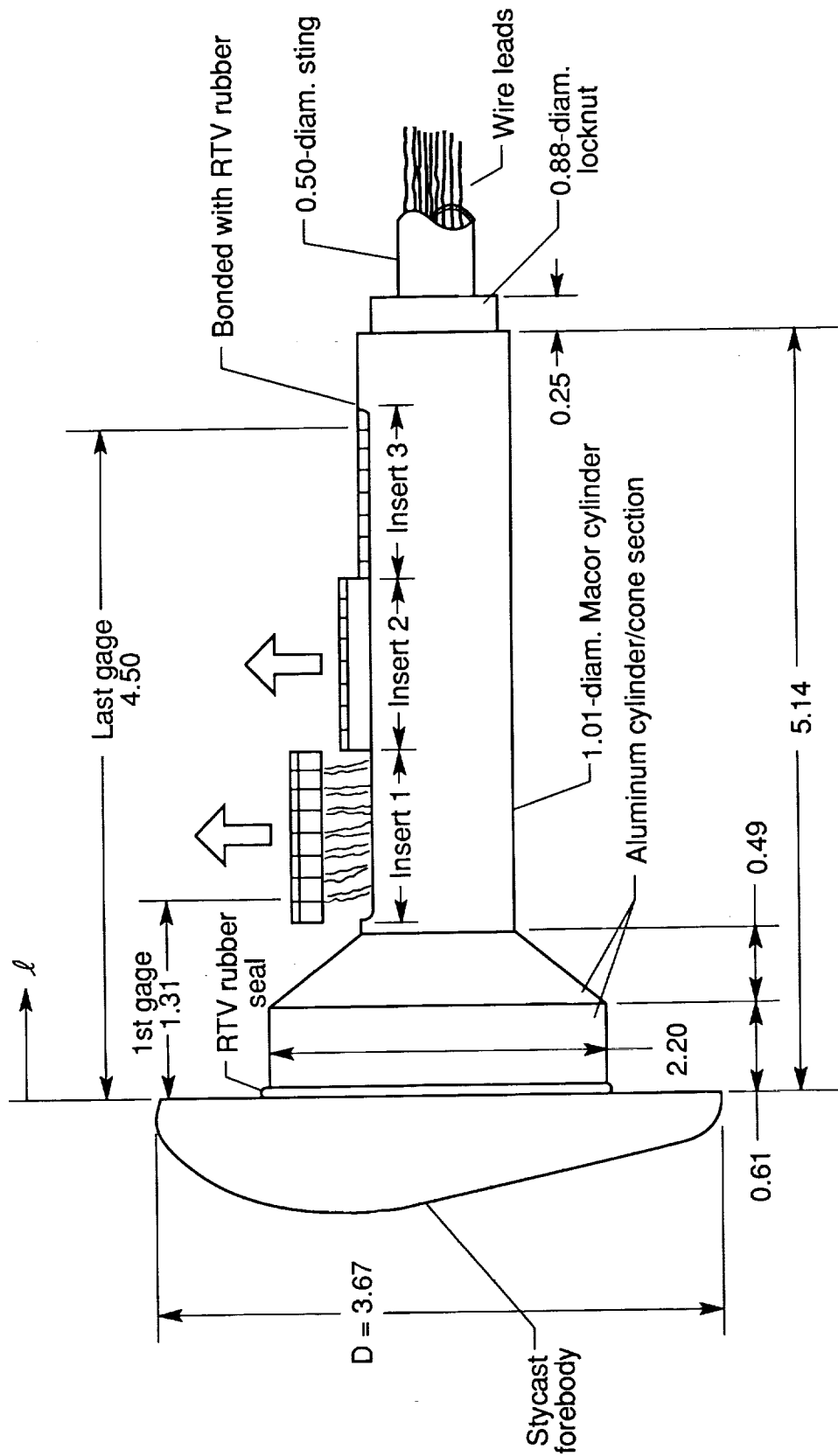
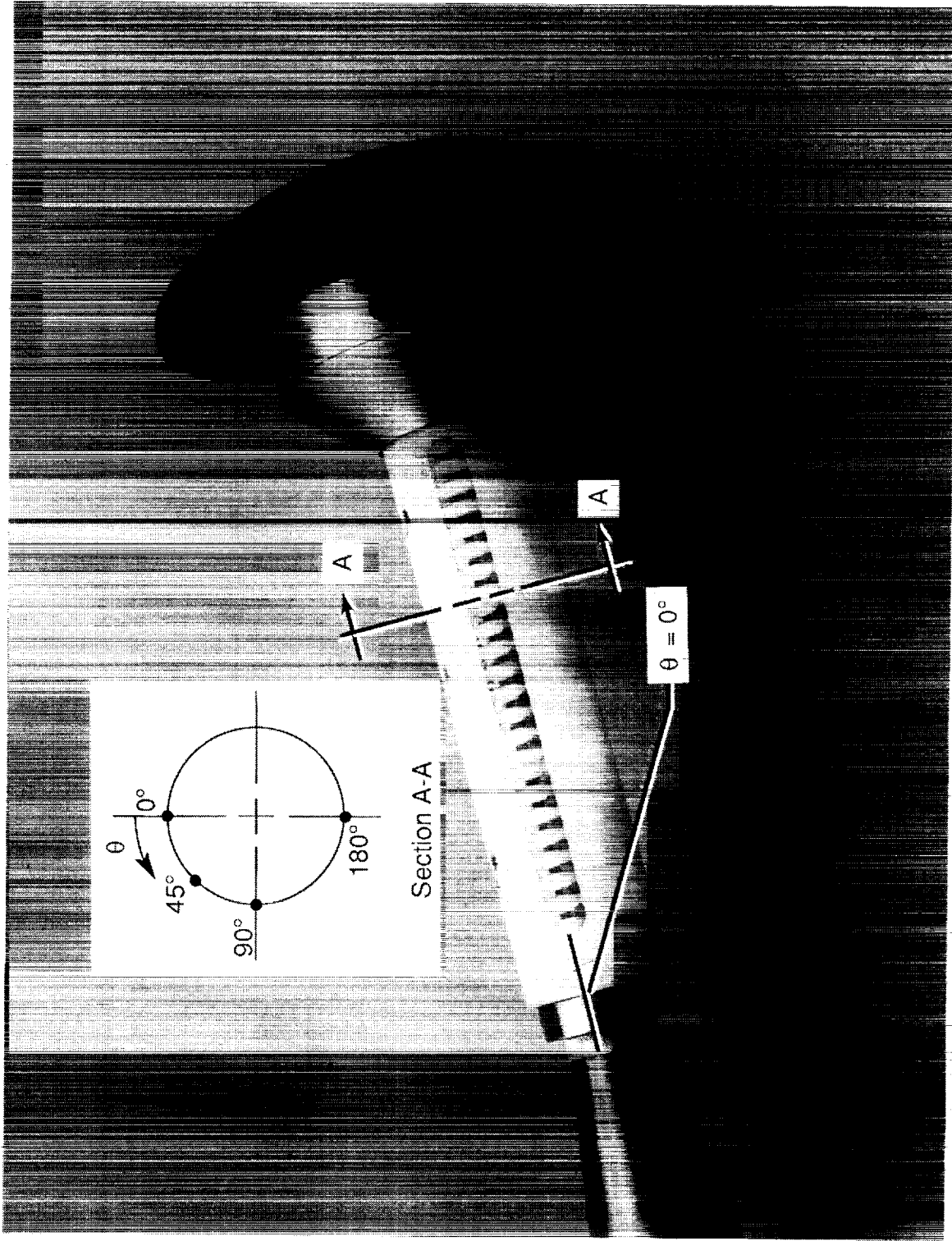


Figure 4. Sketch of AFE wake-heating-study model showing resistance gage inserts partially removed. Dimensions are in inches.

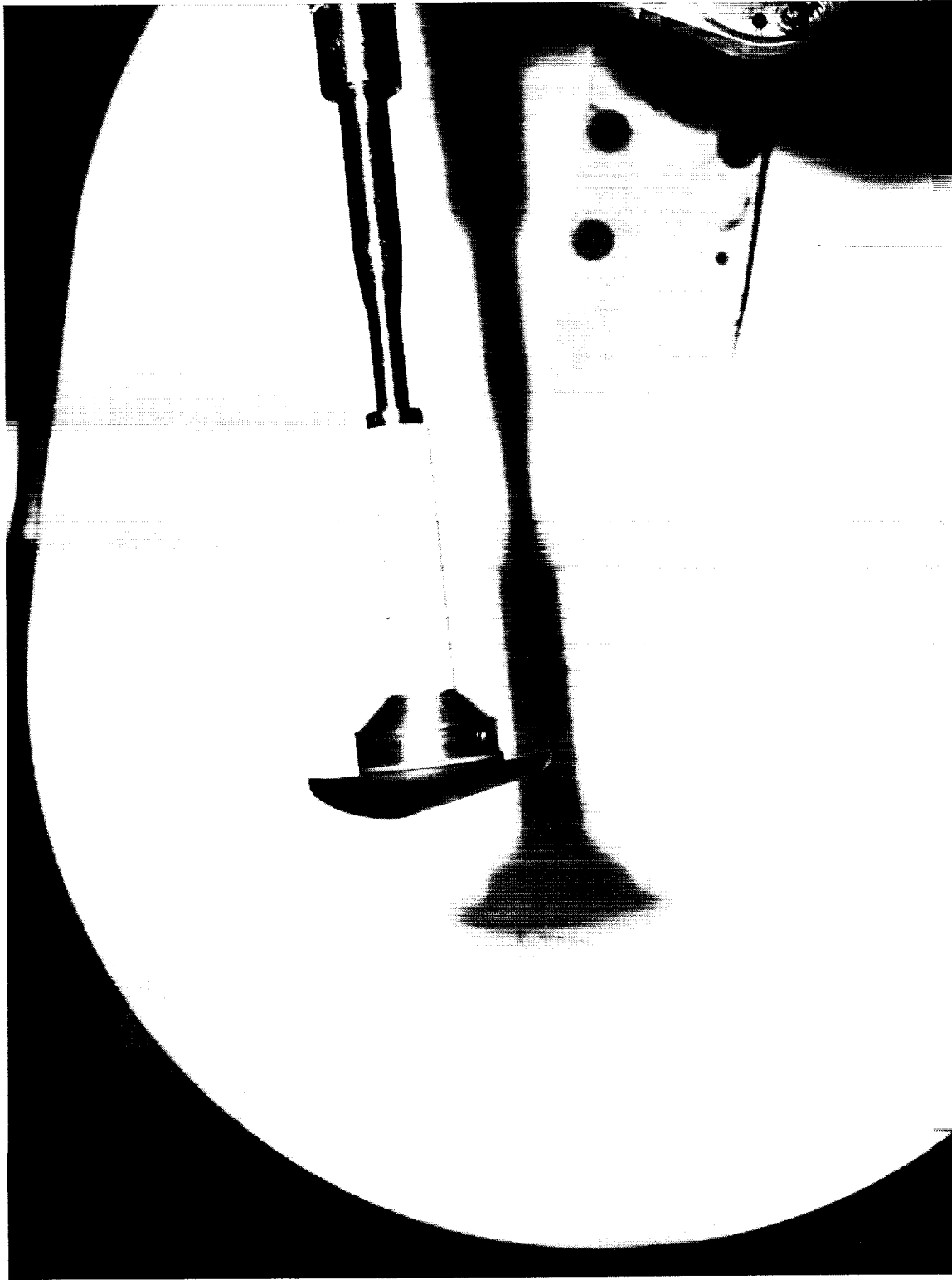
ORIGINAL FILE  
 DRAWN BY: [unreadable]

(a) Location of heat-transfer gage array. Section A-A shows other possible locations.

Figure 5. Photographs of AFE wake-heating-study model.



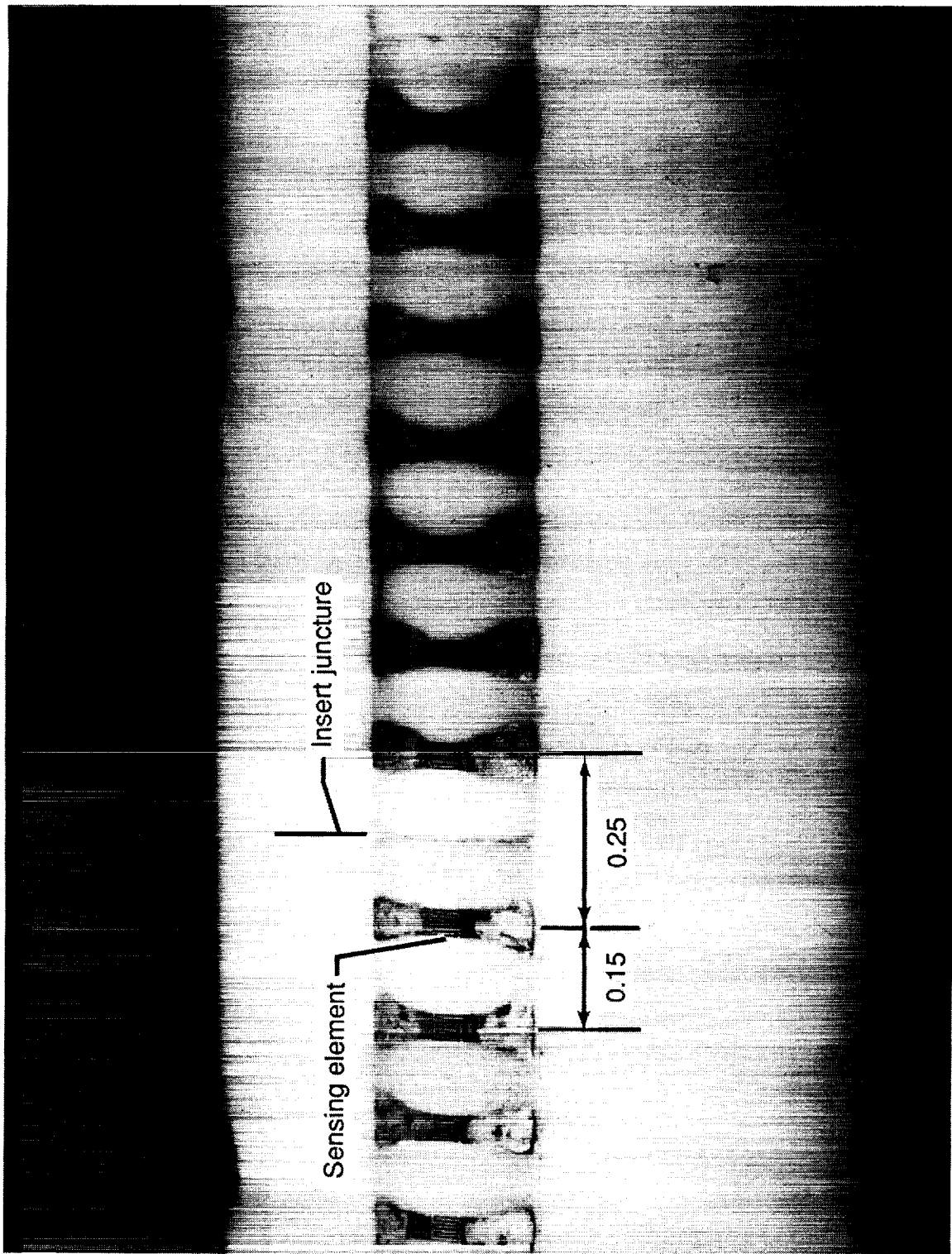
ORIGINAL PAGE  
BLACK AND WHITE PHOTOGRAPH



L-87-6217

(b) Model mounted in Langley 31-Inch Mach 10 Tunnel.

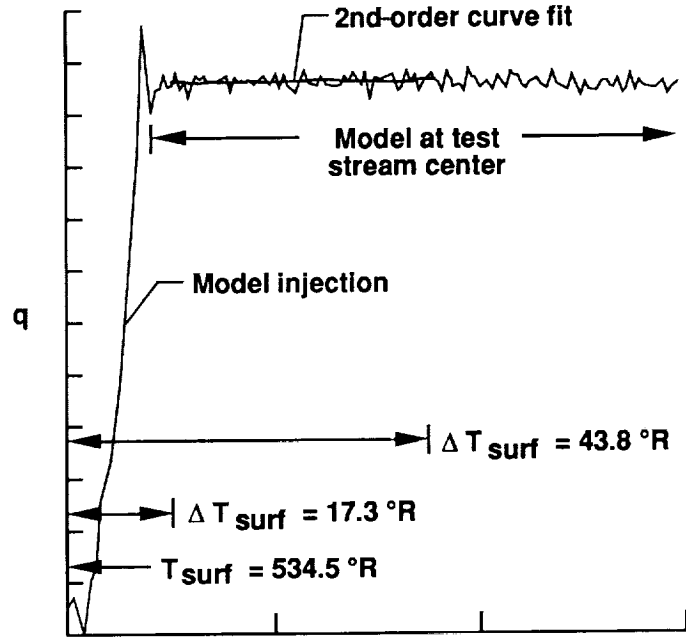
Figure 5. Concluded.



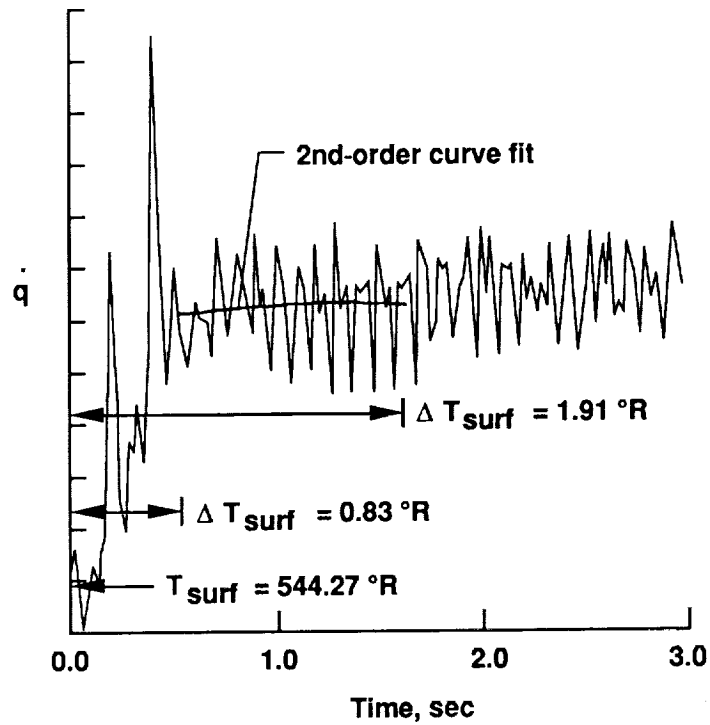
L-88-5341

Figure 6. Photographic enlargement of thin-film resistance gages on AFE wake-heating-study model. Spacing dimensions in inches.

ORIGINAL PAGE  
BLACK AND WHITE PHOTOGRAPH

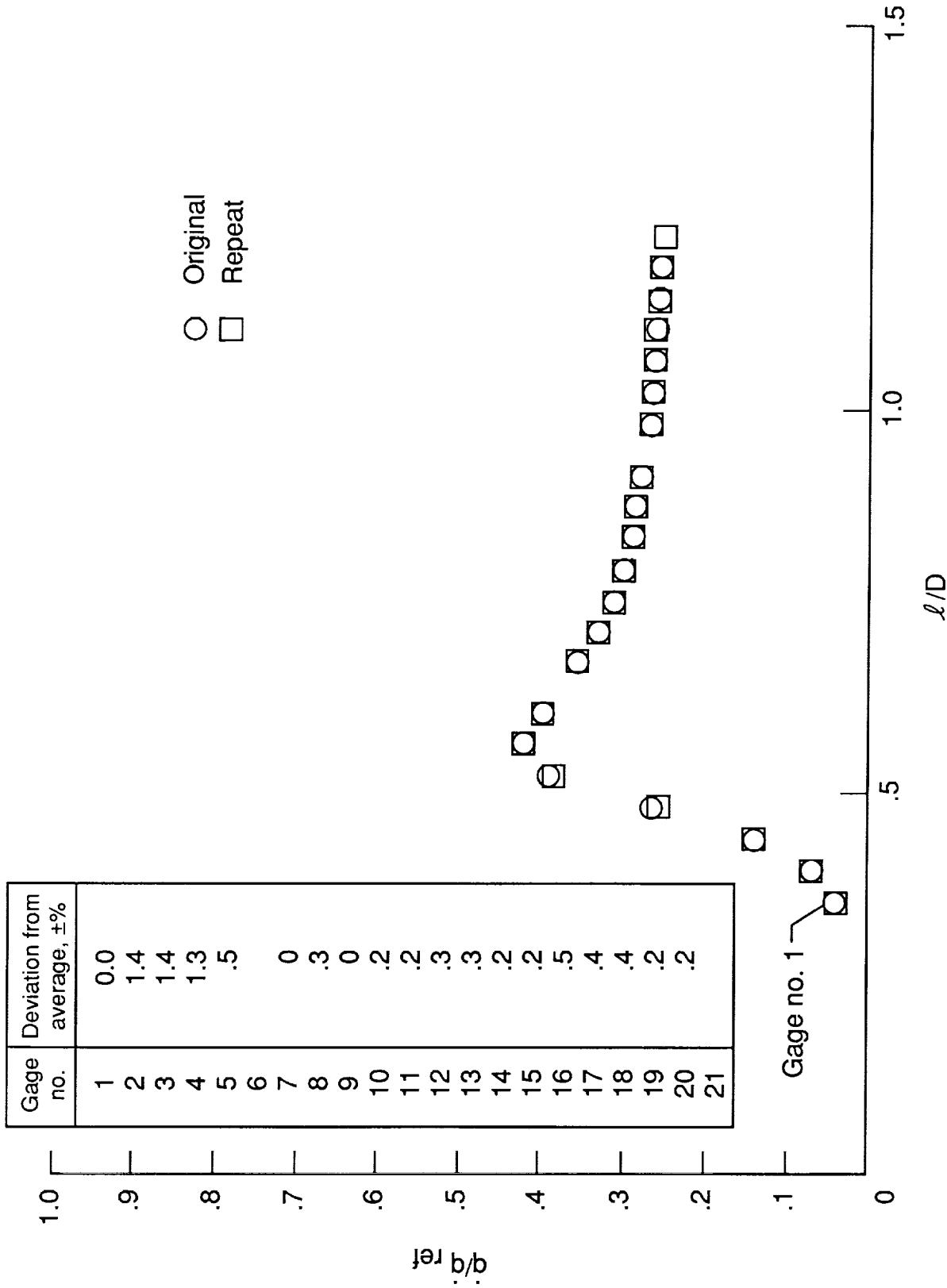


(a) Example of high-heating signal.  $\alpha = -10^\circ$ ;  $\theta = 0^\circ$ .



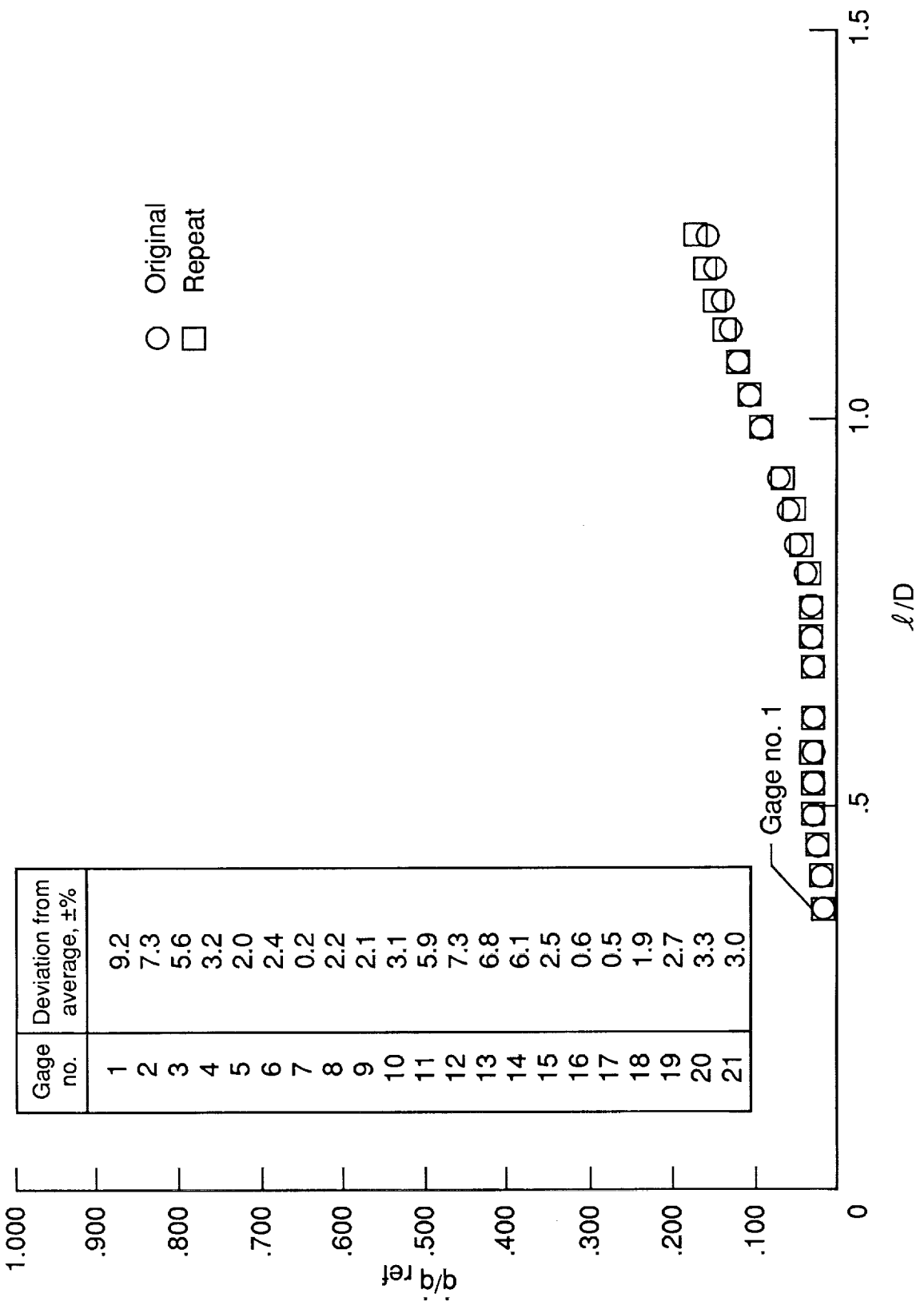
(b) Example of very low-heating signal.  $\alpha = 5^\circ$ ;  $\theta = 180^\circ$ .

Figure 7. Heating-rate time histories indicating range of signal-to-noise ratios of thin-film gages in present tests.  $Re_{2,D} = 13700$ .



(a)  $\theta = 0^\circ$ .

Figure 8. Examples of run-to-run repeatability of heat-transfer rates.  $Re_{2,D} = 50\,500$ ;  $\alpha = 0^\circ$ .



(b)  $\theta = 180^\circ$ .

Figure 8. Concluded.

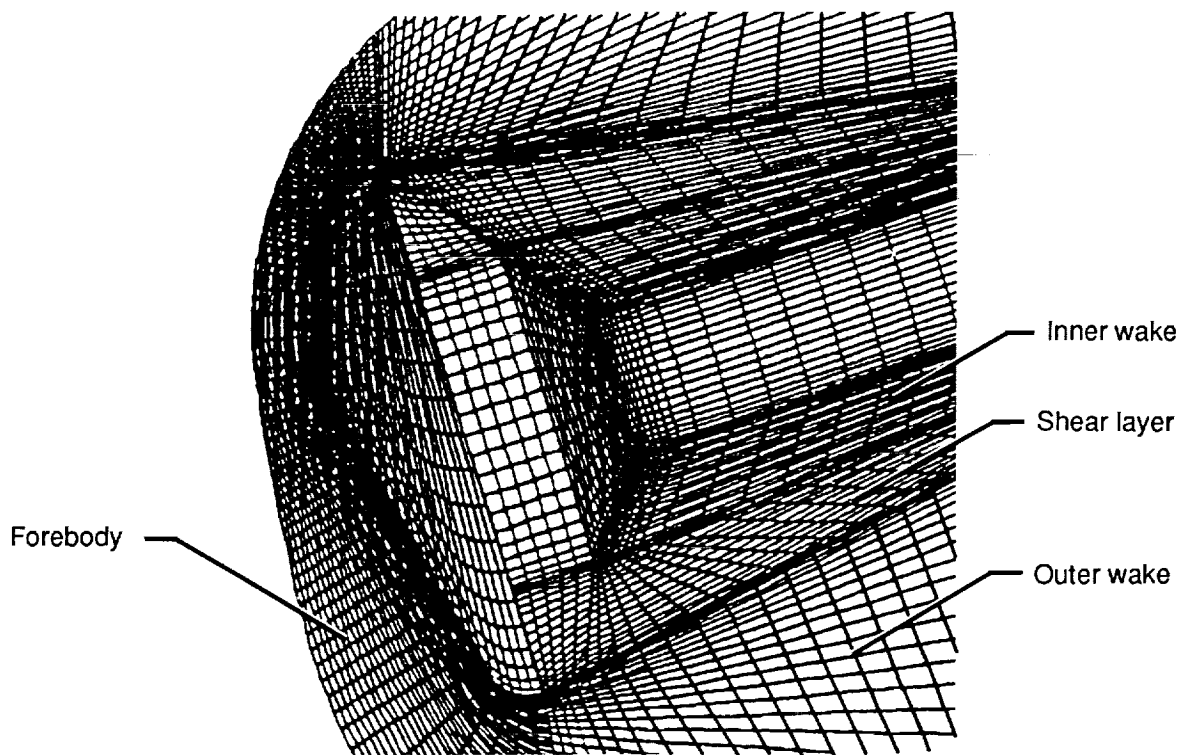
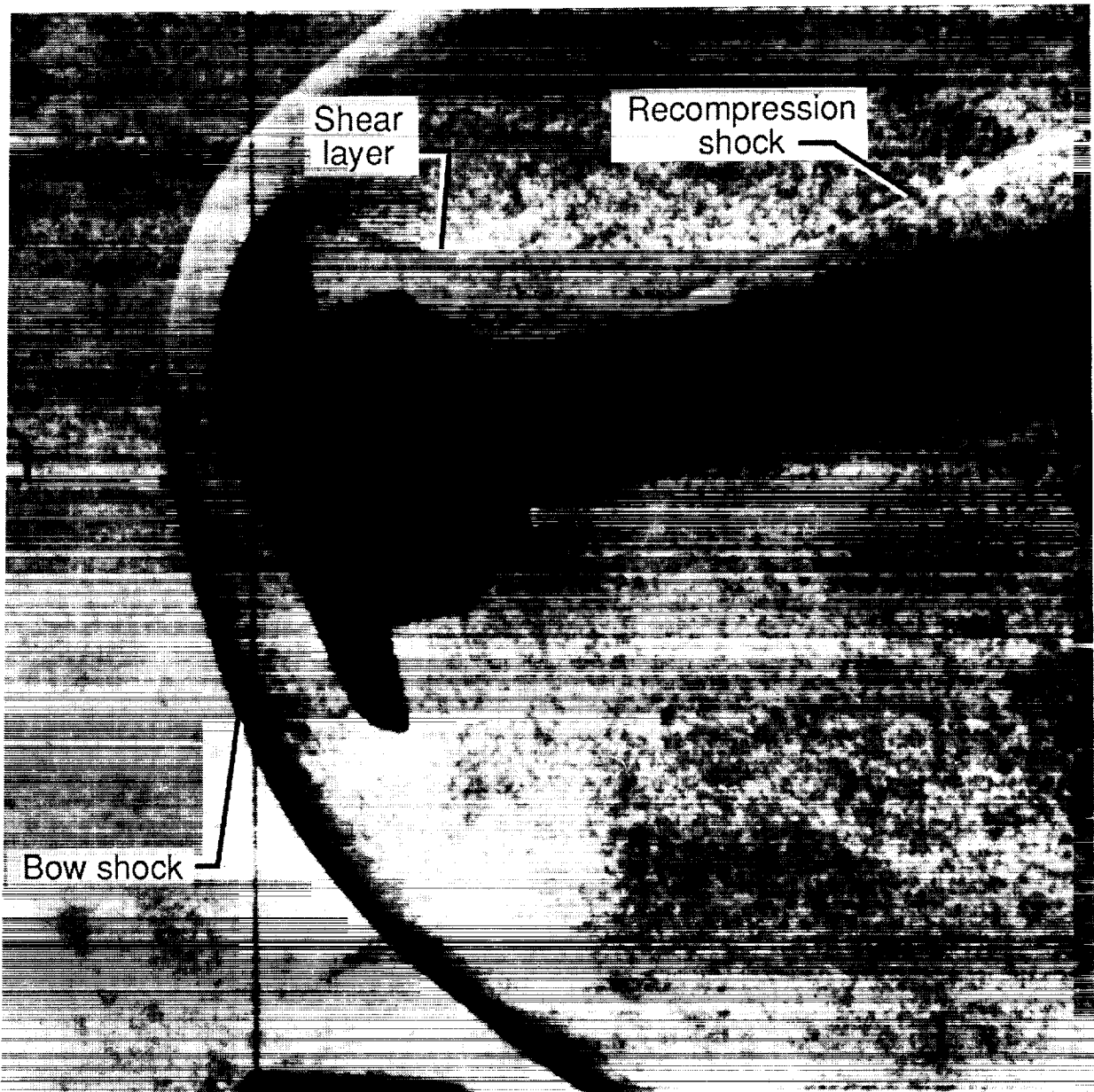


Figure 9. Multidomain grid defining the surface and plane of symmetry for AFE test case. The domains are approximately divided into forebody, outer wake, shear layer behind the shoulder, and inner wake core surrounding the sting (from ref. 14).

ORIGINAL PAGE  
BLACK AND WHITE PHOTOGRAPH

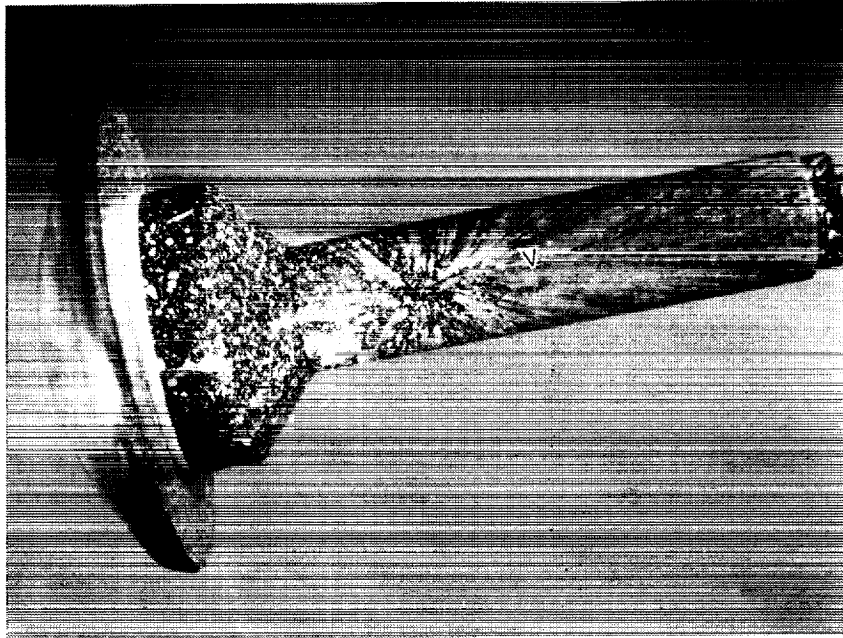
ORIGINAL PAGE  
BLACK AND WHITE PHOTOGRAPH



L-88-5353

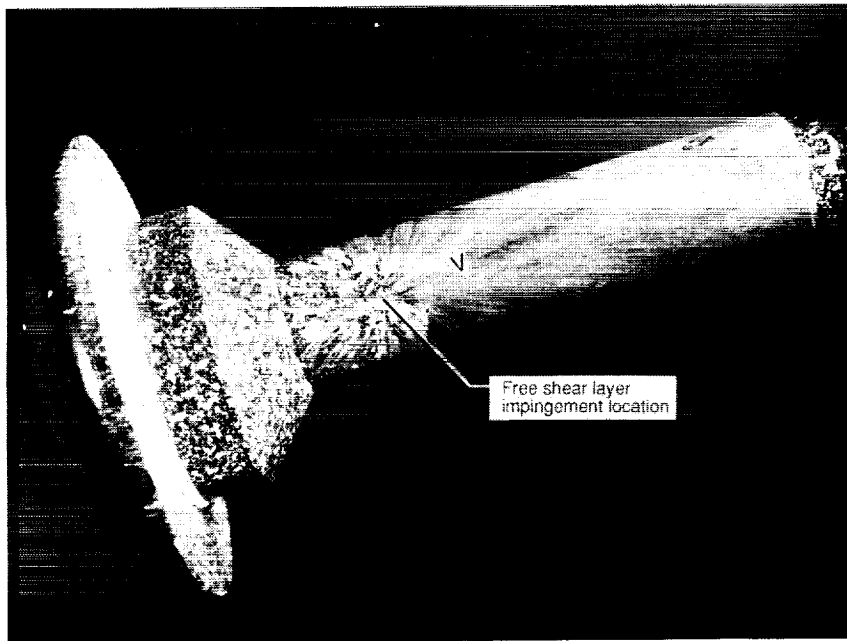
Figure 10. Schlieren photograph showing free shear layer and shocks in Mach 6 flow with AFE wake-heating model.  $Re_{2,D} = 103\,000$ .

REPRODUCED FROM THE  
AERONAUTICAL ENGINEERING  
RESEARCH ESTABLISHMENT  
REPORT



L-87-11,214

(a)  $Re_{2,D} = 6550$ ;  $\alpha = 5^\circ$  (run number 197).

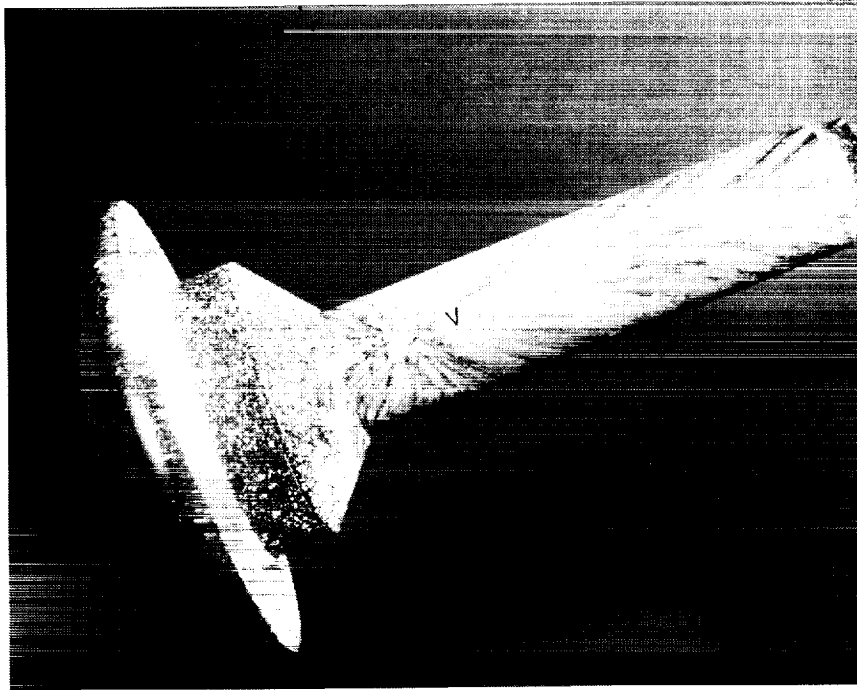


L-89-125

(b)  $Re_{2,D} = 6184$ ;  $\alpha = 0^\circ$  (run number 187).

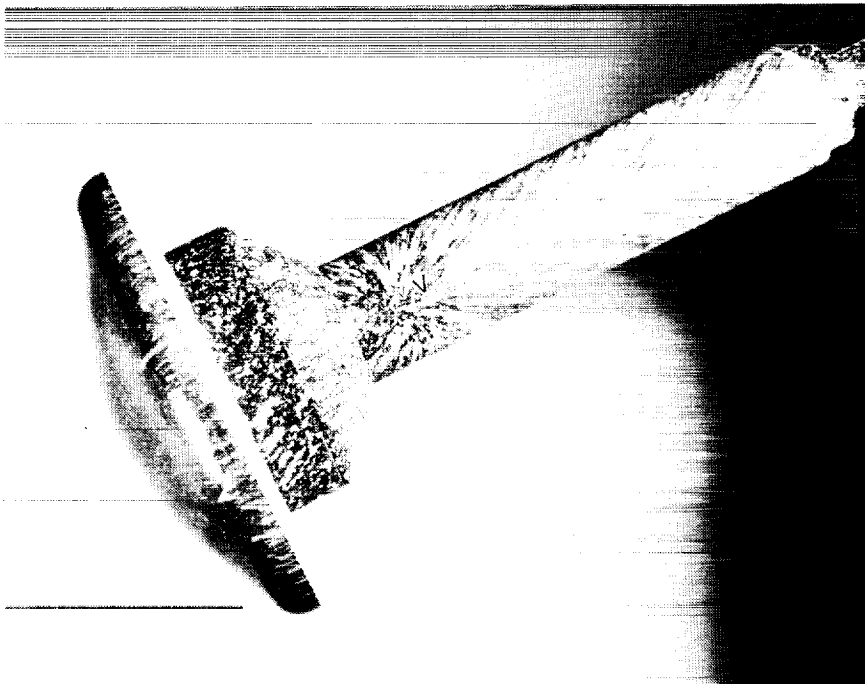
Figure 11. Photographs of oil flow on top of cylinder in wake of AFE forebody configuration. Symbol "v" indicates maximum heating location.  $Re_{2,D} \approx 6300$ .

ORIGINAL PAGE  
BLACK AND WHITE PHOTOGRAPH



(c)  $Re_{2,D} = 6034$ ;  $\alpha = -5^\circ$  (run number 189).

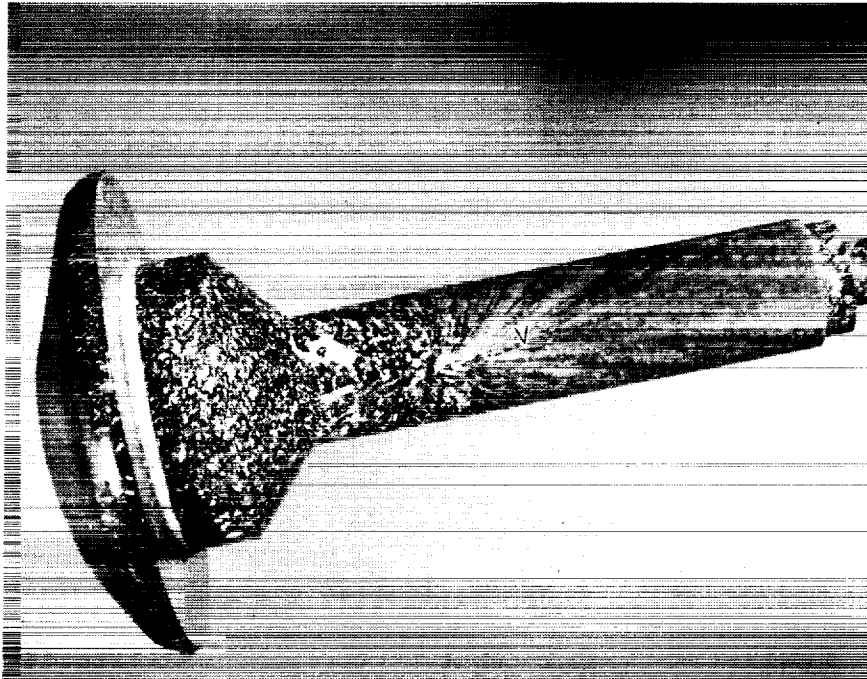
L-89-126



(d)  $Re_{2,D} = 6446$ ;  $\alpha = -10^\circ$  (run number 191).

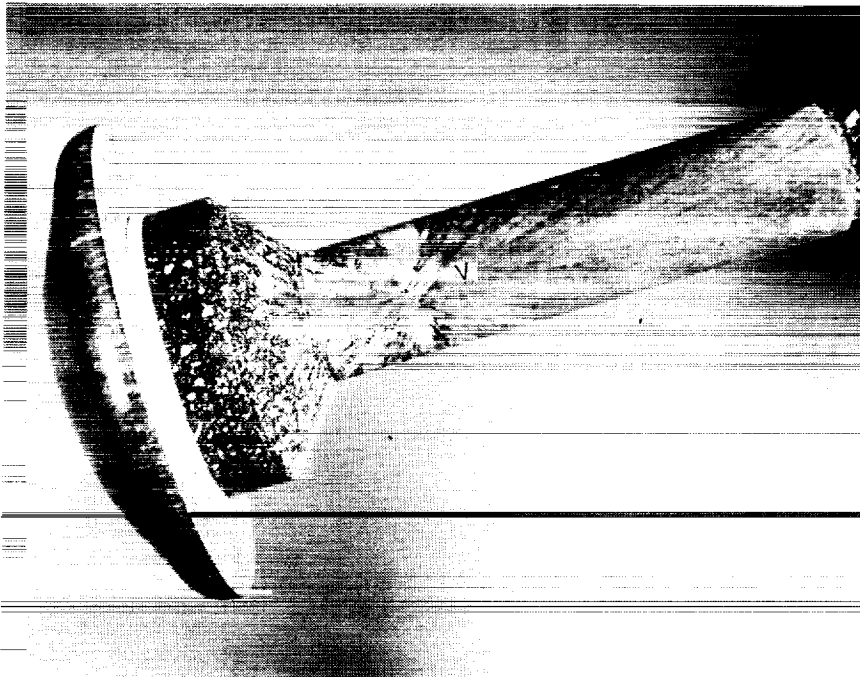
L-89-127

Figure 11. Concluded.



L-89-128

(a)  $Re_{2,D} = 13683$ ;  $\alpha = 5^\circ$  (run number 201).

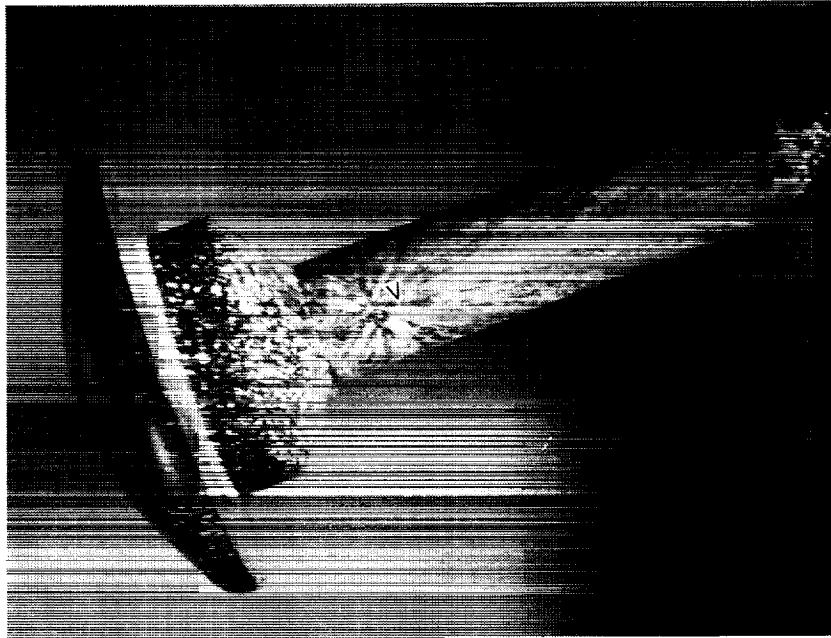


L-89-129

(b)  $Re_{2,D} = 13674$ ;  $\alpha = 0^\circ$  (run number 190).

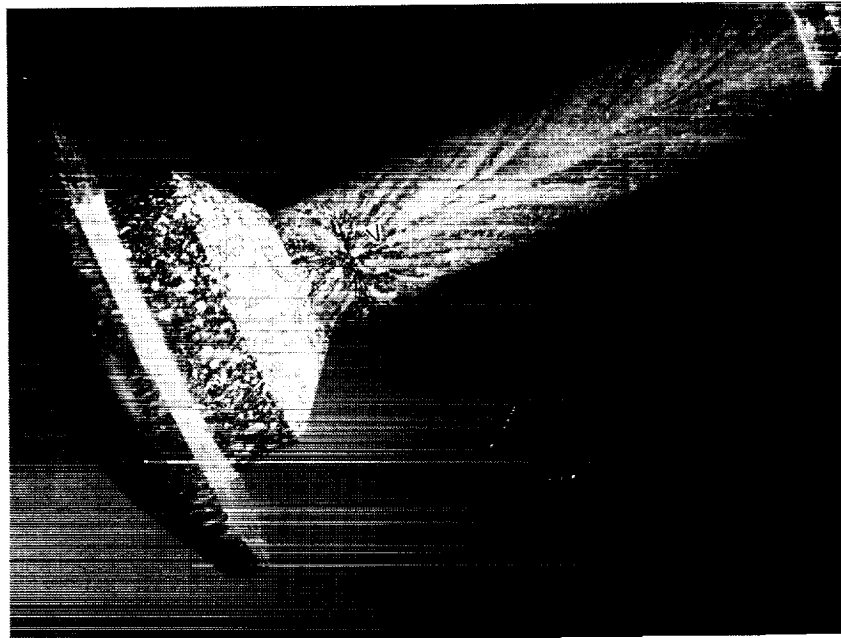
Figure 12. Photographs of oil flow on top of cylinder in wake of AFE forebody configuration. Symbol "v" indicates maximum heating location.  $Re_{2,D} \approx 13800$ .

ORIGINAL PAGE  
BLACK AND WHITE PHOTOGRAPH



L-87-11,199

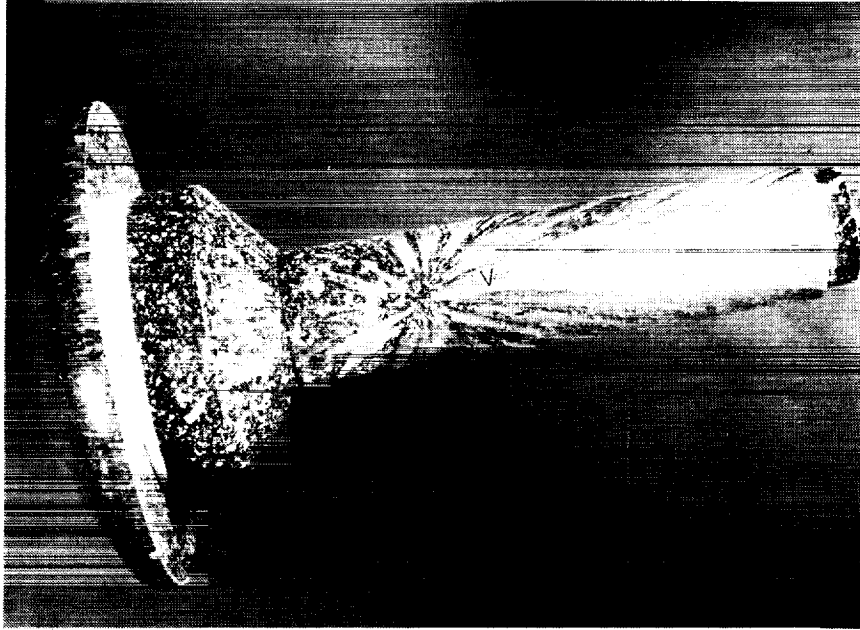
(c)  $Re_{2,D} = 14059$ ;  $\alpha = -5^\circ$  (run number 194).



L-87-11,187

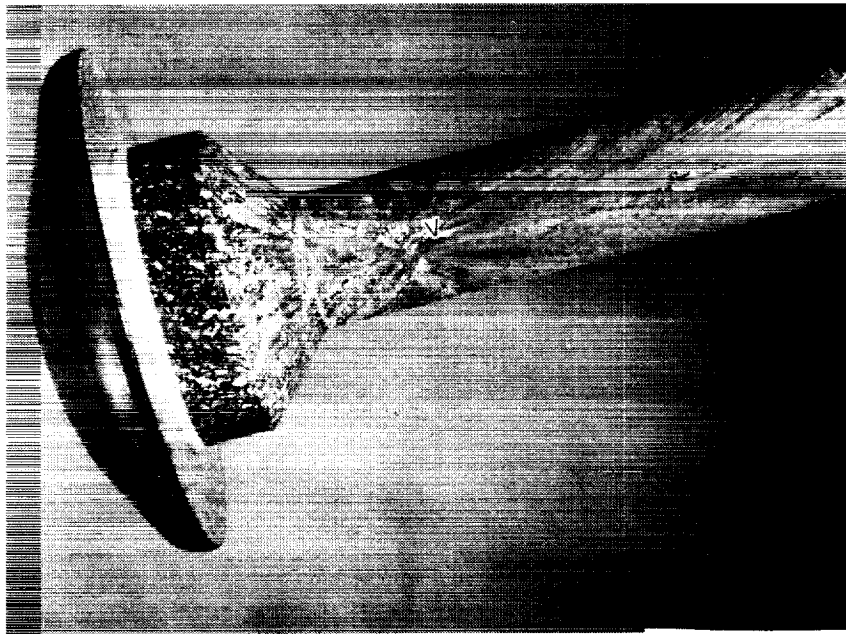
(d)  $Re_{2,D} = 14288$ ;  $\alpha = -10^\circ$  (run number 192).

Figure 12. Concluded.



L-89-130

(a)  $Re_{2,D} = 51\,196$ ;  $\alpha = 5^\circ$  (run number 203).

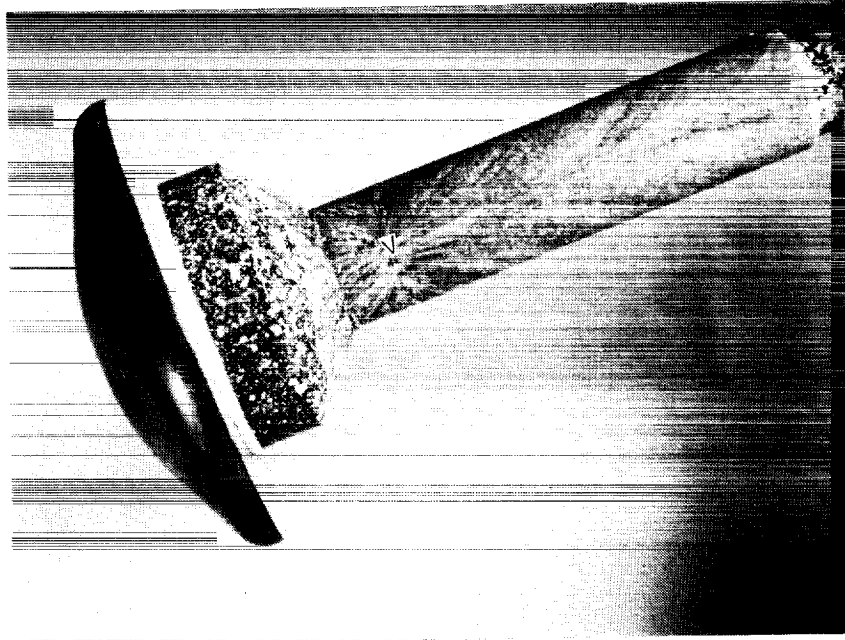


L-87-11,190

(b)  $Re_{2,D} = 50\,744$ ;  $\alpha = 0^\circ$  (run number 193).

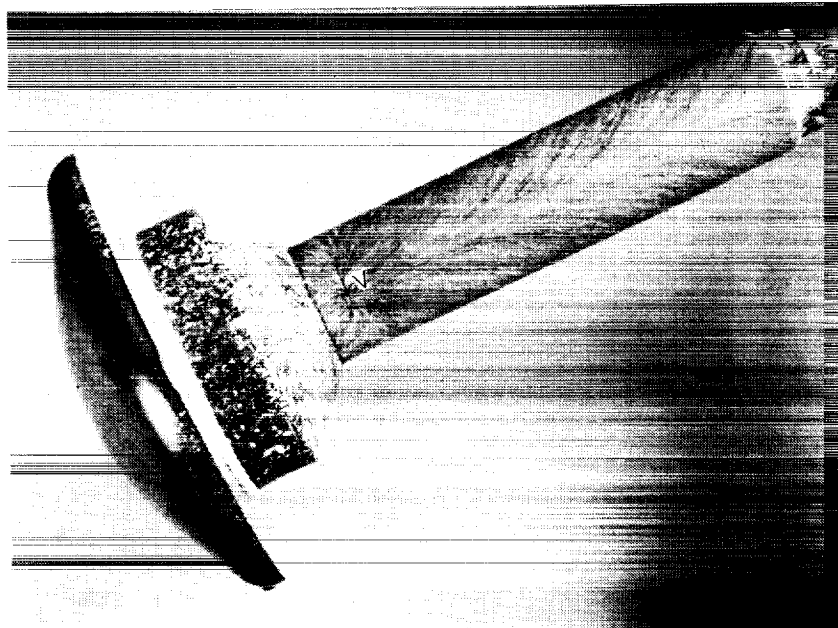
Figure 13. Photographs of oil flow on top of cylinder in wake of AFE forebody configuration. Symbol "v" indicates maximum heating location.  $Re_{2,D} \approx 50\,200$ .

ORIGINAL PAGE  
BLACK AND WHITE PHOTOGRAPH



L-87-11,195

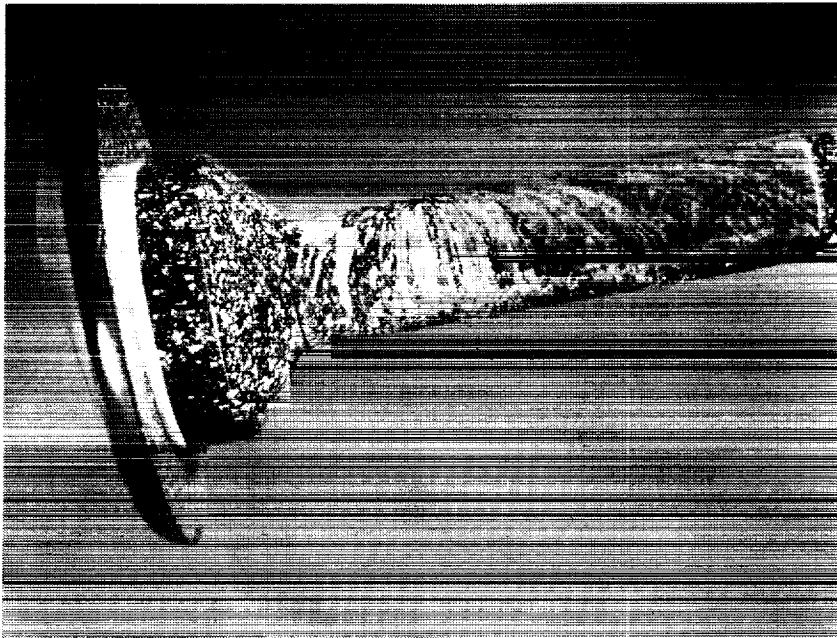
(c)  $Re_{2,D} = 49\,728$ ;  $\alpha = -5^\circ$  (run number 195).



L-87-11,203

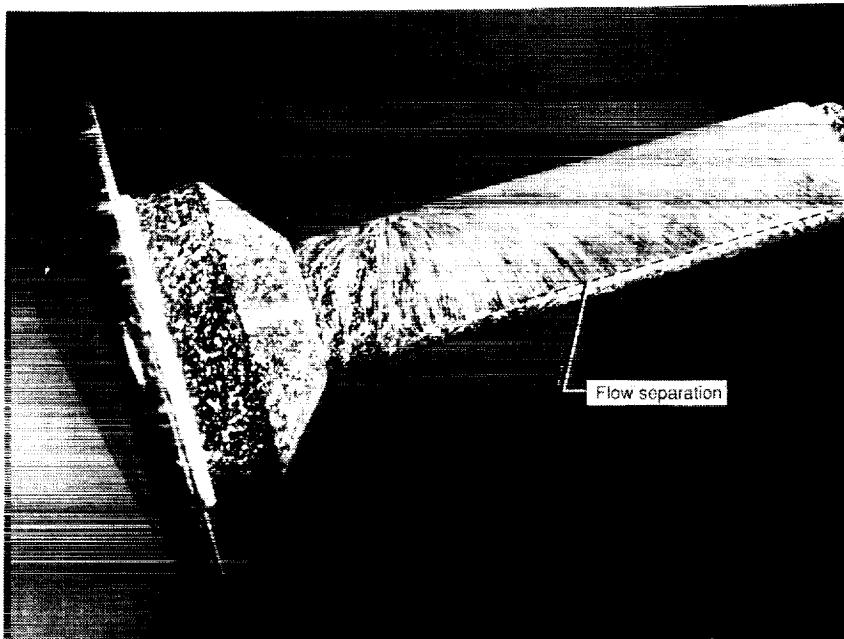
(d)  $Re_{2,D} = 50\,400$ ;  $\alpha = -10^\circ$  (run number 196).

Figure 13. Concluded.



L-87-11,213

(a)  $Re_{2,D} = 6550$ ;  $\alpha = 5^\circ$  (run number 197).

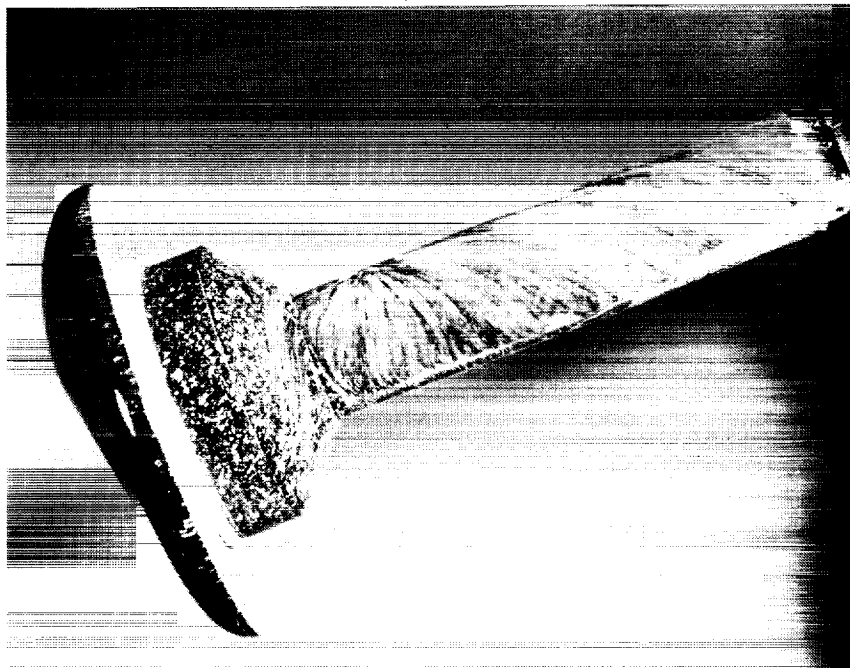


L-89-131

(b)  $Re_{2,D} = 6184$ ;  $\alpha = 0^\circ$  (run number 187).

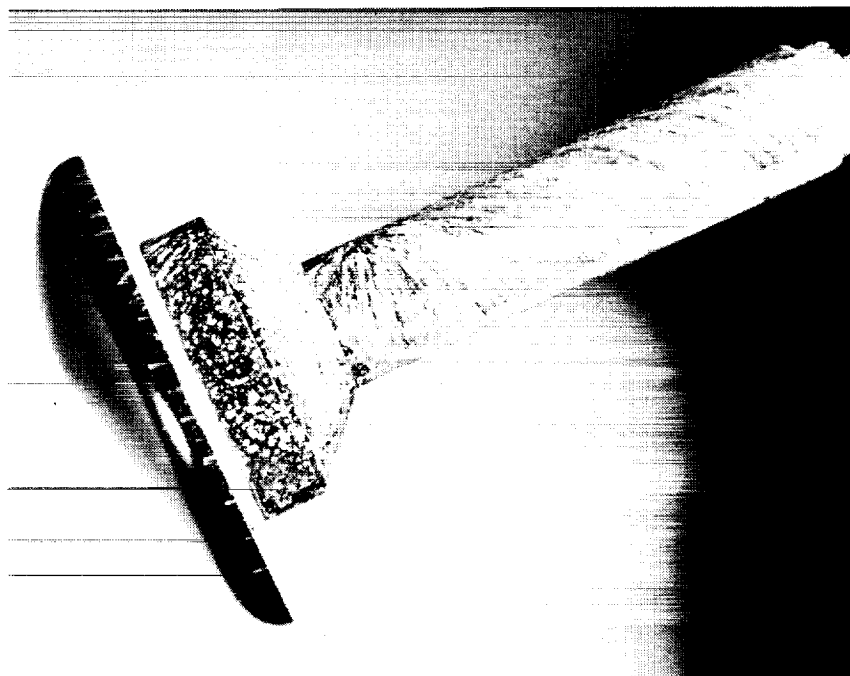
Figure 14. Photographs of oil flow on side of cylinder in wake of AFE forebody configuration.  $Re_{2,D} \approx 6300$ .

ORIGINAL PAGE  
BLACK AND WHITE PHOTOGRAPH



L-89-132

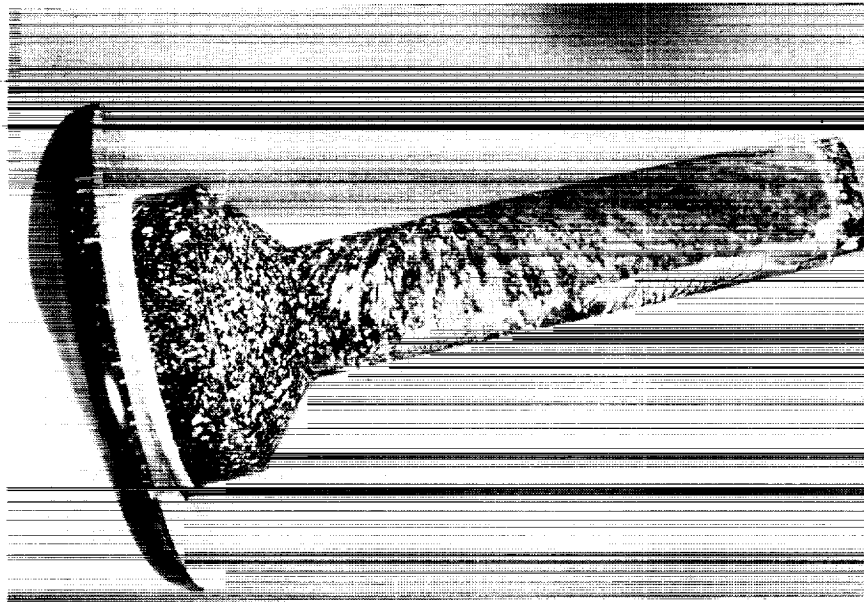
(c)  $Re_{2,D} = 6034$ ;  $\alpha = -5^\circ$  (run number 189).



L-89-133

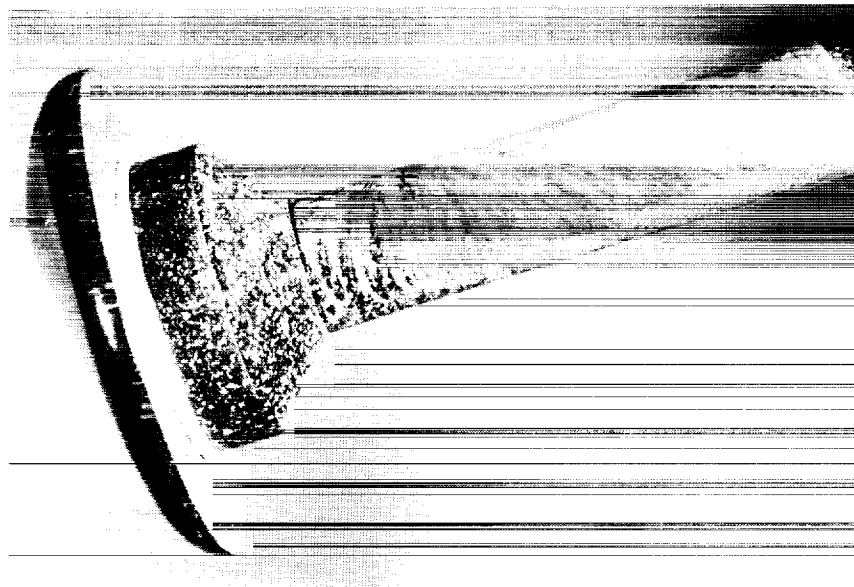
(d)  $Re_{2,D} = 6446$ ;  $\alpha = -10^\circ$  (run number 191).

Figure 14. Concluded.



L-89-134

(a)  $Re_{2,D} = 13683$ ;  $\alpha = 5^\circ$  (run number 201).

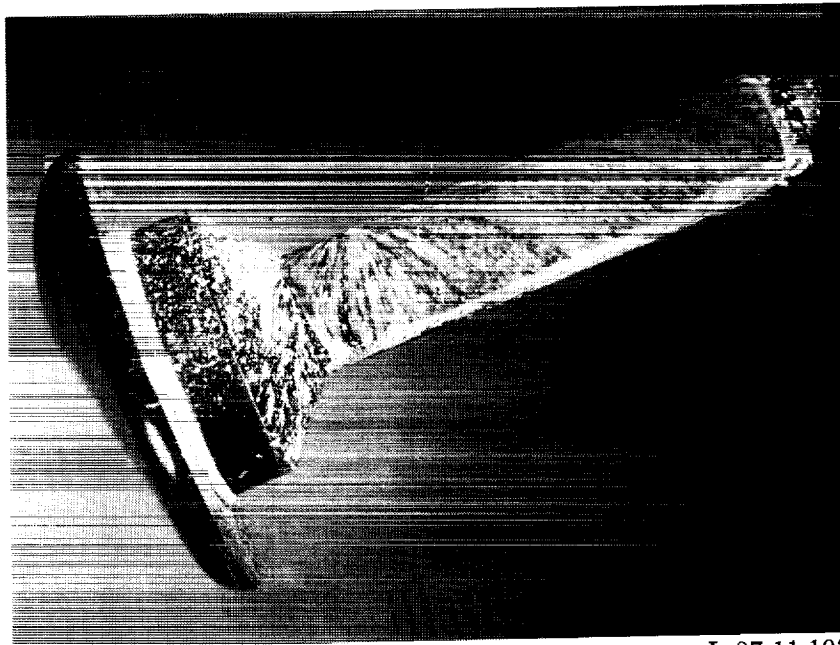


L-89-135

(b)  $Re_{2,D} = 13674$ ;  $\alpha = 0^\circ$  (run number 190).

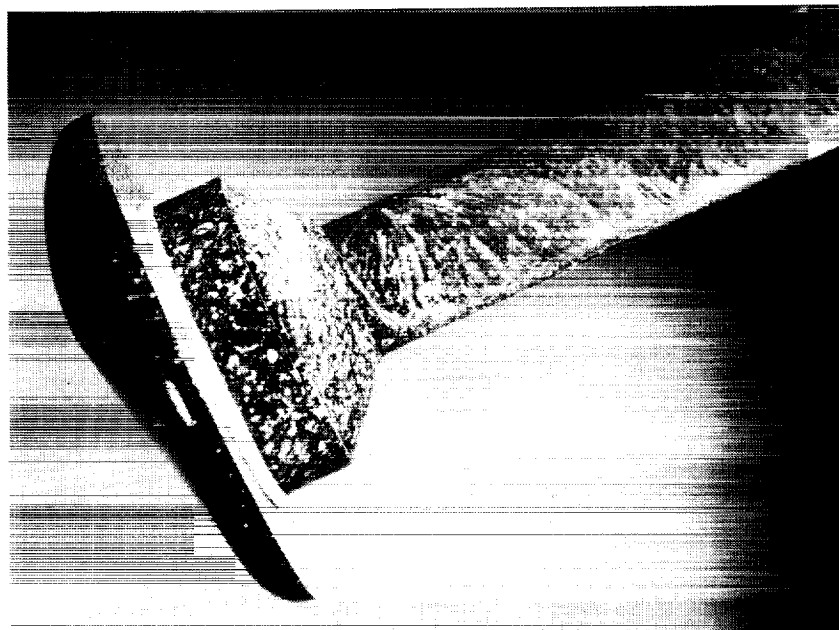
Figure 15. Photographs of oil flow on side of cylinder in wake of AFE forebody configuration.  $Re_{2,D} \approx 13800$ .

ORIGINAL PAGE  
BLACK AND WHITE PHOTOGRAPH



L-87-11,193

(c)  $Re_{2,D} = 14059$ ;  $\alpha = -5^\circ$  (run number 194).



L-87-11,184

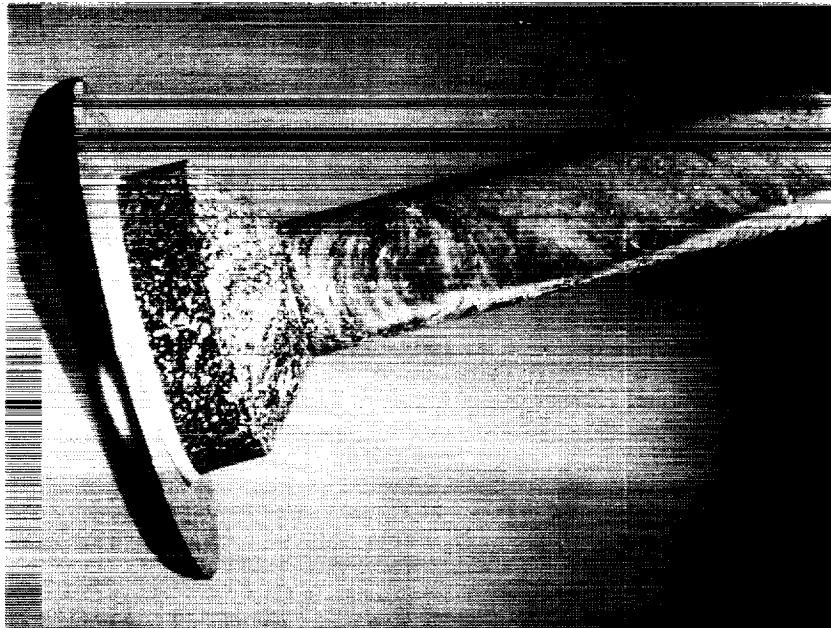
(d)  $Re_{2,D} = 14228$ ;  $\alpha = -10^\circ$  (run number 192).

Figure 15. Concluded.



L-89-136

(a)  $Re_{2,D} = 51\,196$ ;  $\alpha = 5^\circ$  (run number 203).

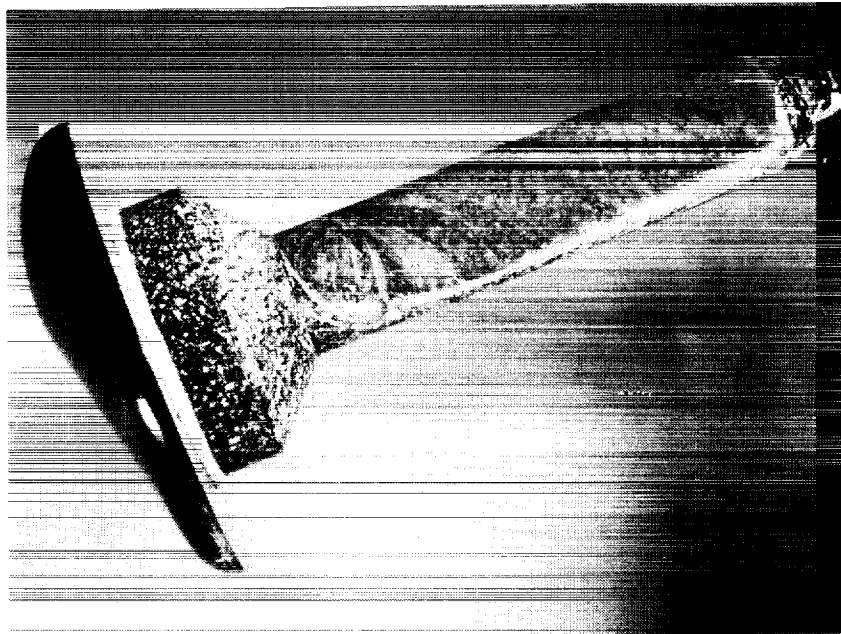


L-87-11,185

(b)  $Re_{2,D} = 50\,744$ ;  $\alpha = 0^\circ$  (run number 193).

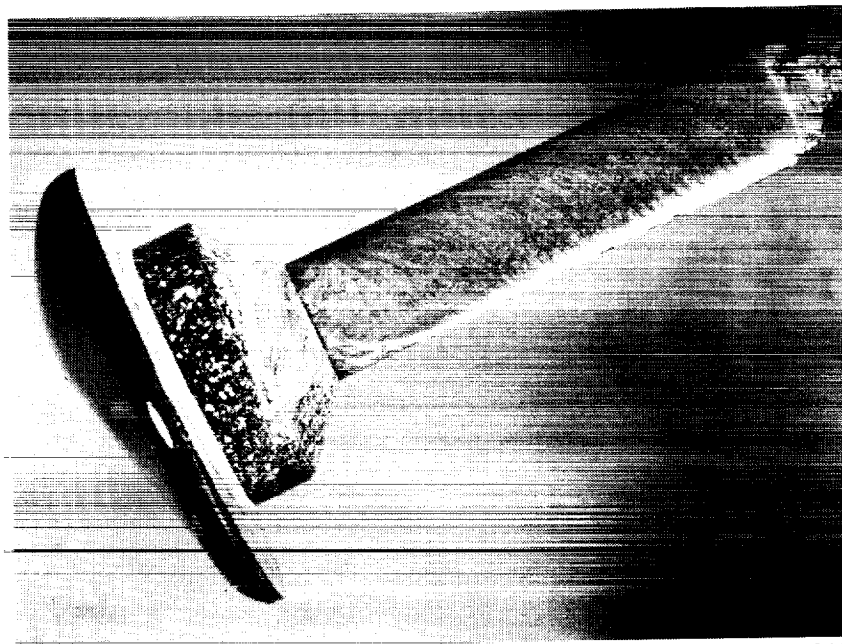
Figure 16. Photographs of oil flow on side of cylinder in wake of AFE forebody configuration.  $Re_{2,D} \approx 50\,200$ .

ORIGINAL PAGE  
BLACK AND WHITE PHOTOGRAPH



L-87-11,192

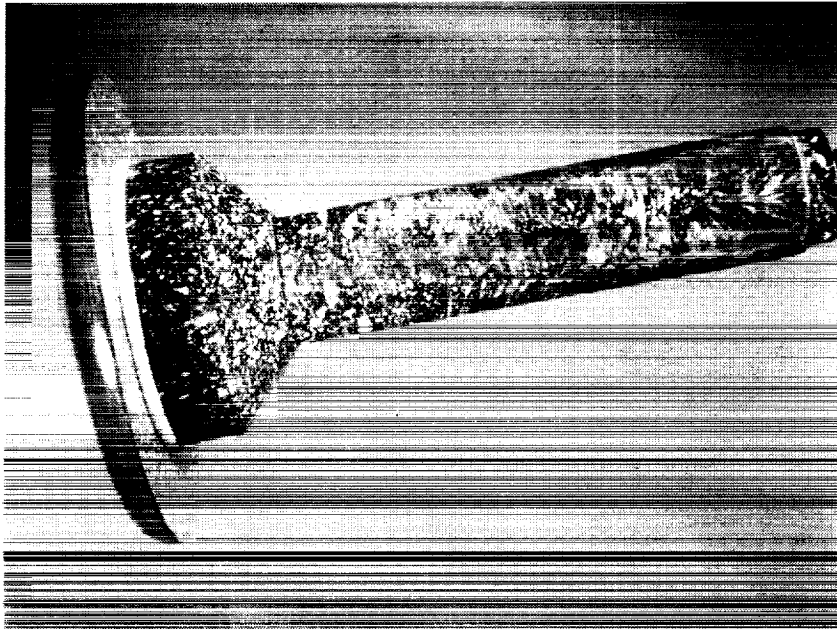
(c)  $Re_{2,D} = 49\,728$ ;  $\alpha = -5^\circ$  (run number 195).



L-87-11,212

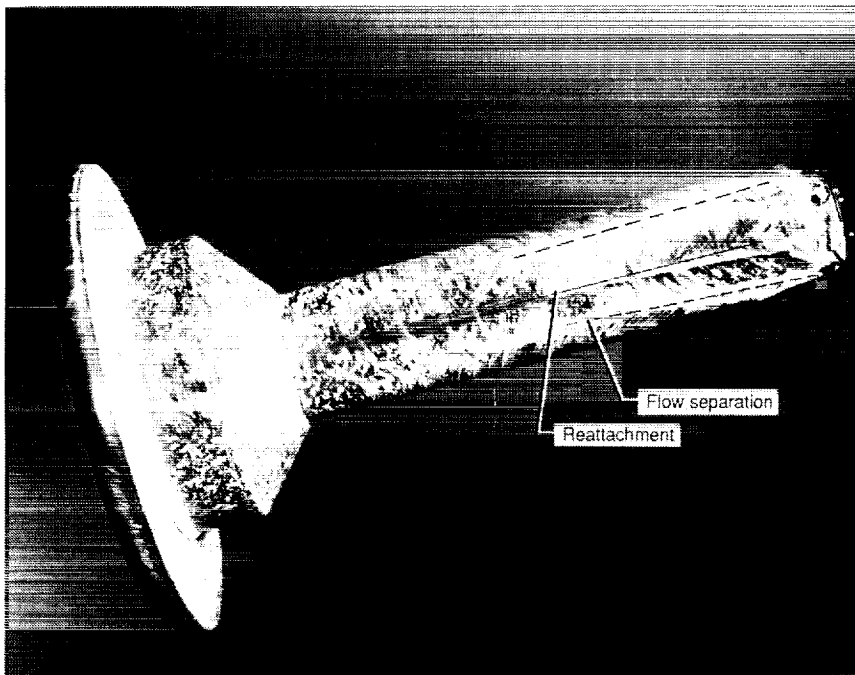
(d)  $Re_{2,D} = 50\,400$ ;  $\alpha = -10^\circ$  (run number 196).

Figure 16. Concluded.



L-87-11,208

(a)  $Re_{2,D} = 6550$ ;  $\alpha = 5^\circ$  (run number 197).

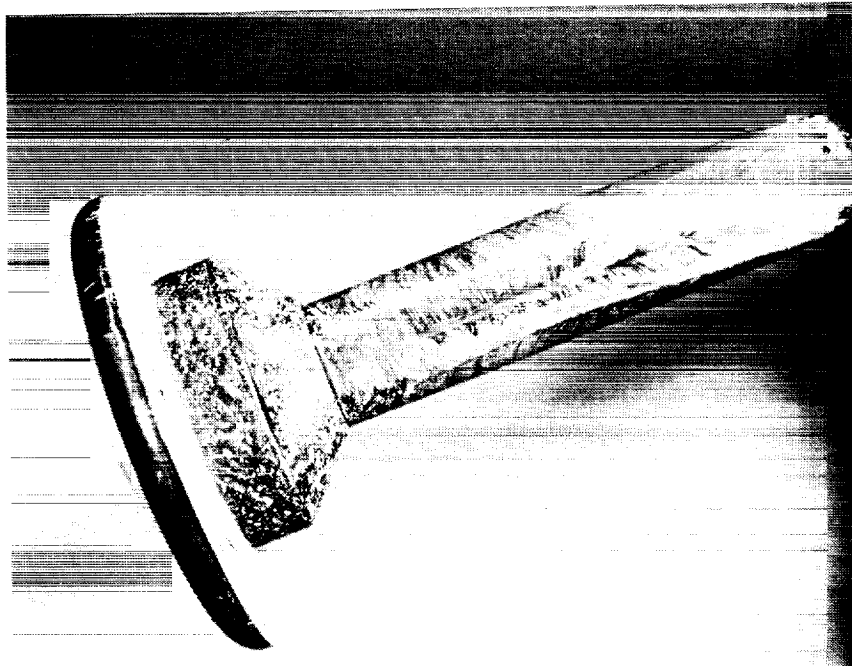


L-89-137

(b)  $Re_{2,D} = 6184$ ;  $\alpha = 0^\circ$  (run number 187).

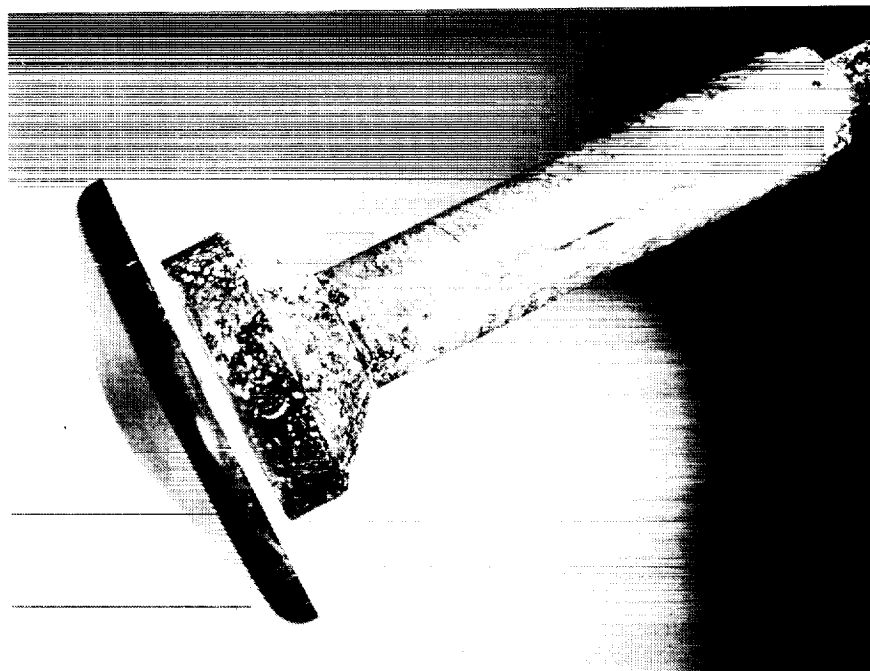
Figure 17. Photographs of oil flow on bottom of cylinder in wake of AFE forebody configuration.  $Re_{2,D} \approx 6300$ .

ORIGINAL PAGE  
BLACK AND WHITE PHOTOGRAPH



L-89-138

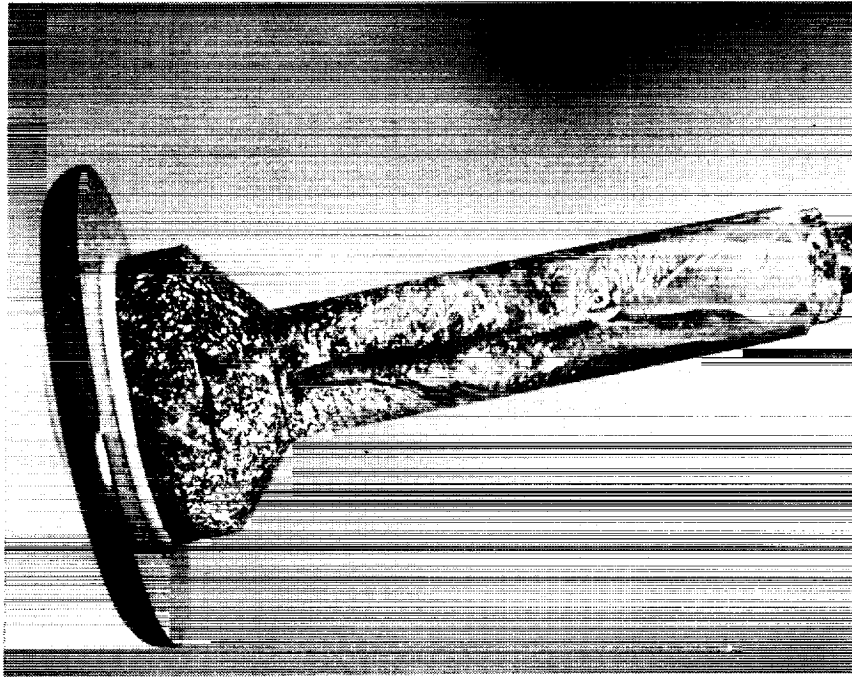
(c)  $Re_{2,D} = 6034$ ;  $\alpha = -5^\circ$  (run number 189).



L-89-139

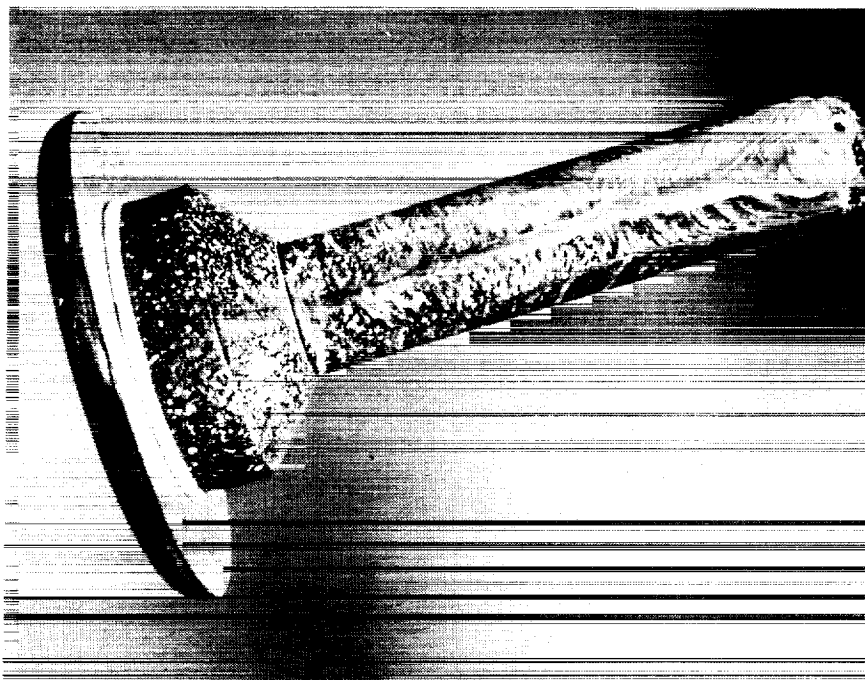
(d)  $Re_{2,D} = 6446$ ;  $\alpha = -10^\circ$  (run number 191).

Figure 17. Concluded.



L-89-140

(a)  $Re_{2,D} = 13683$ ;  $\alpha = 5^\circ$  (run number 201).

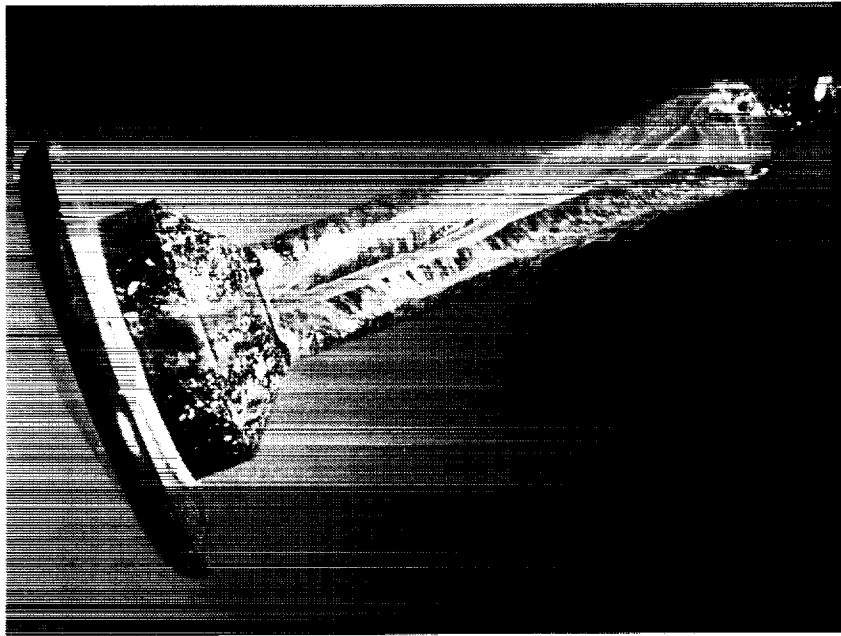


L-89-141

(b)  $Re_{2,D} = 13674$ ;  $\alpha = 0^\circ$  (run number 190).

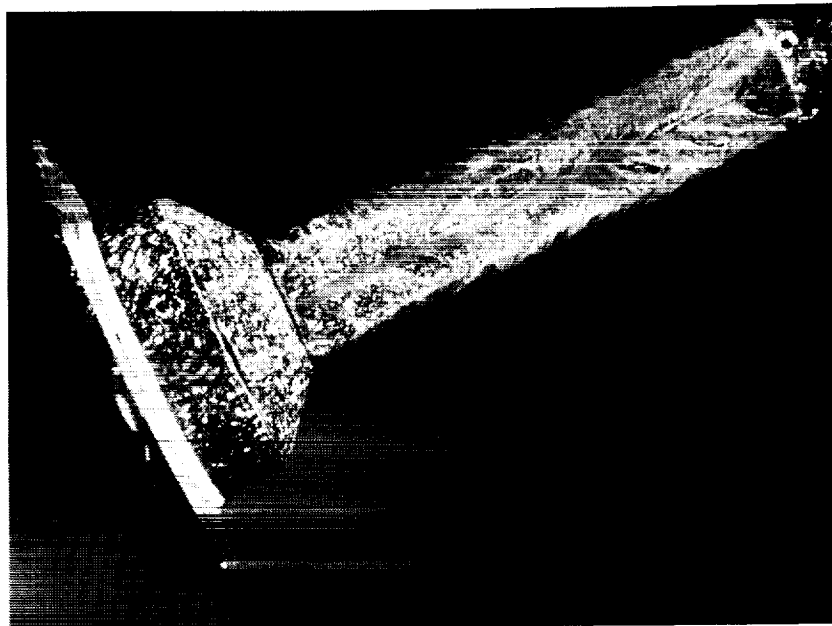
Figure 18. Photographs of oil flow on bottom of cylinder in wake of AFE forebody configuration.  
 $Re_{2,D} \approx 13800$ .

ORIGINAL PAGE  
BLACK AND WHITE PHOTOGRAPH



L-87-11,201

(c)  $Re_{2,D} = 14\,059$ ;  $\alpha = -5^\circ$  (run number 194).

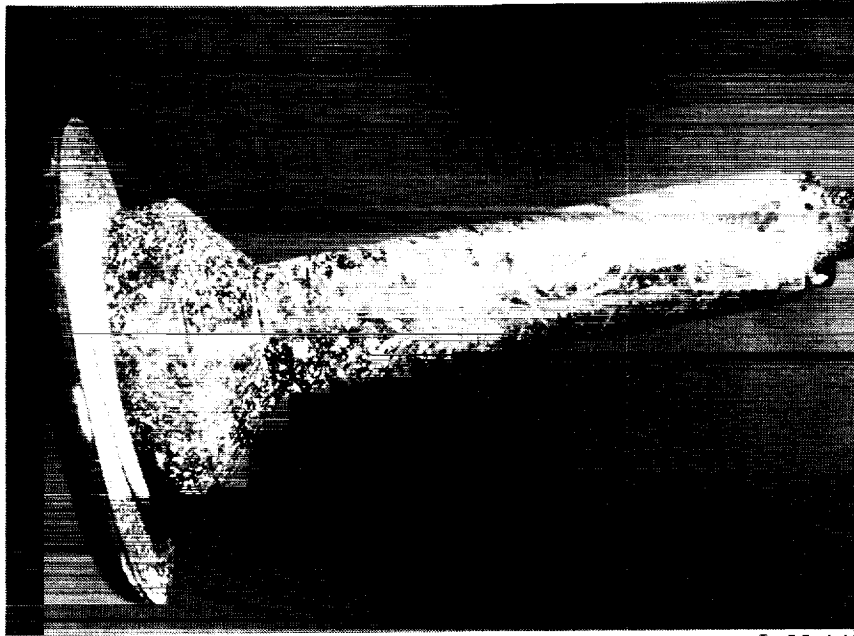


L-87-11,186

(d)  $Re_{2,D} = 14\,228$ ;  $\alpha = -10^\circ$  (run number 192).

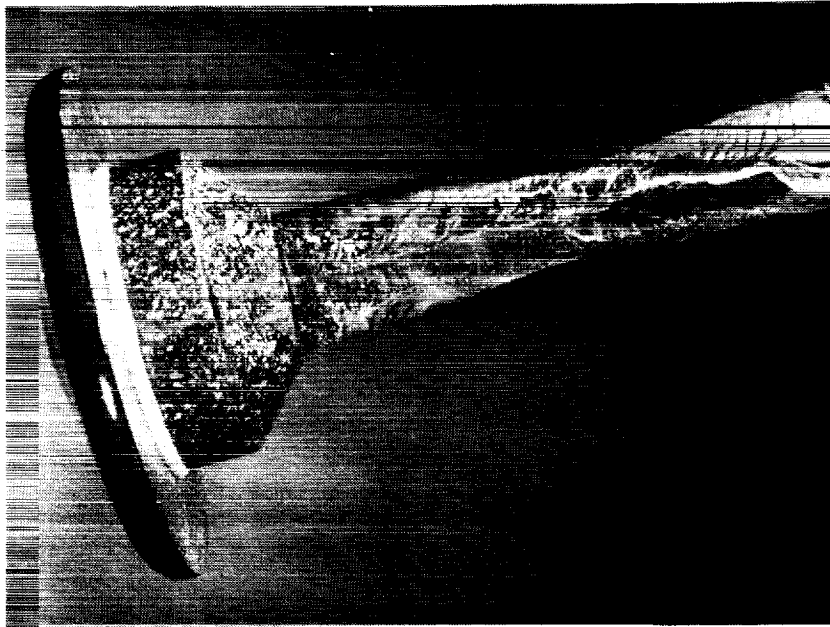
Figure 18. Concluded.

50  
BLACK AND WHITE PHOTOGRAPH



L-89-142

(a)  $Re_{2,D} = 51\,196$ ;  $\alpha = 5^\circ$  (run number 203).



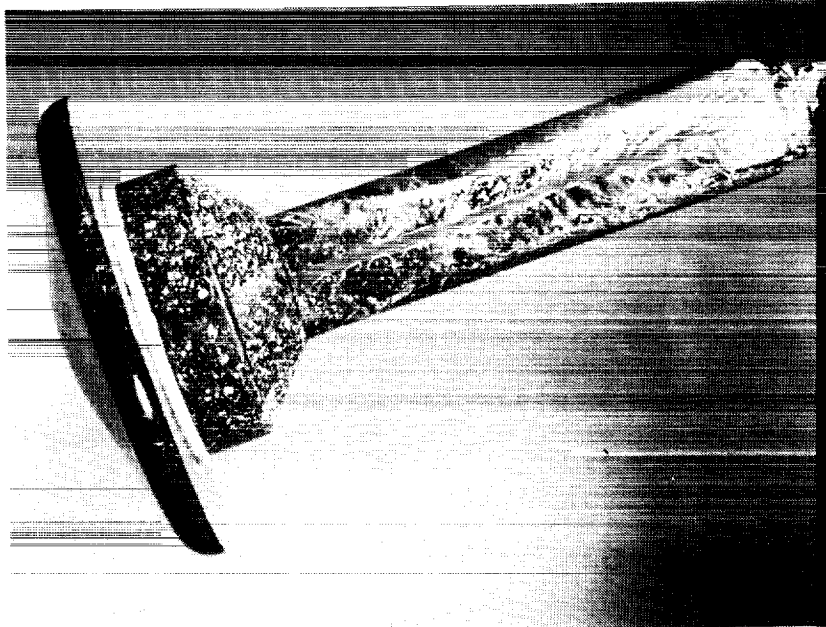
L-87-11,188

(b)  $Re_{2,D} = 50\,744$ ;  $\alpha = 0^\circ$  (run number 193).

Figure 19. Photographs of oil flow on bottom of cylinder in wake of AFE forebody configuration.  
 $Re_{2,D} \approx 50\,200$ .

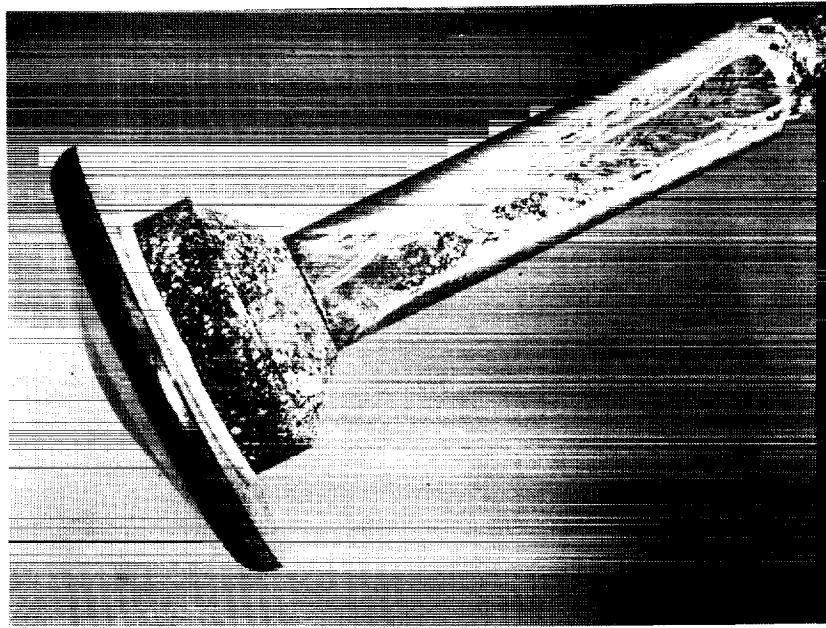
ORIGINAL PAGE  
BLACK AND WHITE PHOTOGRAPH

ORIGINAL PAGE  
BLACK AND WHITE PHOTOGRAPH



L-87-11,196

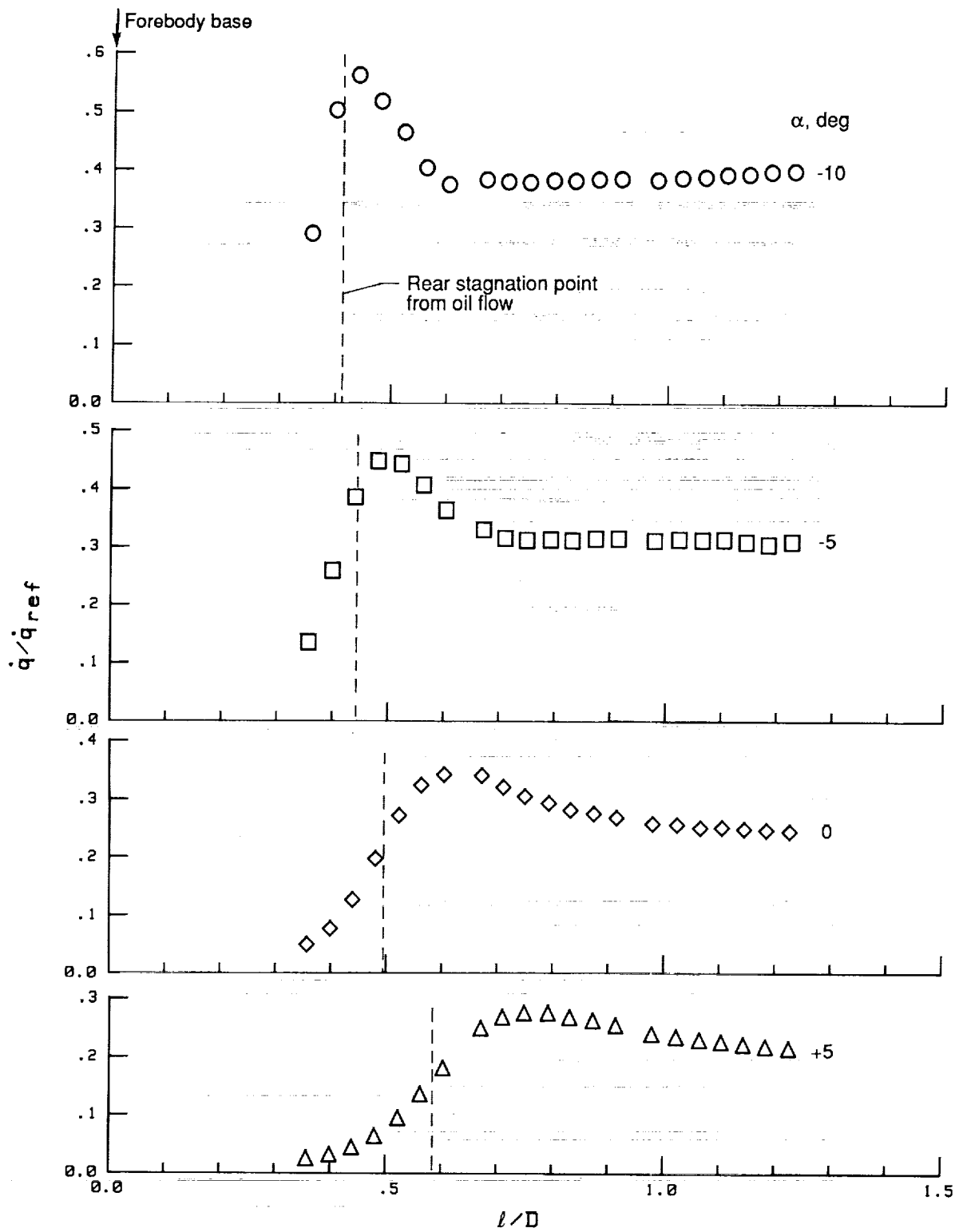
(c)  $Re_{2,D} = 49\,728$ ;  $\alpha = -5^\circ$  (run number 195).



L-87-11,202

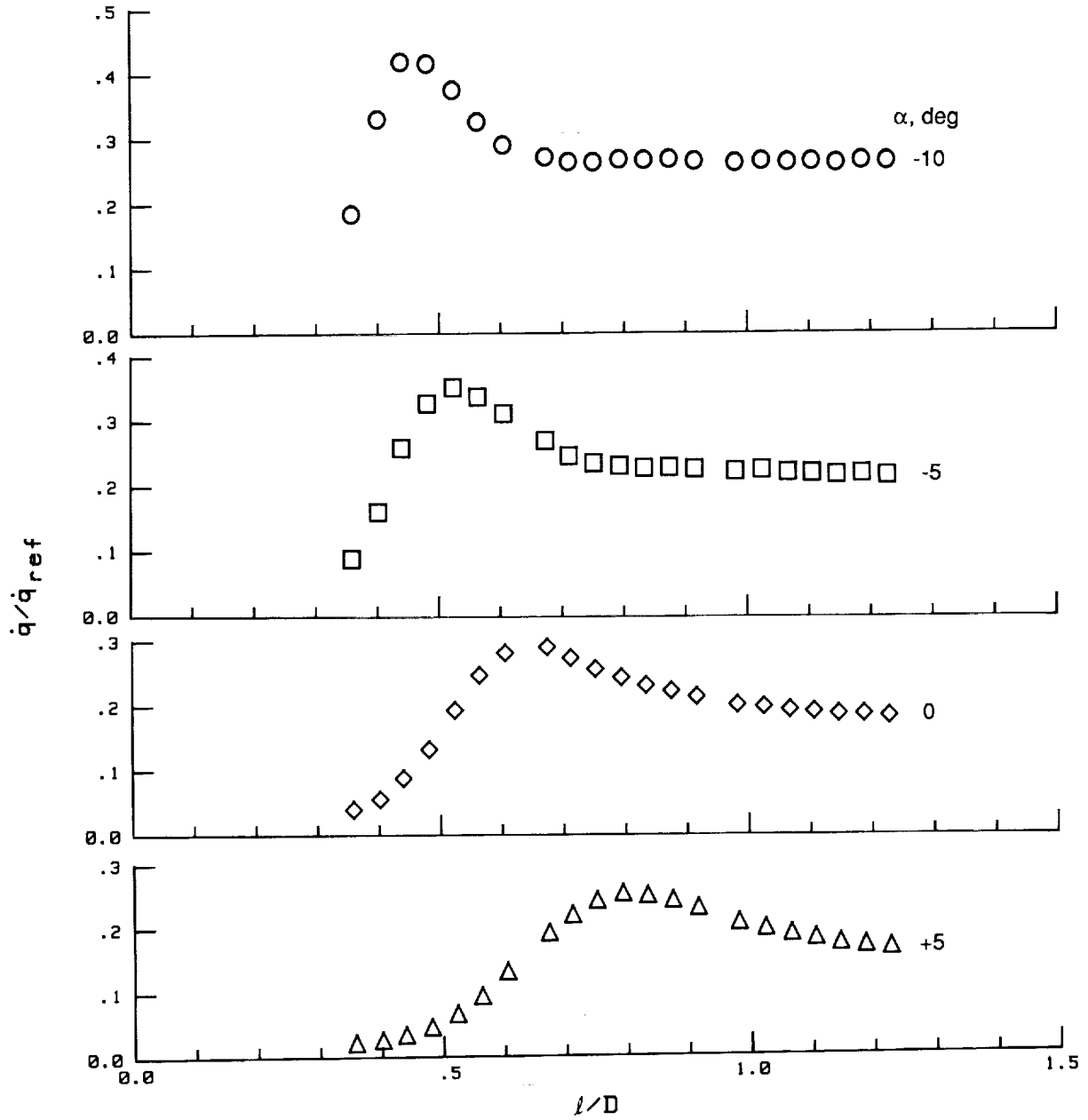
(d)  $Re_{2,D} = 50\,400$ ;  $\alpha = -10^\circ$  (run number 196).

Figure 19. Concluded.



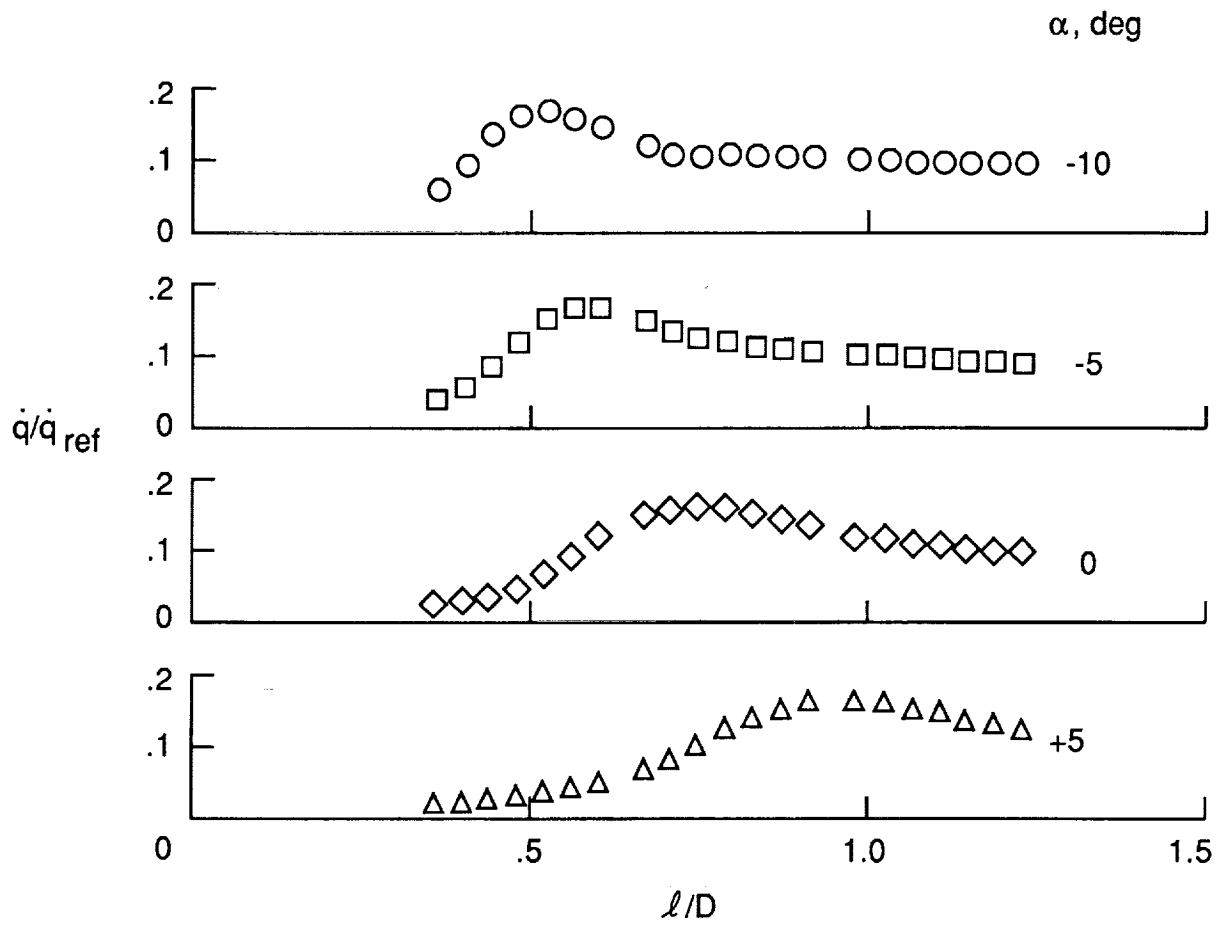
(a)  $\theta = 0^\circ$ .

Figure 20. Effect of angle of attack  $\alpha$  on heating distribution on a cylinder in wake of AFE configuration for nominal Mach 10 and  $Re_{2,D} = 13670$ .

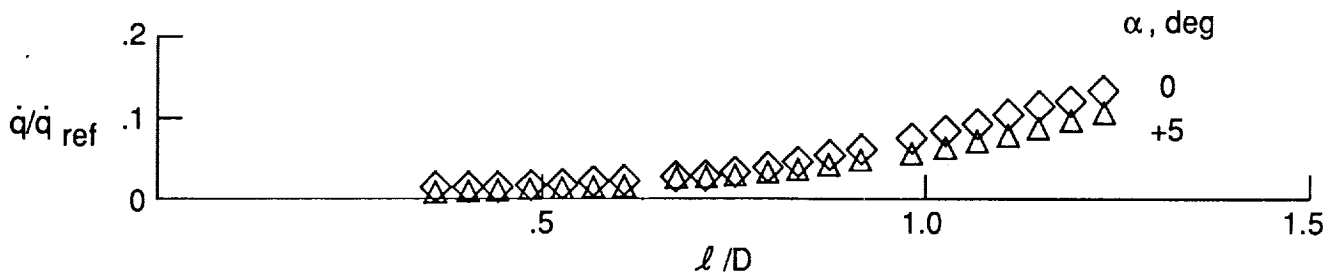


(b)  $\theta = 45^\circ$ .

Figure 20. Continued.



(c)  $\theta = 90^\circ$ .



(d)  $\theta = 180^\circ$ .

Figure 20. Concluded.

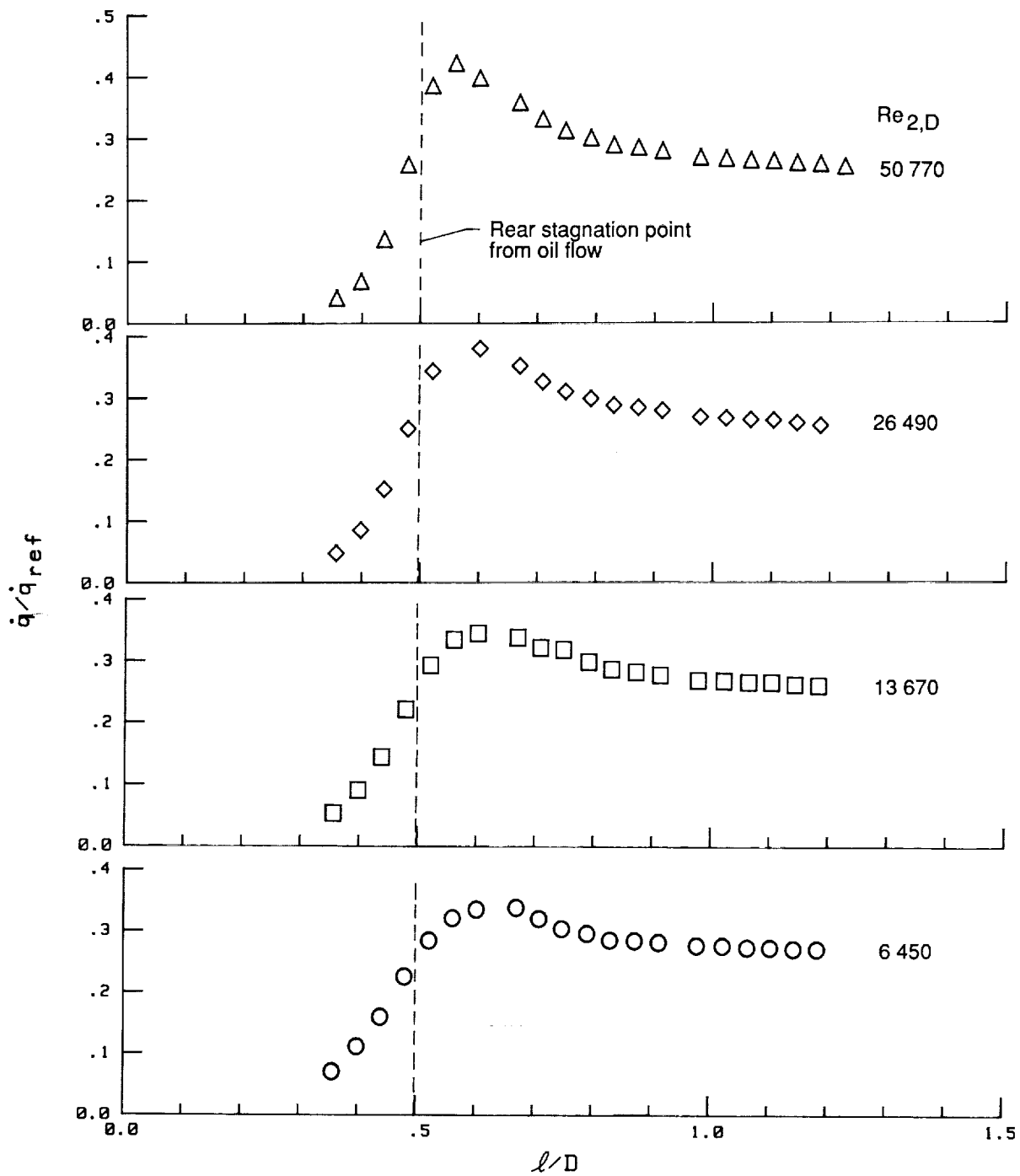


Figure 21. Effect of Reynolds number on measured heat-transfer distributions.  $\theta = 0^\circ$ ,  $\alpha = 0^\circ$ .

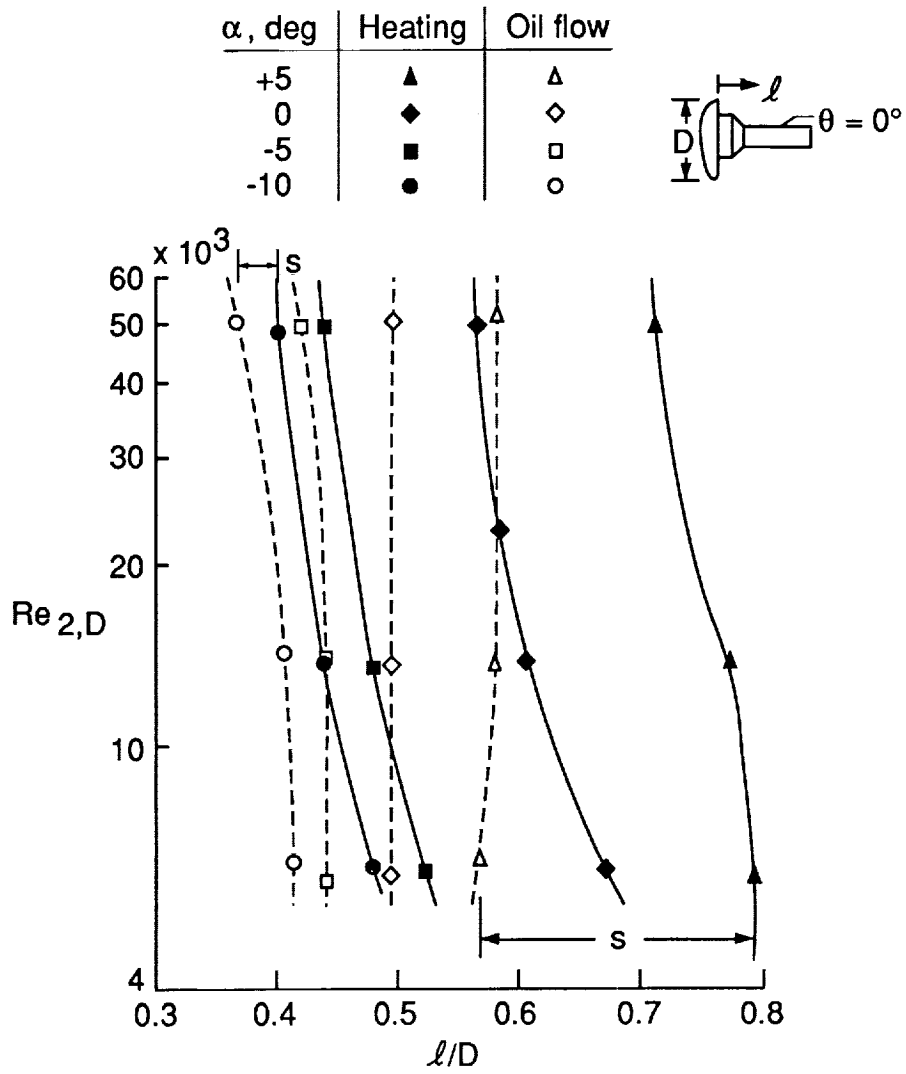


Figure 22. Free-shear-layer impingement locations at  $\theta = 0^\circ$  as determined by oil flows and heating measurements.

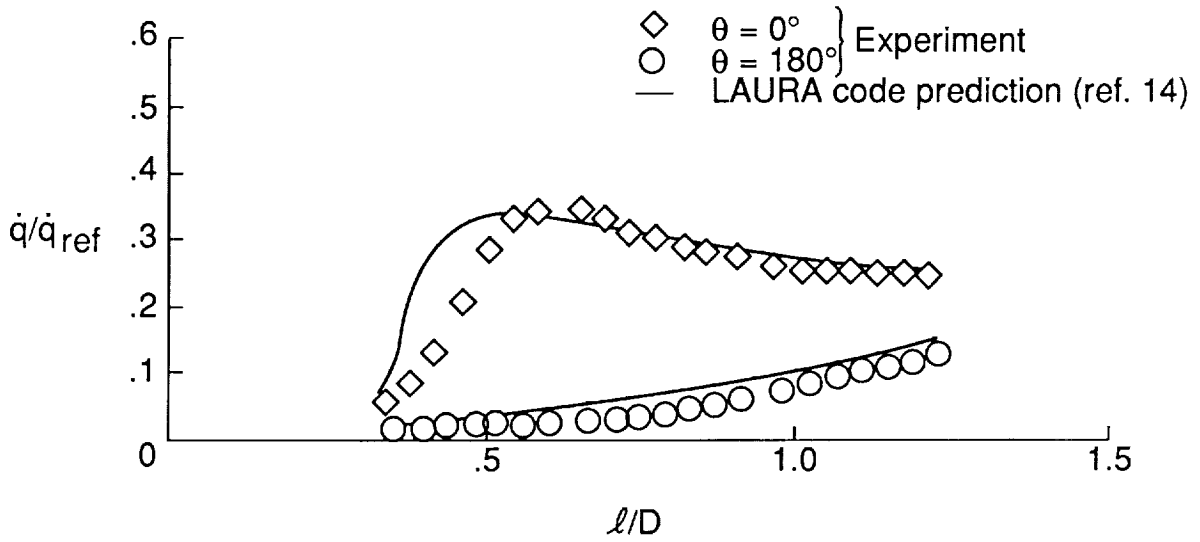


Figure 23. Comparison of predicted heating-rate distribution with measurements.  $Re_{2,D} = 13\,800$  and  $\alpha = 0^\circ$ .

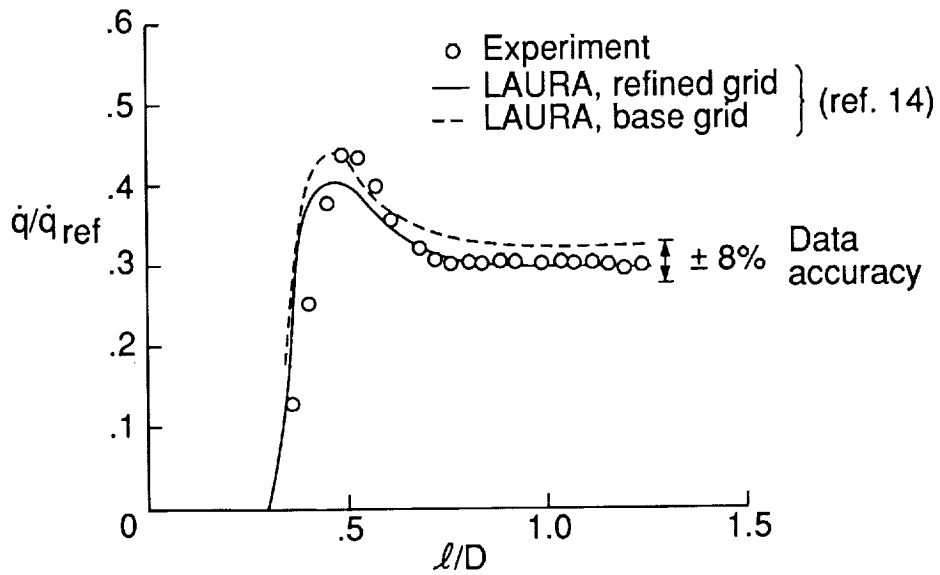
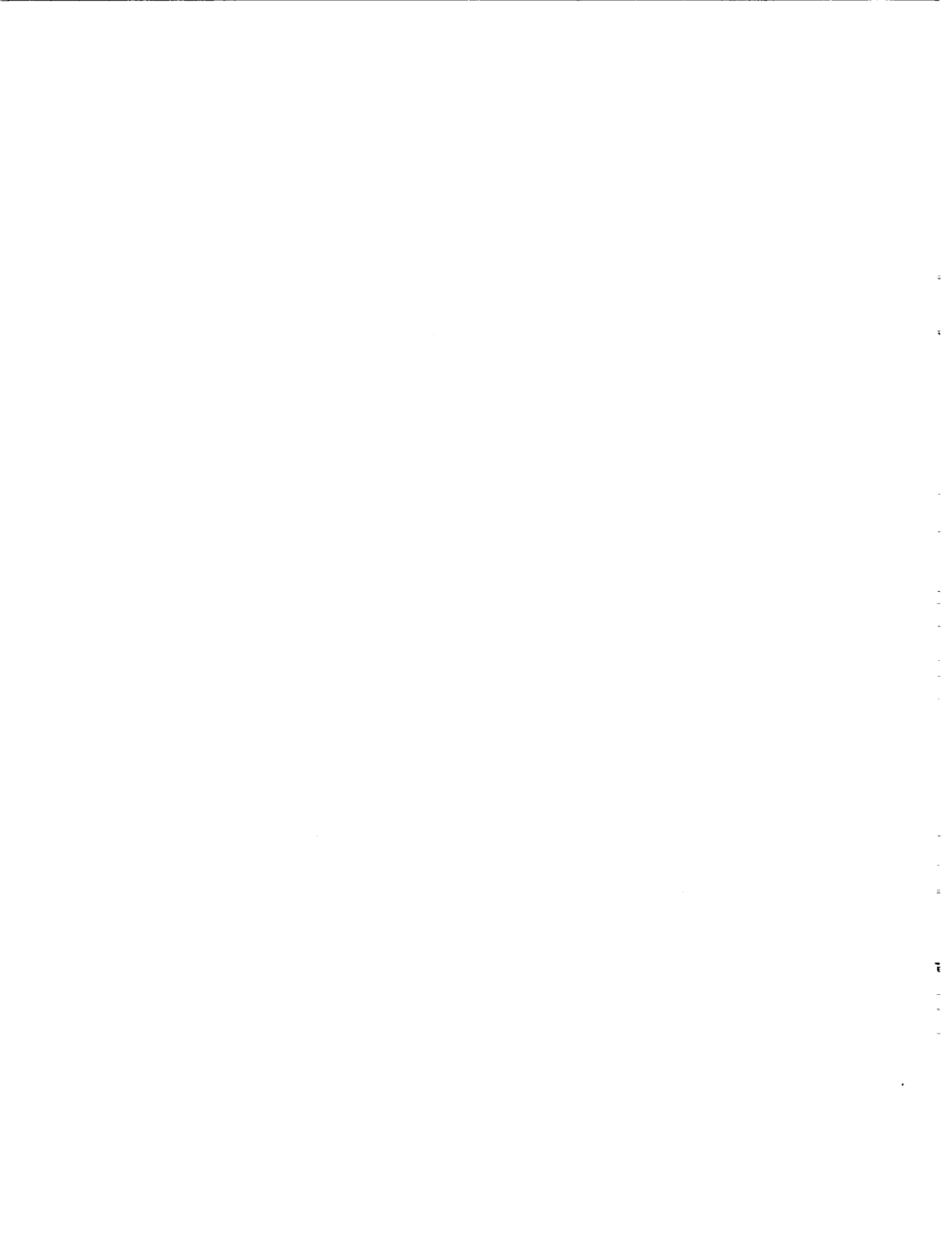


Figure 24. Effect of numerical grid refinement on predicted heating rates.  $Re_{2,D} = 13\,800$ ;  $\theta = 0^\circ$ ;  $\alpha = -5^\circ$ .





# Report Documentation Page

1. Report No. NASA TP-2954		2. Government Accession No.		3. Recipient's Catalog No.	
4. Title and Subtitle Surface Flow and Heating Distributions on a Cylinder in Near Wake of Aeroassist Flight Experiment (AFE) Configuration at Incidence in Mach 10 Air		5. Report Date January 1990		6. Performing Organization Code	
		8. Performing Organization Report No. L-16623		10. Work Unit No. 506-40-41-01	
7. Author(s) William L. Wells		11. Contract or Grant No.		13. Type of Report and Period Covered Technical Paper	
9. Performing Organization Name and Address NASA Langley Research Center Hampton, VA 23665-5225		12. Sponsoring Agency Name and Address National Aeronautics and Space Administration Washington, DC 20546-0001		14. Sponsoring Agency Code	
		15. Supplementary Notes			
16. Abstract Experimental heat-transfer distributions and surface streamline directions are presented for a cylinder in the near wake of the Aeroassist Flight Experiment forebody configuration. Tests were conducted in air at a nominal free-stream Mach number of 10, with postshock Reynolds numbers based on model base height of 6450 to 50 770, and angles of attack of 5°, 0°, -5°, and -10°. Heat-transfer data were obtained with thin-film resistance gage and surface streamline directions by the oil-flow technique. Comparisons between measured values and predicted values were made by using a Navier-Stokes computer code.					
17. Key Words (Suggested by Authors(s)) AFE Hypersonic Blunt body Wake heating			18. Distribution Statement Unclassified—Unlimited  Subject Category 34		
19. Security Classif. (of this report) Unclassified		20. Security Classif. (of this page) Unclassified		21. No. of Pages 56	22. Price A04

